Final Technical Report

Design and Implementation of Innovative Stimulation Treatments to Maximize Energy Recovery Efficiency at the Utah FORGE Site

Award Recipient Organization: University of Utah (DOE Project DE-EE0007080)

Subrecipient Organization:
The University of Texas at Austin
DUNS Identifier: 170230239
[Insert Address, City, State, ZIP Code]
Award Number: 4-2492

Project Period:
10/01/2021 – 12/31/2025

Principal Investigator:
Mukul M. Sharma
Professor, The University of Texas at Austin
msharma@mail.utexas.edu | 512-413-1803

Report Submitted By:
Mukul M. Sharma
Date of Report Submission: 12/31/2025
Reporting Period: 10/01/2021– 12/31/2025
Total Pages (excluding cover page): [Insert Total Pages]

Project Partners: Somnath Mondal, Shell Exploration and Production Company, Houston, TX.
Alan Reynolds, A. Reynolds LLC, Chesapeake, VA 23321

This material is based upon work supported by the U.S. Department of Energy under Award Number DE-EE0007080.

Abstract

Final Report for Design and Implementation of Innovative Stimulation Treatments to Maximize Energy Recovery Efficiency at the Utah FORGE Site

Proper design of Enhanced Geothermal Systems (EGS) must ideally meet the following performance criteria: (i) circulate the working fluid between wells at the desired flowrates at reasonable injection pressures; (ii) heat the circulating fluid to the desired temperature within a reasonable residence time; and (iii) minimize the rate of cooling of the surrounding reservoir rock to extend the economic project life. Such efficient extraction of thermal energy can be achieved if the created fracture network is uniformly distributed along the horizontal well and is well-connected to both wellbores so that the injected water can flow through the entire fracture network and not channel its way through thief zones or thief fractures. If such water channeling occurs, then most of the created fracture network will remain under-utilized and this dramatically reduces the thermal energy extraction rate.

Plug-and-perf (PnP) is the most cost-effective stimulation technique used to place fractures in horizontal wells. However, this method often leads to heel dominated fractures (as demonstrated in this project by fiber optic data). The primary objective of this project, therefore, was to achieve a more uniform stimulation and flow profile across the entire lateral and to ensure good inter-well connectivity. These key performance metrics were tested using different stimulation designs. Each design was evaluated and optimized by suitable instrumentation, diagnostics, and modelling.

Stimulation treatments were performed and successfully monitored with fiber in the 16A and 16B wells. Our installed fibers, interrogators and the PT gauge worked flawlessly and provided excellent data while the 16A well was being stimulated. The distributed temperature and the distributed strain data were recorded using both the Neubrex and the Optasense interrogators. This data was recorded over several days as fracture stages 4 through 10 were pumped. Results clearly showed that hydraulic fractures from the 16A well tilted away from prior fractures, either due to stress shadow effects or due to the presence of natural fractures.

The fiber optic data set collected when fracturing the 16A well was analyzed in near real time to determine suitable locations for perforating the 16B well. This ensured that the stimulation treatments in the 16B well had the best chances of intersecting the fractures created in the 16A well. This was accomplished by analyzing the distributed strain data obtained from the Rayleigh frequency shift data to identify the location of frac hits on the 16B well. The 16B well was successfully perforated with no damage to the fiber by mapping the fiber behind pipe. The fiber optic response of the stimulation treatments in the 16B well were next monitored and recorded over a period of 2 weeks. This is the most complete fracture diagnostic data set ever recorded for a geothermal well. The DAS data from the 16B well clearly shows that the fractures are heel dominated. This is consistent with the simulations conducted before the fracture treatment. Our simulations also show that using a tapered perforation design will improve the cluster efficiency and place the fluid and proppant more uniformly in all perforation clusters and improve injection conformance.

Finally, two fluid circulation tests were successfully monitored by the fiber. This data showed that the conductivity of the fractures connecting the two wells was low when the wells are shut-in but increases substantially with the fluid pressure in the injection well. Integrating the fiber data with the tracer data allowed us to map the conformance, connectivity and conductivity of fractures connecting the two wells. These three Cs control the performance of the EGS well pair.

The primary outcome of this project is a direct comparison of the effectiveness of different stimulation designs in Well 16A and Well 16B on the connectivity, conductance and conformance of fractures at the FORGE site. This comparison was made through the integration of fracture and flow diagnostic methods. The project developed new diagnostic and modelling workflows that provide a robust way to design completions and fracture treatments to achieve the technical objectives stated above for high-temperature geothermal EGS wells. This will lead to significant improvements in the design of future EGS well completions and stimulations and provide a much better understanding of the reasons for this improvement so that novel completion and stimulation procedures can be designed and implemented in the future.

DOE Award Number:

Award Recipient Organization: University of Utah (DOE Project DE-EE0007080)

Subrecipient Organization: The University of Texas at Austin (Award Number: 4-2492)

Principal Investigator: Mukul M. Sharma, Professor

Keywords: Geothermal Wells, Enhanced Geothermal Systems. EGS.

Table of Contents

ABSTRACT **2**

TABLE OF CONTENTS **4**

1. EXECUTIVE SUMMARY **6**

1.1 Background 6
1.2 Objectives 7
1.3 Key Findings 7

2. INTRODUCTION **8**

2.1 Purpose of the Report 8
2.2 Scope of Work 8
2.3 Organization of the Report 10

3. UTAH FORGE FIBER OPTIC MONITORING **12**

3.1 Monitoring Enhanced Geothermal Systems (EGS) 12
3.2 Fiber Optic Installation and Sensing at the FORGE Site 13
3.2.1 Circulation test 1 13
3.2.2 April 2024 well stimulation 14
3.2.3 Circulation test 2 14

4. NUMERICAL MODELING OF THE FORGE SITE **19**

4.1 Description of Fully Coupled Simulator – MF3D 19
4.1.1 Rock deformation 19
4.1.2 Flow in the reservoir and fracture 20
4.1.3 Flow in the wellbore 21
4.2 Hydraulic Fracturing with Fluid and Proppant Distribution 21
4.2.1 Fracture-Propagation Criterion 21
4.2.2 Wellbore distribution 22
4.2.3 Proppant distribution 23
4.3 Energy Balance 23

5. MONITORING FRACTURE GROWTH USING DISTRIBUTED STRAIN SENSING **26**

5.1 Monitoring EGS Fracture Propagation with Fiber Optics 26
5.2 Model Setup 27
5.3 Results and Discussion 27
5.3.1 Base case results 27
5.3.2 In-situ stress contrast 28
5.3.3 Completion design 29
5.3.4 Influence of frac fluid rheology 29

6. MONITORING FLUID CIRCULATION AT THE FORGE SITE (CIRCULATION TEST 1) USING THERMO-HYDRO-MECHANICAL MODELS AND FIBER-OPTIC DISTRIBUTED STRAIN DATA **36**

6.1 July 2023 Circulation Test 36
6.2 Model Setup 37
6.3 Results and Discussion 38
6.3.1 Base case results 38
6.3.2 Fracture stiffness 39
6.3.3 SRV formation compressibility 39
6.3.4 SRV deformability 40

6.3.5 SRV size 40
6.3.6 Multi-fracture simulation setup 40
6.3.7 Multi-fracture modeling results..40

7. MONITORING INFLOW DISTRIBUTION IN GEOTHERMAL WELLS DURING FLUID CIRCULATION (CIRCULATION TEST 2) USING DISTRIBUTED FIBER OPTIC MEASUREMENTS 49

7.1 Fiber Optic Inflow Profiling via Thermal Slugging...49
7.2 Monitoring Thermal Slugging During Fluid Circulation at FORGE...50
7.3 Model Setup 50
7.4 Results and Discussion 51
7.4.1 Base case results 52
7.4.2 Fluid velocity estimation...53
7.4.3 Multi-fracture simulation considering in-well circulation...54
7.4.4 Insights into Utah FORGE fiber optic monitoring data 55

8. INTEGRATION OF FIBER OPTIC DATA WITH FMI AND CHEMICAL TRACER DATA TO EVALUATE INTER-WELL FRACTURE CONNECTIVITY AND FLUID CIRCULATION IN GEOTHERMAL WELL PAIRS 67

8.1 Downhole Monitoring Data from the Utah FORGE EGS Test Site 67
8.2 Integration of Fiber Optic Data with FMI Log...68
8.2.1 Shifts in the injector perforation depths and production intersections.................................68
8.2.2 Fracture-fault interaction..69
8.2.3 Pre-existing faults from FMI log and frac-hits from fiber optic data.......................................69
8.3 Integration of Fiber Optic Data with Chemical Tracer Data 70
8.3.1 Stage connections detected in fiber optic data 70
8.3.2 Stage connections integrating the micro-seismicity data 71
8.3.3 Stage connections and fiber optic 16B production allocation...72
8.3.4 Flow contributions from chemical tracer data and fiber optic data during EGS circulation 72
8.4 Appendix A 72

9. STRATEGIES FOR IMPROVING INTER-WELL CONNECTIVITY AND PROPPANT PLACEMENT IN EGS WELL PAIRS .. 85

9.1 Inter-well Connectivity and Uniformity in Fluid and Proppant Distribution..........................85
9.2 Modeling Analysis of Fracturing Treatments in Injection Well 16A.......................................85
9.2.1 Model setup...85
9.2.2 Base case results 86
9.2.3 Effect of fluid viscosity...86
9.2.4 Effect of completion design 87
9.2.5 Effect of pumping schedule...87
9.3 Fiber Optic Monitoring Data and Modeling Interpretations of Treatment in Production Well 16B 88
9.3.1 HF-DAS data during the stimulation of well 16B...88
9.3.2 Modeling well 16B: base case results 88
9.3.3 Methods to optimize proppant and fluid distribution in clusters 88
9.3.4 Effect of fluid viscosity...89
9.3.5 Effect of lightweight proppant...89
9.3.6 Effect of tapered perforation design..90

LIST OF PAPERS 100

Final Report for
Design and Implementation of Innovative Stimulation Treatments to Maximize Energy Recovery Efficiency at the Utah FORGE Site

Principal Investigator: Professor Mukul M. Sharma
The University of Texas at Austin
Contact information: msharma@mail.utexas.edu

Subcontractors and/or Participating Organizations:
Somnath Mondal, Shell Exploration and Production Company, Houston, TX.
Alan Reynolds, A. Reynolds LLC, Chesapeake, VA 23321

Project Start and End Date: 10/2021 – 12/2025

1. Executive Summary

1.1 Background

A successful EGS must be able to (i) circulate desired fluid flowrates at reasonable injection pressures; (ii) heat the circulating fluid to the desired temperature within a reasonable residence time/well spacing; and (iii) minimize the rate of cooling of the surrounding reservoir rock to extend the economic project life. Such efficient extraction of thermal energy from fractured EGS requires a large contact area between the fracture system and the reservoir rock matrix. This can be achieved if the created fracture network is uniformly distributed along the horizontal well and is well-connected to both wellbores so that the injected water can flow through the entire fracture network and not channel its way through thief zones or thief fractures. If such water channeling occurs, then most of the created fracture network will remain under-utilized as no water flows through it and this dramatically reduces the thermal energy extraction rate.

Plug-and-perf (PnP) is the most common stimulation technique used to place fractures in horizontal wells. It is popular because it is low cost and it is possible to place 5 to 15 sets of fractures in a single pumping stage. However, this method often leads to heel dominated fractures (as shown by fiber optic data). The PI and Shell have recently demonstrated that this can lead to many of the perforation clusters not receiving much fluid or proppant.

This project, therefore, aims to achieve more uniform stimulation across the entire lateral to avoid short-circuiting between well pairs and to ensure good inter-well connectivity. This connectivity was tested for different stimulation designs. Each design was evaluated and optimized by suitable instrumentation, diagnostics, and modelling.

The expected outcome of this proposal was a direct comparison of the effectiveness of different stimulation methods in Well 16A and Well 16B at the FORGE site. This comparison is proposed to be made through the integration of fracture and flow diagnostic methods. This work will also lead to significant improvements in the design of future EGS well completions and stimulations and provide a much better understanding of the reasons for this improvement so that novel completion and stimulation procedures can be designed and implemented in the future.

1.2 Objectives

The project has the following overall technical objectives:

- Place fractures uniformly in a horizontal well (improve cluster efficiency) to ensure uniform distribution of flow into all hydraulic fractures;
- Maximize the area of the conductive and connected fracture network;
- Improve connectivity of the fracture network from the injector to the producer; and,
- Optimize fracture size.

Innovations in integrated fracture diagnostics enable model calibration and allow us to select the best stimulation method, diagnose stimulation uniformity, and optimize well spacing. A detailed assessment of the effectiveness of different stimulation methods was possible for the first time based on both results from numerical simulations and well diagnostic data.

The project developed diagnostic and modelling workflows that provide a robust way to design completions and fracture treatments to achieve the technical objectives stated above for high-temperature geothermal EGS wells. This design methodology is expected to increase the propped fracture area by over 50% and result in better connected and more uniform fractures. These improvements can have a transformational impact on geothermal energy extraction by increasing the rate of energy extraction by a factor of 2.

1.3 Key Findings

1. Stimulation treatments were performed and successfully monitored with fiber in the 16A and 16B wells.
2. The fibers we installed in the 16B well, interrogators and the PT gauge worked flawlessly and provided excellent data while both the 16A and 16B wells were being stimulated and during fluid circulation.
3. The distributed temperature and the distributed strain data were recorded using both the Neubrex and the Optasense interrogators.
4. The impact of different parameters such as fluid viscosity, proppant density and the number of clusters on the fracture performance were evaluated using simulations and changes to the fracture designs pumped in the different stages in the 16A and 16B wells.
5. This is the most complete fracture diagnostic data set ever recorded for a geothermal (EGS) well pair and will provide the basis for further analysis and interpretation in the coming months and years.
6. The fiber optic data set recorded in the 16B well while the 16A well was being fraced was analyzed in near real time to determine suitable locations for perforating the 16B well. The goal was to ensure that the stimulation treatments in the 16B well would have the best chances of intersecting the fractures created in the 16A well. This was accomplished by analyzing the distributed strain data obtained from the Neubrex interrogator (Rayleigh

frequency shift data) to identify the location of frac hits on the 16B well. Perforation depths and clusters were designed based on this analysis.

7. The 16B well was successfully perforated with no significant damage to the fiber. The fiber in the 16B well was successfully mapped by Schlumberger to ensure that the fiber would not be severed during perforating operations in the 16B well.
8. The fiber optic response of the stimulation treatments in the 16B well were next monitored and recorded over a period of 2 weeks.
9. Excellent DTS, DAS and distributed strain data as well as PT gauge data was collected using both the Neubrex and Optasense interrogators.
10. This data clearly showed a heel biased placement of proppant and fluid.
11. The pumping data collected in the frac van indicated that the fractures created in the 16B well were communicating with the 16A well fracs. This is excellent news as this would allow fluid to be circulated between this well pair.
12. Finally, two fluid circulation tests were successfully monitored by the fiber.
13. This data showed that the conductivity of the fractures connecting the two wells was low when the wells are shut-in but increased substantially when the fluid pressure in injection well (and the fractures). Fluid was successfully circulated between the two wells.
14. The fiber data was integrated with tracer data to map the conductivity and connectivity of fractures that connect the 16A and 16B wells.

2. Introduction

2.1 <u>Purpose of the Report</u>

This Final Report summarizes the work done over the course of the past 3 years in this project.

2.2 <u>Scope of Work</u>

The work was conducted in 7 primary tasks, Each task is summarized below.

Task 1: Build a subsurface model for the Utah FORGE site

A DFN model that is consistent with the core, log and other available data was completed and tested. Geological, geophysical microseismic and other data were studied to be able to build an accurate and representative geological and DFN model for area surrounding the 16A and 16B wells at the FORGE site.

Task 2: Optimize pumping & perforation scheme for different stimulation methods for Well 16A

The purpose of this task was to simulate the growth of hydraulic fractures in the presence of natural fractures. New equations were developed and a model was implemented that can model fracture propagation in a DFN model (including the interaction of natural and hydraulic fractures).

The hydraulic fracturing model was completed and integrated with the new FORGE DFN model. Several runs were made using the model to propagate hydraulic fractures in the new DFN model. The geometry of the fracture network created was shown to depend on many reservoir properties and on the pumping schedule. Simulations were run to better understand the role of the completion parameters and fracturing fluids on the geometry of the complex hydraulic fracture network. The net pressure and microseismic data recorded for 3 fracs conducted in Well 16A were simulated and history matched. With this calibration of the model, additional runs were made to design six hydraulic fracture treatments for the stimulation program in the 16A well. A final set of recommendations for the different treatments that should be pumped in the cased and cemented portion of the 16A well was presented to the FORGE team in July 2023. These fracture designs were modified based on comments received so that the fracturing program can be finalized well before the field deployment of the frac fleet. A presentation and publication was prepared recommending these stimulation treatments.

Task 3: Installation of fiber optic cables in Well 16B

Three sets of optical fibers were successfully installed in the 16B well in July and August, 2023. Centralizers and cable protectors were used to ensure that the cable was not damaged during installation. The cables were successfully tested by monitoring the cementing operation and gathering data for fluid migration.

The successful installation of the fibers required several meetings with the Utah FORGE team and the vendor teams to coordinate our efforts. The document that had details of the fiber installation procedure was followed to make the process more manageable. Because of the very long lead times (over 6 months) associated with manufacturing the special fiber optic cables and the other special items, we requested and obtained quotes for many specialized items. To ensure that all items are compatible and meet tight specifications and the timelines for installation, we submitted a request to sole-source some of the items (such as the high temperature fibers).

Task 4: Monitor / Analyze Stimulation Treatments in Well 16A

The purpose of this task was to monitor the stimulation treatments in Well 16A with a state-of-art FO high-temperature system, consisting of 2 permanent installed FO cables outside casing (a long cable to the toe, and a shorter cable to the heel of the well). This geometry enabled us to monitor DAS, DTS, and DSS over the entire wellbore, and obtain pressure at the heel and toe of Well 16B, during the well life cycle.

The fiber array (installed in the 16B well) was successfully used to monitor the fracture treatments in the 16A well. Our installed fibers, interrogators and the PT gauge worked flawlessly and provided excellent data while the 16A well was being stimulated. The distributed temperature and the distributed strain data were recorded using both the Neubrex and the Optasense interrogators. This data was recorded over several days as fracture stages 4 through 10 were pumped. The impact of different parameters such as fluid viscosity, proppant density and the number of clusters on the fracture performance was evaluated based on this data. This is the most complete fracture diagnostic data set ever recorded for a geothermal well and provides the basis for further analysis and interpretation in the coming months and years.

The fiber optic data set recorded in the 16B well while the 16A well was being fraced was analyzed in near real time to determine suitable locations for perforating the 16B well. The goal was to ensure that the stimulation treatments in the 16B well would have the best chances of intersecting the fractures created in the 16A well. This was accomplished by analyzing the distributed strain data obtained from the Neubrex interrogator (Rayleigh frequency shift data) to identify the location of frac hits on the 16B well. Perforation depths and clusters were designed based on this analysis.

Task 5: Compare field diagnostic data with simulations for fractures in well 16A

The purpose of comparing the model predictions with all available diagnostic measurements is that it allows us to interpret the data and make predictions about the behavior of the EGS system under different operating conditions. Many “what-if” scenarios were run to see if improvements to the energy recovery rate can be made.

The stimulation treatments in well 16A were modeled and compared with field data. The circulation tests were modeled and compared with fiber and tracer measurements.

Task 6: Monitor & analyze DTS/DAS/DSS data from stimulations in the 16B well

The purpose of this task was to monitor the fracturing treatments in the 16B well using different stimulation techniques and designs. The perforation locations were determined based on the Well 16A fracture locations identified from DSS. This optimization ensured a good connection between the well pairs.

The 16B well was successfully perforated with no significant damage to the fiber. The fiber in the 16B well was successfully mapped by Schlumberger to ensure that the fiber would not be severed during perforating operations in the 16B well.

The fiber optic response of the stimulation treatments in the 16B well were next monitored and recorded over a period of 2 weeks. Excellent DTS, DAS and distributed strain data as well as PT gauge data was collected using both the Neubrex and Optasense interrogators. The pumping data collected in the frac van indicated that the fractures created in the 16B well were communicating with the 16A well fracs.

The DAS data analysis was completed and the volumes of slurry and proppant entering each perforation cluster was estimated. The distribution of proppant was found to be heel biased for all the stages in the 16B well. This was completely consistent with the results of models for these stimulation treatments.

Task 7: Compare field diagnostic data with the simulation results for well 16B

The primary goal of this task was to test and recalibrate the hydraulic fracturing models used for designing the treatments in well 16B, using the treatment pressure, fiber optic data and other diagnostics. This comparison allowed us to interpret the fiber data and provide the most direct measure of the uniformity and connectivity of the fractures created in the PnP simulation stages.

We set up and ran models for the hydraulic fractures and the circulation tests that have been pumped to calibrate the models with data. What-if cases were run to improve the fracture designs. We modeled the fiber response of the two circulation tests that have been conducted. This provided us with much more insight into the connectivity between the 16A and 16B wells.

2.3 Organization of the Report

The work done and the primary accomplishments for each Task are presented in the Results and Discussion section of this report.

2.4 Publications and Presentations, Intellectual Property (IP), Licenses, etc.

1. “Integration of Fiber Optic Data with FMI And Chemical Tracer Data To Evaluate Inter-well Fracture Connectivity and Fluid Circulation In Geothermal Well Pairs”, Y. Ou, Chris Fredd and Mukul Sharma, SPE Hydraulic Fracturing Conference, Feb., 2026.
2. “Strategies for Improving Inter-well Connectivity and Proppant Placement In EGS Well Pairs: A Field Study Integrating Models And Well Fiber Optic Data”, Y. Li, Y. Ou, M. Mura, Mukul Sharma, SPE Hydraulic Fracturing Conference, Feb., 2026.

3. "Pressure Drawdown Testing in Fractured Production Wells: Impact of Geomechanics And Fracture Closure", Y. Li, Y. Ou, Mukul Sharma, SPE Hydraulic Fracturing Conference, Feb., 2026.
4. "Acoustic Emission Signatures During Frictional Sliding of Rocks: Insights Into Induced Seismicity Events", A. Sathyanath, Mukul Sharma, SPE Hydraulic Fracturing Conference, Feb., 2026.
5. "Inversion Of Natural Fracture Properties Using Microseismic Data and Hydraulic Fracture Simulation", Q. Liu and Mukul Sharma, SPE Hydraulic Fracturing Conference, Feb, 2026.
6. "Monitoring fluid circulation in an enhanced geothermal system with permanent fibers", ARMA Workshop on Distributed Fiber Optic Sensing for Geomechanical Applications, Paper presented at the 58th US Rock Mechanics/Geomechanics Symposium held in Golden, Colorado, USA, 23-26, June 2024, Yuhao Ou and Mukul M. Sharma.
7. "Factors Controlling the Flow and Connectivity in Fracture Networks in Naturally Fractured Geothermal Formations," SPE Drilling and Completions, Vol. 38, issue 01, pp 131-145, SPE-212292-PA, March 2023, M. Cao and M.M. Sharma. https://doi.org/10.2118/212292-PA.
8. "A computationally efficient model for fracture propagation and fluid flow in naturally fractured reservoirs," Journal of Petroleum Science and Engineering, Vol. 220, Part B, pp 111249, January 2023, M. Cao and M.M. Sharma. https://doi.org/10.1016/j.petrol.2022.111249
9. "The impact of changes in natural fracture fluid pressure on the creation of fracture networks," Journal of Petroleum Science and Engineering, Vol. 216, pp. 110783, September 2022, M. Cao and M.M. Sharma. https://doi.org/10.1016/j.petrol.2022.110783
10. "Creation of a Data-Calibrated Discrete Fracture Network of the Utah FORGE Site," ARMA 23–0822, Paper was presented at the 57th US Rock Mechanics/Geomechanics Symposium held in Atlanta, Georgia, USA, 25-28 June 2023, M. Cao and M.M. Sharma.
11. "Integrating a Boundary Element Method Based Hydraulic Fracturing Simulator with a Compositional Reservoir Simulator for Well Lifecycle Simulations," ARMA 23–0382, Paper was presented at the 57th US Rock Mechanics/Geomechanics Symposium held in Atlanta, Georgia, USA, 25-28 June 2023, M. Cao, S. Zheng, and M.M. Sharma.
12. "Geomechanical Modeling of Fracture Growth in Naturally Fractured Rocks: A Case Study of the Utah FORGE Geothermal Site," Paper presented at the Unconventional Resources Technology Conference held in Denver, Colorado, USA, 13-15 June 2023, M. Cao and M.M. Sharma.
13. "The Effect of Variations of Fluid Pressure in Natural Fractures on the Geometry of Fracture Networks and Well Productivity," Paper presented at the Unconventional Resources Technology Conference held in Denver, Colorado, USA, 13-15 June 2023, M. Cao and M.M. Sharma.
14. "Factors Controlling the Flow and Connectivity in Fracture Networks in Naturally Fractured Geothermal Formations," *SPE Drilling and Completions*, Vol. 38, issue 01, pp 131-145, SPE-212292-PA, March 2023, M. Cao and M.M. Sharma. https://doi.org/10.2118/212292-PA
15. "A computationally efficient model for fracture propagation and fluid flow in naturally fractured reservoirs," *Journal of Petroleum Science and Engineering*, Vol. 220, Part B, pp

111249, January 2023, M. Cao and M.M. Sharma. https://doi.org/10.1016/j.petrol.2022.111249
16. "An Efficient Model of Simulating Fracture Propagation and Energy Recovery from Naturally Fractured Reservoirs: Effect of Fracture Geometry, Topology and Connectivity," SPE-212315-MS, Paper presented at the SPE Hydraulic Fracturing Technology Conference and Exhibition, January 31–February 2, 2023, M. Cao and M.M. Sharma, doi: https://doi.org/10.2118/212315-MS
17. "The impact of changes in natural fracture fluid pressure on the creation of fracture networks," *Journal of Petroleum Science and Engineering*, Vol. 216, pp. 110783, September 2022, M. Cao and M.M. Sharma. https://doi.org/10.1016/j.petrol.2022.110783

3. Utah FORGE Fiber Optic Monitoring

3.1 Monitoring Enhanced Geothermal Systems (EGS)

Geothermal reservoirs composed of hot dry rock formations pose significant challenges for efficient heat extraction due to their inherently low permeability and porosity, despite the presence of abundant natural fractures. Enhanced Geothermal Systems (EGS) have emerged as a promising solution for overcoming these barriers and harnessing energy from such reservoirs by using hydraulic fracturing to generate high conductivity pathways for fluid circulation. EGS relies heavily on horizontal well drilling and multi-stage hydraulic fracturing to initiate a large number of interconnected fractures within the formation. This process dramatically increases the contact area between the injected fluid and the hot-dry-rock formation, thereby improving heat extraction efficiency. However, the success of EGS hinges on three critical factors: (1) hydraulic and thermal connectivity between the injection and production wells, (2) the conductivity and geometry of the induced fracture network, and (3) the uniformity of the injection and production profile in the injection and production wells. Despite the benefits of hydraulic fracturing in generating multiple flow pathways between injection and production wells, uncertainty in fracture propagation paths and flow routing, especially in heterogeneous or anisotropic formations, complicates efforts to predict and control long-term EGS performance.

The performance of interconnected wellbore systems primarily depends on two factors: (1) the geometry of the resulting fracture network, and (2) flow rates through the fracture system, which is generally inferred from the inflow rates from the various perforation clusters. Diagnostic tools such as microseismic and tiltmeters, have been used to assess the geometry of hydraulic fractures between injection and production wells. However, these methods generally lack the capacity to provide direct downhole measurements, and their spatial resolution limitations make it challenging to distinguish between individual producing clusters accurately. Additionally, fracture closure and uneven proppant distribution can result in discrepancies between the fracture geometry observed during hydraulic fracturing and the actual propped fracture geometry that is most relevant during fluid circulation. Moreover, obtaining reliable thermal and hydraulic data from downhole conditions in geothermal wells poses significant challenges. Traditional wellbore logging tools, including spinner logs and temperature surveys, are typically not designed to withstand the extreme temperatures often exceeding 200°C encountered in hot dry rock formations. These limitations underscore the need for robust and high-resolution sensing technologies capable of operating reliably in extreme geothermal environments.

Fiber optic distributed sensing, with superior integrity to survive under high-temperature and high-pressure conditions, has been used to monitor enhanced geothermal wells (Titov et al., 2023; Jurick, et. al. 2025 and Ou et. al. 2024). As a part of this project, at the Utah FORGE enhanced geothermal test site, we have installed fiber, gathered fiber optic data and leveraged it to generate a comprehensive dataset covering the entire process of EGS operations from multi-stage fracturing treatments to inter-well fluid circulation.

3.2 Fiber Optic Installation and Sensing at the FORGE Site

Located near Milford, Utah, the FORGE site targets a hot dry rock granite formation at depths exceeding 3,000 meters and temperatures over 220°C, representing a milestone in the demonstration of full-scale EGS development (Figure 3.1a). It combines state-of-the-art horizontal drilling, multi-stage hydraulic stimulation, and fiber-optic distributed sensing to investigate fracture geometry, inter-well connectivity, and heat extraction efficiency in hot dry rock. As one of the first geothermal projects to apply distributed fiber sensing during both stimulation and circulation, FORGE has generated invaluable datasets that improve the understanding of subsurface heat and mass transfer in EGS.

The Utah FORGE test site features a geothermal circulation system consisting of a deviated injector well (16A) and a corresponding deviated producer well (16B) (Figure 3.1b). Both wells, 16A and 16B, are long slanted wells with the producer 16B drilled above the injector, 16A. Aiming to establish connectivity with the production well 16B and increase the permeability of the geothermal reservoir between the wells, multi-stage hydraulic fracturing was applied to stimulate the injector 16A and increase the connectivity between injector and producer. Three stages of hydraulic fracturing stimulation were completed in April 2022 without proppant injection. Stages 3R to stage 10 in 16A were completed later in April 2024 with additional fracturing stages still to be planned. During most of these stages, proppant was used. Fracture diagnostic tools were employed to monitor the fracture intersections along the production well 16B during the stimulation of 16A. 4 stages in 16B were then stimulated at detected intersections to establish good hydraulic connectivity between the two sets of fractures created in the injector and producer. Two major inter-well circulation tests were conducted: the first in July 2023 and the second in April 2024, conducted immediately after the April 2024 hydraulic fracturing campaign. During these tests, fluid was injected at fixed rates into well 16A and extracted from well 16B to test the connectivity of the created multi-fracture system.

To monitor the hydraulic stimulation and fluid circulation, a multi-mode fiber-optic cable was permanently cemented behind the casing of well 16B (Figure 3.2). This allowed for the deployment of distributed acoustic, temperature and strain sensing technologies (DAS, DTS and DSS data were all collected at the FORGE site) under extreme subsurface conditions. Notably, this system withstood prolonged exposure to high temperatures (> 220°C) and enabled distributed, real-time monitoring during both stimulation and EGS fluid circulation tests.

3.2.1 Circulation test 1

In the July 2023 fluid circulation test, fiber optic distributed strain sensing was used to monitor the possible fracture intersections along the production/monitoring well 16B and their responses during the EGS circulation. In the fiber optic strain rate waterfall that plots the strain rate with respect to measured depth along the producer and circulation time, tensional strain rate signals are seen in the zone of interest suggesting possible intersecting fractures and an overall expansion of the formation due to injection (Figure 3.3). Geometry characteristics of these observed tensional strain rate signals are expected to correlate with fracture conductivity and property changes in the stimulated reservoir volume (SRV).

3.2.2 April 2024 well stimulation

Hydraulic fractures in geothermal injection wells must intersect production wells so that good fluid communication can be maintained between the wells ensuring overall success in geothermal energy extraction (Jurick et al., 2025). In the FORGE April 2024 well stimulation of 16A and 16B, the deployed multi-mode fiber cable was employed to monitor fracture propagation with the aim of assessing the geometry and connectivity of the stimulated fracture network. Using the Rayleigh frequency shift based distributed strain sensing (DSS-RFS), the team continuously monitored fracture stimulation events originating from the adjacent injection well (stage 3R to stage 10 in 16A). These measurements enabled the detection of fracture-driven interactions, commonly referred to as “frac hits”, along the production well (Figure 3.4). The insights from the fiber optic data, interpreted as fracture intersections from the distributed strain data, were then used to guide the design and placement of perforation clusters in the production well (Figure 3.5). In the following production well stimulation (stage 1 to 4 in 16B), HF-DAS provided additional information regarding the fluid and proppant distribution during the fracturing injection (Figure 3.6). This data-informed strategy resulted in successful hydraulic fractures that effectively linked the injection and production wells, as later confirmed by cross-well circulation tests conducted after well stimulation (Ou et al., 2025).

3.2.3 Circulation test 2

Following the stimulation of production well 16B, fiber optic monitoring remained active throughout the April 2024 fluid circulation test. During the early stages of circulation, thermal slugging behavior, characterized by abrupt temperature changes along the wellbore, were observed in the fiber optic waterfall plot originating from the four perforated stages completed along well 16B (Figure 3.7). This phenomenon was attributed to heterogeneous thermal conditions within the wellbore, a residual effect of prior hydraulic stimulation. The gradient of these thermal slugs provided insight into fluid velocity variations along the producer 16B, illustrating the value of distributed fiber-optic sensing to resolve real-time subsurface flow dynamics with high sensitivity to localized thermal and hydraulic perturbations.

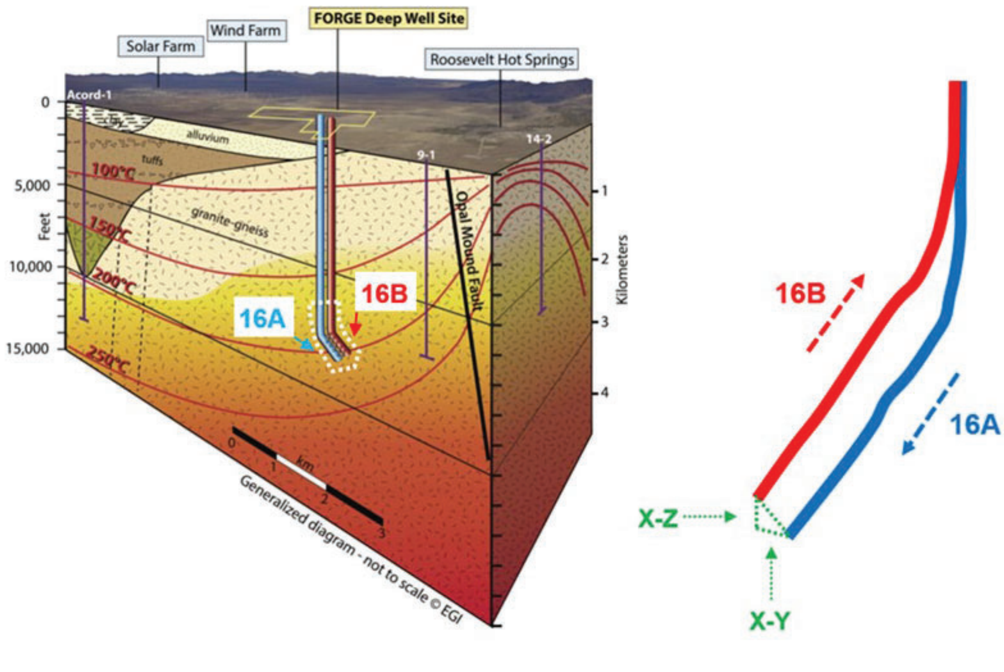

(a) (b)

Figure 3.1: (a) General well placement of the Utah FORGE EGS test site. The EGS consists of one long deviated injector 16A (shown in blue color) and one deviated producer 16B placed above it (depicted in red color); (b) Well placement of the injection well 16A and production well 16B in the FORGE geothermal formation. The EGS well pair is 110 meters apart in the X-Z plane and a distance of 60 meters in the X-Y plane (Ou et al., 2025c).

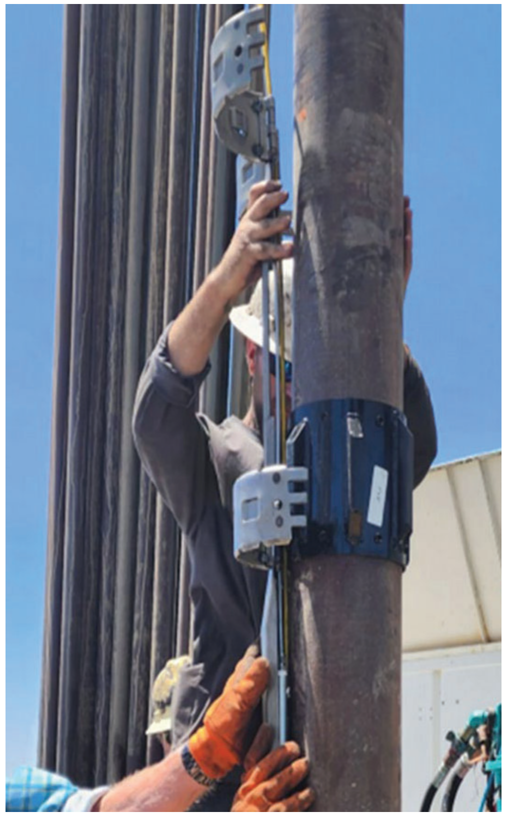

Figure 3.2: Installation of the multi-mode University of Texas - Shell fiber optic cable in the 16B well.

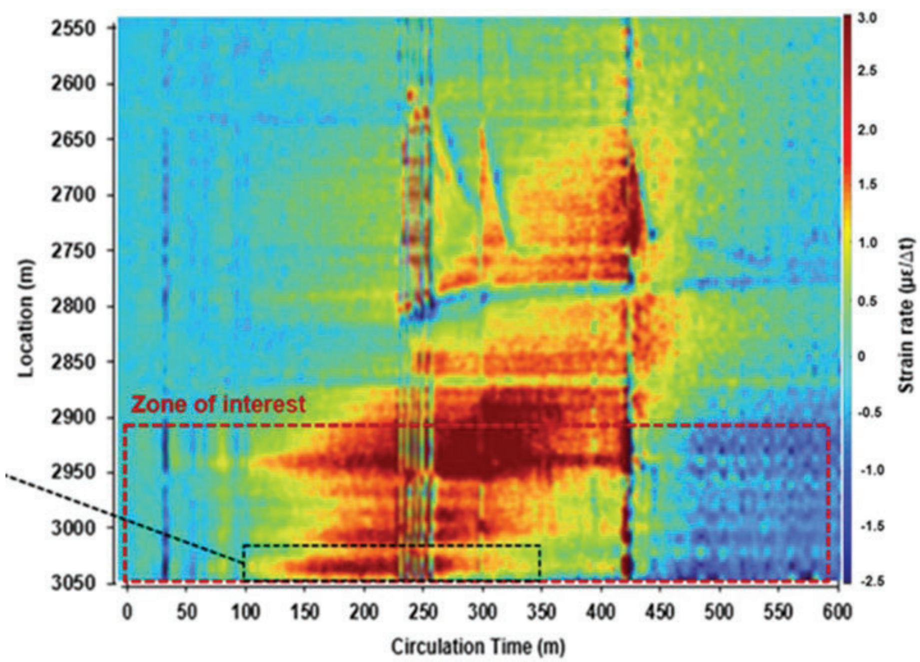

Figure 3.3: Fiber optic strain rate waterfall plot obtained during the FORGE July 2023 circulation test. Clear red tensional strain rate signals indicate intersecting hydraulic fractures within the zone of interest (Ou et al., 2024).

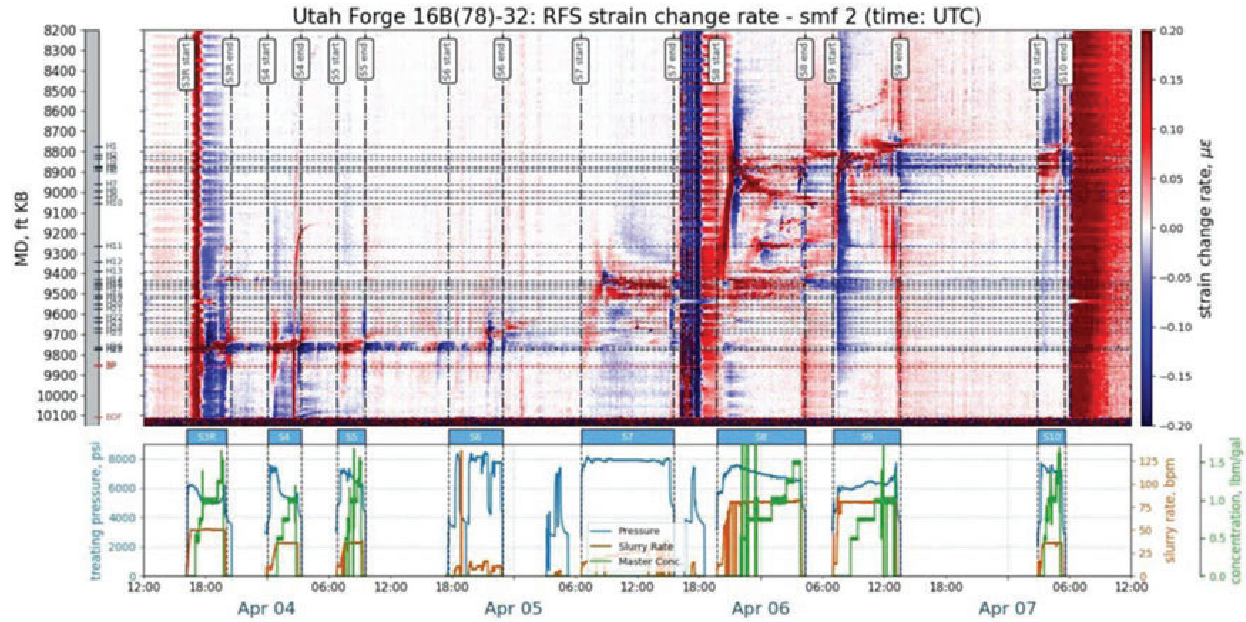

Figure 3.4: DSS-RFS strain change rate fiber optic monitoring along well 16B during the April 2024 stimulation of well 16A at the Utah FORGE site. (Jurick et al., 2025).

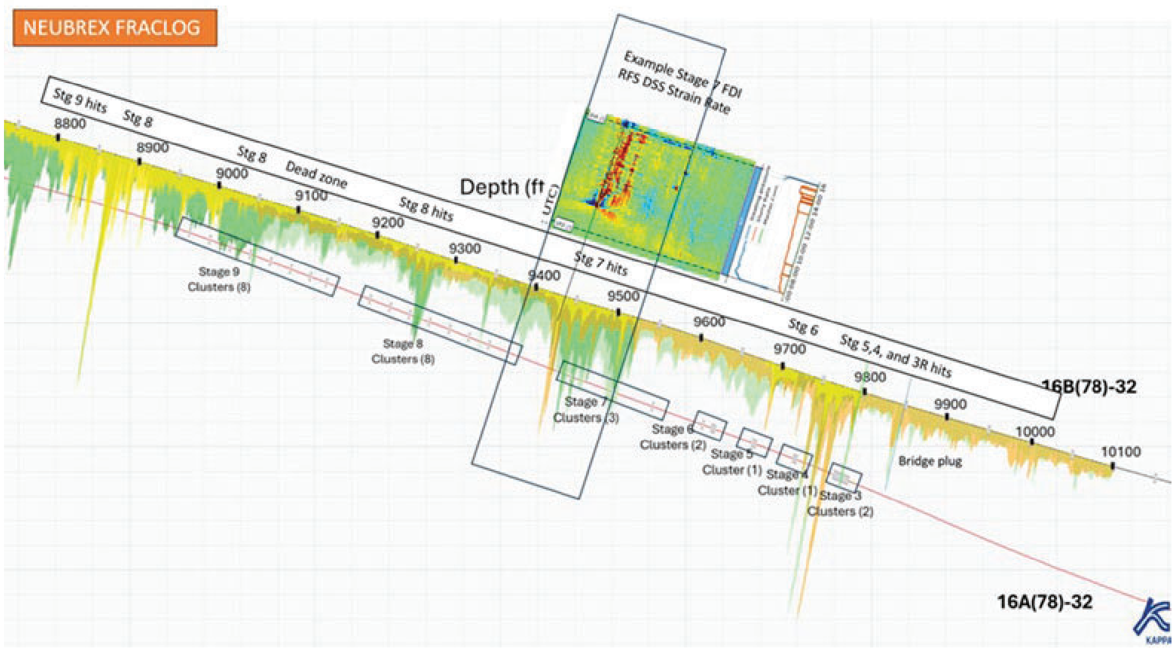

Figure 3.5: Rayleigh Frequency Shift (DSS-RFS) Strain Change, projected onto the 16B monitor well, with 16A hydraulic fracturing stage positions indicated on the 16A wellbore trajectory. (Jurick et al., 2025).

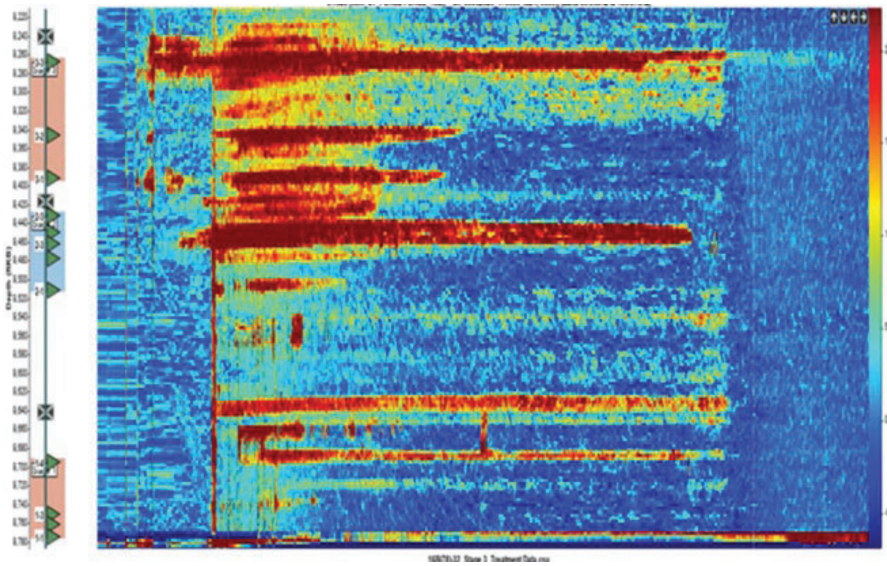

Figure 3.6: Example of HF-DAS monitoring data during the stimulation of stage 3 in the production well 16B.

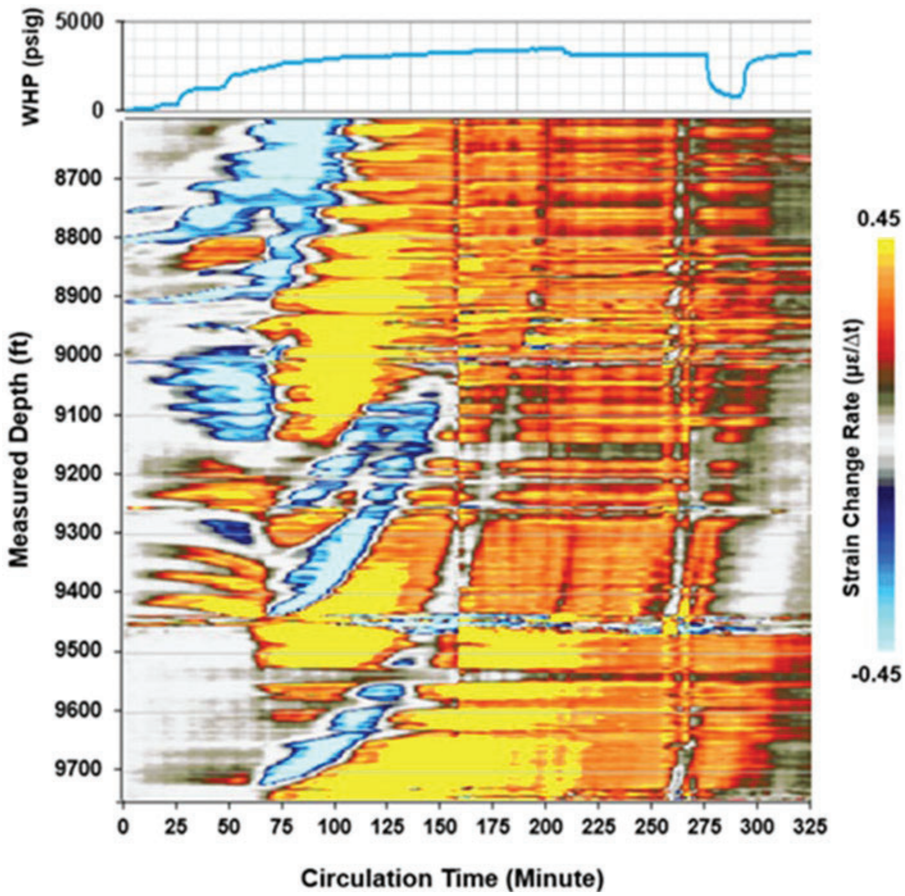

Figure 3.7: Fiber optic waterfall plot obtained from the April 2024 water circulation test with clear thermal slugging behavior during early fluid circulation (Ou et al., 2025b).

4. Numerical Modeling of the Forge Site

4.1 Description of Fully Coupled Simulator – MF3D

To understand and interpret the acquired fiber optic data, a fully coupled geomechanical simulator, Multifrac-3D, was employed for modeling the hydraulic fracturing treatments and EGS fluid circulation at the Utah FORGE site. The simulator incorporates a comprehensive coupling of rock deformation within the reservoir, flow within the reservoir, flow within the fracture and flow within the wellbore. Wellbore flow rate and pressure are implicitly solved and coupled with the corresponding solution of fracture domain and reservoir domain (Figure 4.1). This is essential for handling complex cross flow among fractures during production shut in. The governing equations for the reservoir and fracture domains are formulated independently and are coupled through interface conditions at the fracture–reservoir boundary. An implicit fracture surface contact model is implemented to account for the dynamic width change of propped fractures (with different proppant amount and stiffness) during fracture closure and production.

Rock deformation in the reservoir is discretized using an extended finite volume (FV) approach (Cardiff et al., 2016). Fluid flow in the reservoir and wellbore is discretized using a cell-centered FV method (Manchanda et al., 2020). The hydraulic fracture is represented as two collocated planes of discontinuity in the reservoir and is discretized using a novel finite area (FA) method (Bryant 2015). The multi-physics embedded in the fully coupled numerical system results in a set of highly non-linear algebraic equations. The Newton-Raphson method is utilized to linearize the non-linear equations and solve the resulting linear algebraic system (Figure 4.2) iteratively upon convergence.

4.1.1 Rock deformation

The reservoir domain is discretized into several non-overlapping control volumes, which are referred to as "cells" in the finite volume method. All the boundaries, including the fractures, are divided into "faces". The reservoir displacement equation describes the solid deformation in the reservoir domain, which is derived from the conservation of linear momentum and substitution of Cauchy stress tensor. The resulting governing equation (Eq. 4.1) is a surface integral of flux consists of displacement and pressure inside the grid cell (Cardiff et al., 2016). considering the effect of poro-elasticity.

$$\oint_{\Gamma}[(2\mu + \lambda)n \cdot \nabla u_n + \lambda n tr(\nabla_t u_t) + \mu n \cdot \nabla u_t + \mu \nabla_t u_n + \sigma_0 + \alpha p I] d\Gamma = 0 \quad (4.1)$$

where n is the face normal vector, Γ is the face area of the control volume, and u_n and u_t are the normal and tangential displacement respectively. μ and λ are the Lame constant, σ_0 is the in-situ stress, and α is the Biot's coefficient accounting the effect of poro-elasticity.

On the reservoir fracture interfaces Γ_b, closure and dilation of the fracture at the boundary (Eq. 4.2) are influenced by various factors, including the pressure of the fracture fluid p_f, and the contact force σ_n, between two adjacent fracture faces. Fracture closure and contact force are determined by fracture stiffness and proppant concentration (when proppant transport is considered).

$$\int_{\Gamma_b}[(2\mu + \lambda)n \cdot \nabla u_n + \lambda n tr(\nabla_t u_t) + \mu n \cdot \nabla u_t + \mu \nabla_t u_n + \sigma_0 + \alpha p I] d\Gamma + \mathrm{n} p_f |\Gamma_b| + \sigma_n = 0 \quad (4.2)$$

The fracture contact force, σ_n is calculated according to the Barton-Bandis rock joint correlation (Eq. 4.3) as a function of fracture width and fracture stiffness (Bandis et al., 1983). Fracture width is directly related to fracture conductivity that dominates fluid flow within the fracture. The computation of fracture width is based on the reservoir displacement boundary field (Manchanda et al., 2020) and is implicitly coupled with the solution of fracture pressure. This dynamic fracture width calculation is the fundamental coupling physics enabling the accurate simulation of hydraulic fracturing, fracture closure and production with varying fracture conductivity.

$$\sigma_n = \frac{w_{offset} - w}{a - b\left(w_{offset} - w\right)}, \quad a = \frac{1}{K_{ni}}; \quad b = \frac{1}{K_{ni} w_{offset}} \tag{4.3}$$

The parameter, w_{offset} is the critical width below which a fracture face is considered propped (it depends on the proppant concentration at any point inside the fracture). A corresponding fracture surface contact force is incorporated into the rock deformation equation on the closed fracture element. The initial normal stiffness of the fracture face, K_{ni} is determined by either the stiffness of the proppant pack or the fracture surface asperity.

4.1.2 Flow in the reservoir and fracture

Flow within the reservoir is governed by mass conservation driven by Darcy's flow in porous media (Eq. 4.4). This equation is spatially discretized using the finite volume method in terms of fluid pressure, incorporating the effects of poro-elasticity.

$$\int_{\Omega} \frac{1}{M} \frac{dp}{dt} d\Omega - \int_{\Omega} \nabla \cdot \left(\frac{k_m}{\mu_f} \nabla p \right) d\Omega + \int_{\Omega} \alpha \frac{\partial}{\partial t} (\nabla \cdot u) d\Omega = 0 \tag{4.4}$$

where k_m is the rock permeability, μ_f is the fluid viscosity, M and α is the Biot modulus for poro-elastic coupling with displacement field u.

Similarly, fluid flow within the hydraulic fracture is described by a mass conservation equation that accounts for fracture fluid leak-off, with spatially varying conductivity resulting from the non-uniform fracture width distribution. The corresponding governing equation is discretized using the finite area method (Eq. 4.5). The modified equivalent fracture permeability derived from the Tallmadge equation (Eq. 4.6) is used for modeling fluid flow through the proppant pack inside the fracture (Tallmadge et al., 1970).

$$\int_S \frac{w}{K_f} \frac{\partial p_f}{\partial t} dS + \int_S \frac{\partial w}{\partial t} dS - \oint_{\partial S} n \cdot \frac{k_f w}{\mu_f} \nabla p_f dL + \int_S \frac{k_m}{\mu_f} \frac{(p_f - p_{in})}{\delta_n} dS - q_i = 0 \tag{4.5}$$

$$k_f = \frac{d_p^2 (1 - c)^3}{\frac{c^2}{w^{1.5}} (0.150 + 0.0042 (\frac{d_p \rho_f u_f}{\mu_f c})^{5/6})} \tag{4.6}$$

where p_f is the fracturing fluid pressure, w is the fracture width, S is the surface area of the fracture face, μ_f is the fracturing fluid viscosity, k_f is the fracture permeability, k_m is the reservoir permeability adjacent to the fracture surface, w is the width of the fracture, K_f is fluid bulk modulus, q_i is the cluster volume slurry rate, and δ_n is the distance between the center of one fracture face (with fracturing fluid pressure p_f) and the center of its adjacent reservoir cell (with pore pressure p_{in}) for calculating fluid leak-off rate based on Darcy's law. ρ_f is the fracture fluid density, u_f is the Darcy flow velocity in fracture, d_p is proppant diameter and c is the proppant concentration.

4.1.3 Flow in the wellbore

Flow within the wellbore is treated as one-dimensional fluid flow through a pipe and is numerically discretized along the wellbore trajectory using a finite volume method (Figure 4.3). Mass transfer at wellbore connections, including open-hole leak-off and injection/production from connected hydraulic fractures, are incorporated as point rate sources calculated based on pressure drop and a modified production index. The first wellhead grid cell controls the production/injection schedule of the entire system by constraining either the wellhead pressure or rate.

The governing equations of wellbore flow rate are derived from mass conservation of wellbore fluid (Eq. 4.7). Fluid pressure is computed with respect to the momentum conservation of wellbore flow (Eq. 4.8).

$$\frac{\partial(\rho_j S_j)}{\partial t} + \frac{1}{A}\frac{\partial(A\rho_j S_j u_j)}{\partial x} = \rho_j q_j \tag{4.7}$$

$$\frac{\partial(\rho_B u_B)}{\partial t} + \frac{\partial(\rho_B u_B^2)}{\partial x} + \frac{\partial p}{\partial x} + \rho_B g sin\theta + \frac{f\rho_B u_B^2}{2D} = 0 \tag{4.8}$$

where ρ_j is the density of the fluid phase j, S_j is the saturation of phase j, A is the cross-section area of the wellbore, u_j is the velocity of the fluid phase j, q_j is the volumetric source/sink term of phase j, which includes the mass transfer between the coupled wellbore and the reservoir volumes and the mass transfer between the coupled wellbore and the fracture volumes. p is the fluid pressure, θ is the incline angle of the well section, D is the wellbore diameter, and f is the friction factor. ρ_B is the bulk fluid density and can be calculated as $\rho_B = \sum_{j=1}^{n_p} \rho_j S_j$, where n_p is the number of phases. u_B is the total velocity of the fluid mixture assuming all phases have the same velocity.

Mass transfer between wellbore and fracture is calculated by the modified Peaceman well model (Eq. 4.9), which employs the production index (*PI*) based on near wellbore fracture permeability, wellbore diameter and the wellbore skin factor (Eq. 4.10). Wellbore pressure and flow rate are implicitly coupled to correctly handle the complex fluid partition during injection and cluster crossflow during production shut in.

$$q_j = PI\frac{kk_{rj}}{\mu_j}(p_{fj} - p_w) \tag{4.9}$$

$$PI = \frac{k_f w}{0.5\ln\left({L_f}^2 + {h_f}^2\right) - \ln(r_w) + \ln(S) - 1.966} \tag{4.10}$$

where q_j is the flow source or sink, μ_j is the fluid viscosity of phase j, L_f is the fracture length in the well block, h_f is the fracture height in the well block, k_f is the fracture permeability at the fracture-wellbore intersection, r_w is the wellbore radius, S is the skin factor of the well.

4.2 Hydraulic Fracturing with Fluid and Proppant Distribution

4.2.1 Fracture-Propagation Criterion

The Mode I fracture-propagation criterion using stress-intensity factors (SIFs) is used to evaluate the "face breaking" and SIFs are calculated using the semi-analytical solutions shown in Eq. 4.1 (Olson 1991). The fracture propagation criterion (for crack dilation) is based on checking if $K_I > K_{Ic}$. K_{Ic} is the user specified tensional strength of the reservoir rock. The crack propagation direction is calculated based on the maximum tangential stress at the fracture tip. The propagation direction θ, which is the angle away from the crack tip direction, is calculated by Eq. 4.12.

$$K_I = \frac{0.806\sqrt{\pi} d_n E}{4\sqrt{2a}(1-v^2)}, \qquad K_{II} = \frac{0.806\sqrt{\pi} d_s E}{4\sqrt{2a}(1-v^2)} \tag{4.11}$$

$$\theta = 2\tan^{-1}\frac{-2K_{II}}{K_I + \sqrt{K_I^2 + 8K_{II}^2}} \tag{4.12}$$

where K_I and K_{II} denote the normal and shear stress intensity factors, a is the element half length, d_n and d_s are the normal and shear displacement discontinuity, E is the Young's modulus, and v is the Poisson's ratio.

In the simulation of fracture propagation, the fracture must propagate along the internal faces of the reservoir mesh. A dynamic mesh-modification algorithm is implemented to enable the cutting of mesh cells diagonally to enable fracture turning. A cell in the fracture propagation direction is split into two triangular prism cells when the propagation angle is within a certain range, and the newly created internal face is converted into boundary faces and becomes a part of the fracture (Figure 4.4). In addition, validation of this fracture propagation simulation against the analytical solutions of classical PKN and KGD models can be found in Manchanda et al. (2020).

4.2.2 Wellbore distribution

The flow of slurry and proppant in the wellbore and the distribution of slurry and proppant into the fractures is treated as a set of point sources (fracture cluster with perforations) flow into and out of a pre-determined finite volume ensuring mass conservation with wellbore storage (Eq. 4.13). Fluid injected into a multi-cluster fracture treatment is distributed between the clusters and corresponding fractures. q_i in Eq. 4.5 is this distributed flow rate for each fracture in the system and is calculated using a resistance model developed by Yi and Sharma (2018). In the integrated fracturing simulation model, wellbore distribution is implicitly coupled into the solution of fracture and reservoir (Zheng et al., 2019). We calculate the slurry distribution using the resistance calculation that includes the pressure drop in the wellbore sections, the pressure drop in the perforations, and the pressure in the fracture at the injection location (Figure 4.5).

$$P_{BHP} - P_{BHP}^{old} - \frac{K_f}{V_{well}}\left(q_{in} - \sum_{i=1}^{n} q_i\right)\Delta t = 0 \tag{4.13}$$

where P_{BHP} is the bottom hole pressure at the current time step, P_{BHP}^{old} is the bottom hole pressure in the previous time step, K_f is the wellbore fluid bulk modulus, V_{well} is the wellbore volume, q_i is the injection rate into each cluster and q_{in} is the total injection rate into this treatment stage. If there are n clusters being considered, then one will have n + 1 more governing equations and n + 1 more unknowns: n equations for fluid distribution and 1 equation for the wellbore storage effect, and n unknowns for cluster flow rates (q_i) and 1 unknown for bottom hole pressure (P_{BHP}). The fracture fluid pressure near the injection point (perforations) is calculated according to Eq. 4.14. The friction pressure drop within each wellbore segment is calculated according to the friction factor method (Bird et al., 2007), and the pressure drop across perforations is calculated based on Romero's correlation (Romero et al., 1995) in which the pressure drop scale quadratically with the cluster flow rate (Eq. 4.15).

$$p_f = p_{BHP} - \Delta p_{section} - \Delta p_{perf} \tag{4.14}$$

$$\Delta p_{perfi} = \frac{0.2369\rho q_i^2}{n_{perf}^2 d_{perf}^4 K_d^2} \tag{4.15}$$

where ρ is the fluid density, n_{perf} is the number of active perforations, d_{perf} is the perforation diameter, and K_d is the discharge coefficient in which the effect of perforation erosion can be considered through dynamic change of the discharge coefficient.

4.2.3 Proppant distribution

An empirically derived Particle Transport Efficiency (PTE) correlation based on high-fidelity CFD–DEM simulations is used, enabling accurate prediction of fluid and proppant partitioning among perforation clusters. The approach follows the framework established by Wu and Sharma (2016, 2019) and Zhang et al. (2019), preserving the essential physics of near-wellbore particle entry while allowing computationally efficient multi-cluster simulations.

The simulator represents the near-wellbore region of a horizontal stage with multiple perforation clusters connected to planar fractures. The slurry flow in the wellbore is modeled as a single-phase continuum carrying a dispersed solid phase, and the fluid– particle interactions are incorporated through the PTE-based closure. The PTE is defined as the ratio of the proppant mass rate entering a perforation to the total upstream proppant mass rate. It serves as the principal coupling term linking local hydraulics, slurry rheology, and particle transport (Eq. 4.16).

$$PTE = f(D_{well}, D_{perf}, D_p, \rho_p, \mu, q_{slurry}, C_{ppg}, r) \tag{4.16}$$

The coefficient embedded in the simulator implementation are directly taken from regression fits to the CFD–DEM dataset of Zhang et al. (2019), which quantify how particle transport efficiency varies with Reynolds number, perforation geometry, and slurry viscosity.

Perforation plugging is modeled through a local concentration-based criterion that captures the onset of particle bridging within the perforation tunnel. The instantaneous proppant concentration inside a perforation, C_p, is calculated as the ratio of the proppant volumetric flux to the total slurry flux (Eq. 4.17).

$$C_p = \frac{Q_{p,perf}}{Q_{slurry,perf}} \tag{4.17}$$

where, $Q_{p,perf}$ and $Q_{slurry,perf}$ denote the proppant and total slurry volumetric rates through the perforation, respectively. When the local concentration C_p exceeds the critical proppant concentration C_{crit}, the perforation is considered hydraulically plugged.

4.3 Energy Balance

The governing equation of energy conservation for porous media and wellbore full of n_p fluid phases (Eq. 4.18) is derived from the first law of thermodynamics.

$$\rho_B C_{pB} \frac{\partial T}{\partial t} - \nabla \cdot (k_B \nabla T) + \sum_{j=1}^{n_p} \rho_j C_{pj} u_j \nabla T = \sum_{j=1}^{n_p} \rho_j q_j C_{pj} (T - T_0) \tag{4.18}$$

where the bulk heat capacity $\rho_B C_{pB} = (1-\phi)\rho_s C_{ps} + \phi \rho_f C_{pf}$, C_{pj}, C_{ps} and C_{pf} are the specific heat capacity of phase j, the rock and the fluid, and ρ_j, ρ_s and ρ_f are the density of phase j, the rock and the fluid. The bulk thermal conductivity $k_B = \phi \sum_{j=1}^{n_p} k_j S_j + (1-\phi) k_s$, where k_j

and k_s are the thermal conductivity for phase j and rock. And u_j is the phase j velocity, T is the recent temperature, while T_0 is the reference temperature.

The coupling is added to conservation equations and pressure equations of both wellbore and reservoir. If non-isothermal condition is used, the wellbore volumes will act as a heat source q_T to the coupled reservoir cells (Eq. 4.19) via conduction and convection (if it is an open-hole completion).

$$q_T = \pi D k_w (T_r - T_w) + \sum_{j=1}^{n_p} \rho_j q_j C_{pj} (T_r - T_w) \tag{4.19}$$

where q_T is the heat flux from the wellbore to the reservoir, k_w is the conductive heat transfer coefficient, C_{pj} is the heat capacity of phase j, T_r and T_w are the temperature in the coupled reservoir and wellbore control volume pairs.

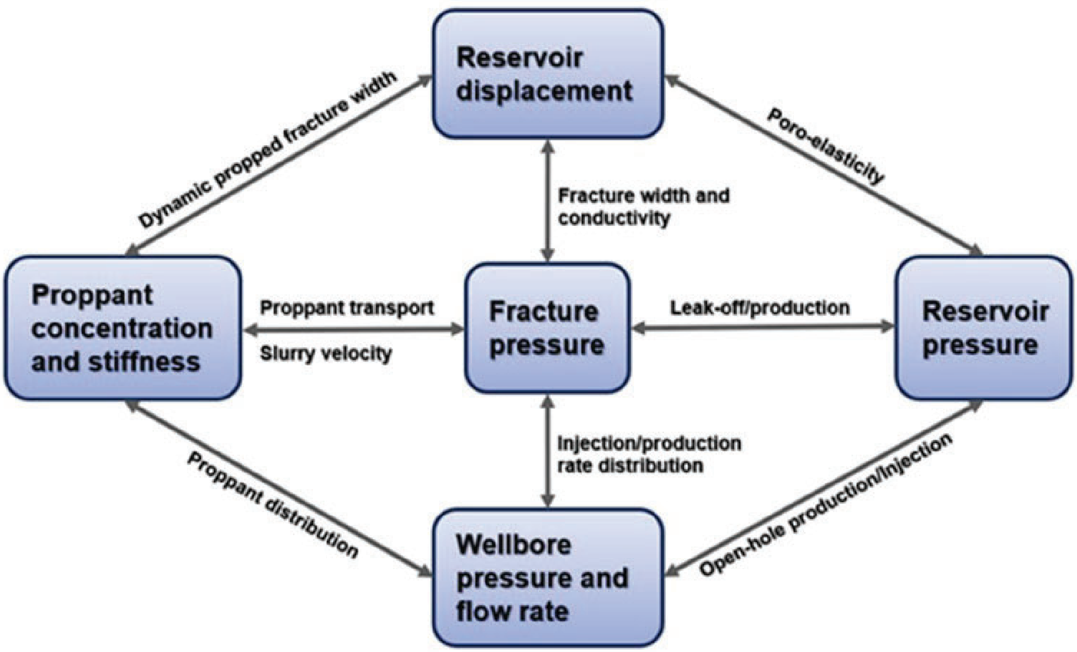

Figure 4.1: Primary governing equations in the reservoir-fracture-wellbore system.

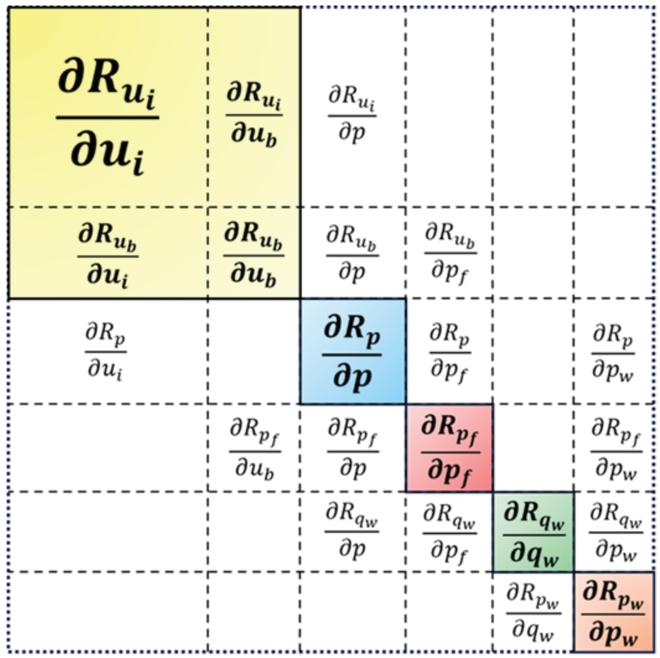

Figure 4.2: Jacobian matrix of the fully coupled non-linear system. Non-diagonal parts are the coupling terms linking the numerical domains with each other.

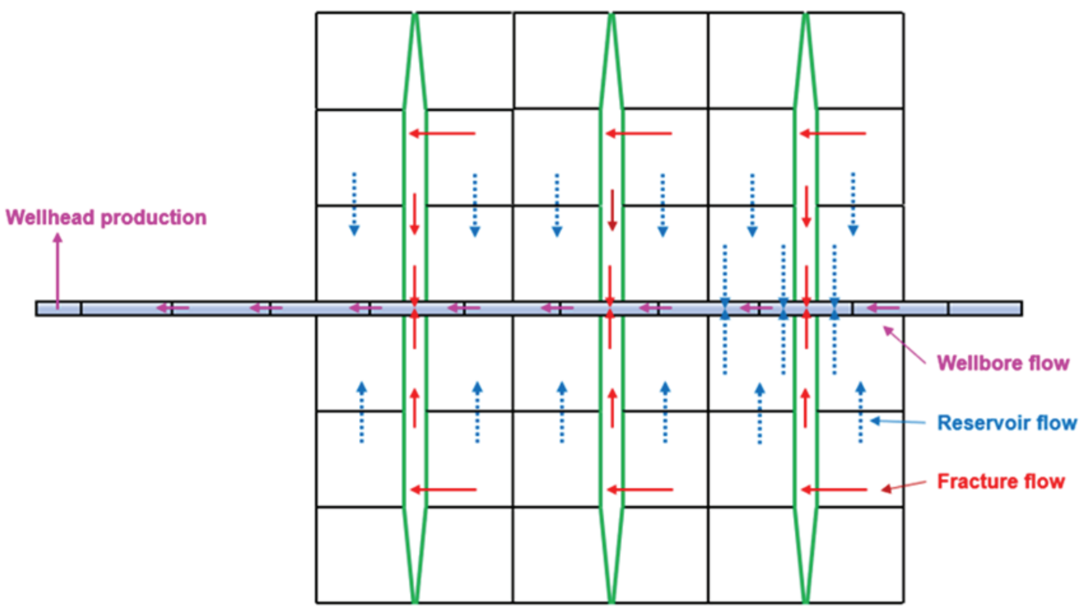

Figure 4.3: Illustration of the numerical fracture-reservoir-wellbore system. The blue one-dimensional grid cells are the wellbore domain with the pink arrows indicating the wellbore flow. The green inner boundary faces are the fracture domain with the red arrows showing the fracture flow coupled with fluid flow within the reservoir and wellbore. Blue dashed arrows represent the reservoir flow and wellbore coupling is considered if the corresponding wellbore section is open hole.

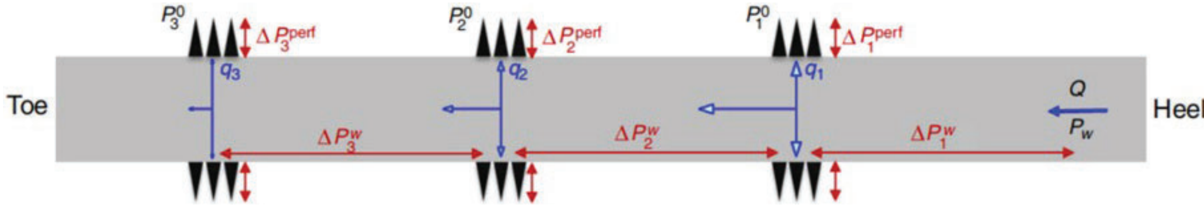

Figure 4.4: Flow distribution between multiple perforation clusters by accounting for the pressure drop in the well sections and the perforations (Manchanda et al., 2020).

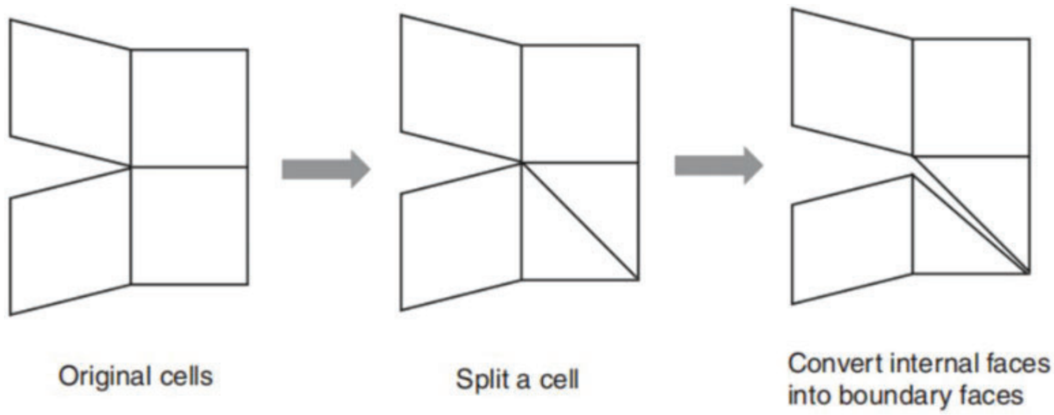

Figure 4.5: Fracture turning enabled by splitting cells diagonally (Manchanda et al., 2020).

5. Monitoring Fracture Growth using Distributed Strain Sensing

5.1 Monitoring EGS Fracture Propagation with Fiber Optics

To ensure efficient heat extraction and sustained circulation, hydraulic fractures generated from the injection well must intersect the production well, thereby establishing continuous and conductive fluid pathways (Jurick et al., 2025). Consequently, the ability to monitor and characterize fracture propagation is essential for evaluating the geometry, extent, and inter-well connectivity of the stimulated fracture network.

Using the Rayleigh frequency shift based distributed strain sensing (DSS-RFS), the team continuously monitored fracture stimulation events originating from the adjacent injection well. These measurements enabled the detection of fracture-driven interactions, commonly referred to as “frac hits”, along the production well (Figure 5.1). The insights from the fiber optic data were then used to guide the design and placement of perforation clusters in the production well. This data-informed strategy resulted in successful hydraulic fractures that effectively linked the injection and production wells, as later confirmed by cross-well circulation tests conducted after well stimulation (Ou et al., 2025b).

Analysis of fracture-driven interaction signals, as captured in fiber-optic strain rate waterfall plots, reveals notable discrepancies between the perforation locations in the injection well and the corresponding fracture intersection points along the production well (Figure 5.2). These observations indicate that hydraulic fractures undergo significant reorientation and turning during multi-stage stimulation, particularly in the later stages of the treatment. A detailed understanding of fracture geometry is, therefore, critical for optimizing future well placement and completion strategies in Enhanced Geothermal Systems. The large number of design parameters for a fracturing operation makes a multi-variate optimization approach difficult to implement in practice. In this context, numerical simulation serves as a valuable tool for demonstrating the driven mechanisms governing fracture propagation and reorientation in large-scale EGS well stimulations.

5.2 Model Setup

In this section, we introduce the Base Case used for modeling and interpreting the fiber optic strain change rate data acquired from the FORGE April 2024 injection well stimulation. The computational mesh for the two-dimensional reservoir domain is presented in Figure 5.3. The size of the simulated domain is $1000 \times 800 \times 120m^3$, and the number of grid blocks in the x, y and z directions are 200, 80 and 1, respectively.

A uniform fracture height of 120m is assumed in our two-dimensional fracture propagation simulation in the X-Y plane. The Base Case assumes that the fracture reorientation primarily happens in the X-Y plane (the X-Y distance between the injection well 16A and the production well 16B is 60m) due to the smaller in-situ stress contrast, while fracture growth in the X-Z plane (the X-Z distance between the injection well 16A and the production well 16B is 110m) was discussed in later sections. Difference in the sizes of an individual grid block along the X and Y directions provides smoother fracture turning along diagonals of the reservoir mesh. Dynamic mesh refinement is applied around the hydraulic fractures to support a more accurate calculation of stress and strain distribution among multiple created fractures. This also ensures enough meshing resolution for outputting the strain change rate responses along the production well locations for generating the fiber optic modeling data. A zero gradient boundary condition is used for the flow simulation, while a fixed zero-displacement/zero-shear boundary condition is imposed for the rock deformation simulation.

The Base Case simulates the 3-day multi-stage hydraulic fracturing treatments at the Utah FORGE site in April 2024 in well 16A (from stage 3R to stage 9). Modeling inputs for the fracturing injection schedule are depicted in Figure 5.4 based on the actual pumping schedule for well 16A. Field completion design parameters for well 16A (Table 5.1) were used for calculating the cluster location and perforation pressure drop for each hydraulic fracture (one fracture is assumed in each perforated cluster). The multi-stage hydraulic fracturing simulation is set-up according to reservoir parameters and in-situ conditions specific to the Utah FORGE site. The general fracture-reservoir simulation inputs for the Base Case are summarized in Table 5.2.

5.3 Results and Discussion

The stimulation treatments in well 16A (from stage 3R to 9) were simulated in the Base Case considering the effect of poro-elasticity. Reservoir stress and strain distribution in multi-stage stimulation are accurately captured through dynamic mesh refinement around all created fractures (Figure 5.5). These coupled fracture-reservoir modeling results provide critical insights into the fracture reorientation and turning suggested by the fiber optic monitoring data. Key factors affecting the geometry of the created fracture network such as in-situ stress contrast, poro-elasticity, thermo-elasticity and fracture-fault interaction are discussed in subsequent sensitivity cases.

5.3.1 Base case results

Fracture geometry and reservoir stress distribution at the end of the Base Case simulation are shown in Figure 5.6. Clear fracture reorientation is observed in the X-Y plane due to the stress shadowing effect adjacent to the created hydraulic fractures. Since normal “plug and perf” hydraulic fracturing treatment is employed in the Well 16A stimulation, fracture stages are perforated sequentially towards the heel. As a consequence, the stress shadow increases as more fracture stages are completed. Fractures in later stages turn more towards the heel and hit the producer at larger angles due to the cumulative stress shadow from stage 3R to stage 9.

The cumulative stress shadow and the extent of fracture turning from stage 3 to stage 9 lead to the clear discrepancies between the perforation locations in the injection well 16A and the corresponding fracture intersection points along the production well 16B in the Base Case simulation (Figure 5.7a). This agrees well with the "frac-hit" locations analyzed from the strain responses along the production well 16B through fiber optic monitoring during well 16A stimulation (signals of fracture driven interactions in the strain change rate waterfall plot as shown in Figure 5.2).

The fiber optic modeling data is outputted by sampling the reservoir deformation along the production well 16B (reservoir normal strain in the X direction). Unlike many Boundary-Element Method (BEM) based fracturing simulations that require post processing of the analytical displacement field to obtain the strain tensor in the reservoir, our integrated reservoir-fracture simulator always incorporates explicit reservoir meshing. Therefore, the normal strain, ε_X and corresponding strain rate, $\dot{\varepsilon_X}$ within the reservoir domain in the target direction can be numerically calculated by taking the gradient of the displacement field, $\tilde{u}$ (Eq. 5.1).

$$\tilde{\varepsilon} = grad(\tilde{u}), \qquad \dot{\varepsilon_X} = \frac{d\varepsilon_X}{dt} = \frac{\varepsilon_X^{n+1} - \varepsilon_X^{n}}{t^{n+1} - t^{n}} \tag{5.1}$$

The computed fiber optic strain change rate waterfall is generated by plotting the normal strain rate in the direction of production well 16B, $\dot{\varepsilon_X}$ against the locations along 16B and stimulation time (Figure 5.8). Classical "heart-shaped" strain rate signals are observed in earlier fracturing stages suggesting the time and locations of "frac-hits" at the monitor well (Liu et al., 2020). Asymmetric turning signals are observed, which corresponds to the fracture reorientation in the numerical modeling results (Figure 5.6). The gradient of the turning signal increases in later stages, suggesting the accumulating effect of stress shadow as the multi-stage hydraulic fracturing treatment proceeds. This shows that the fiber optic distributed strain sensing not only identifies the locations of fracture intersection but also monitors the patterns of fracture growth and reorientation before the fractures reach the monitor well.

5.3.2 In-situ stress contrast

The magnitude of in-situ stress contrast dominates the extent of fracture reorientation. A representative case was simulated incorporating stress contrast in the X–Z plane, using a constant fracture length of 120 meters. The resulting fracture geometry at the end of well stimulation, shown in Figure 5.9b, indicates that a high stress contrast significantly limits fracture turning, with only minor reorientation observed in stages 8 and 9. These results suggest that, under the strong X–Z stress contrast of the FORGE geothermal formation, vertical fracture propagation can be reasonably approximated as planar with negligible deviation. This observation supports the Base Case assumption that the observed discrepancies between the perforation positions in well 16A and the corresponding fracture intersections in well 16B are primarily a result of fracture reorientation occurring within the X–Y plane, where the stress contrast is comparatively lower.

Additionally, Figure 5.9 reveals pronounced cluster inefficiency during the stimulation of well 16A, particularly in stages 8 and 9, where several clusters received little fluid injection. Apart from stress shadowing, which inhibits both the propagation and fluid intake of fractures, the completion design of well 16A (as detailed in Table 5.1) further exacerbates fracture non-uniformity. The use of a high number of perforations per cluster leads to uneven fluid distribution and increased cluster-to-cluster variability in fracture growth.

5.3.3 Completion design

The April 2024 stimulation of well 16A at the FORGE site incorporated a large number of perforations (18-120 perforations) in each cluster results in apparent cluster inefficiency. Such inefficiency can be mitigated by modifying the completion strategy. One of the most effective and widely adopted techniques to address low cluster efficiency caused by stress shadowing and fracture competition is Limited Entry Perforation (LEP). By deliberately limiting the number of perforations per cluster, LEP increases backpressure at each entry point, maintaining sufficiently high injection pressure to promote a more balanced distribution of fluid across all clusters. This approach minimizes preferential growth toward the outermost or more compliant fractures.

The simulated fracture geometry of the case (with large X-Z stress contrast) employing LEP completion with 2 perforations in each cluster is presented in Figure 5.10b. LEP design yields significantly more uniform fracture lengths across stages and enhances the overall cluster efficiency since a more even fluid allocation across clusters is achieved. In common multi-stage hydraulic fracturing treatments of wells in unconventional reservoir, achieving good cluster efficiency is critical for increasing the contact area between the horizontal wellbore and formation. In the context of enhanced geothermal system, fracture uniformity assumes even greater importance, as it directly influences the hydraulic connectivity between the injection and production wells. Fractures that receive insufficient fluid during stimulation may fail to propagate to the production well and thus not contribute to long-term thermal energy extraction through fluid circulation. Therefore, achieving uniform stimulation across clusters is a key design objective for ensuring the optimum performance of EGS developments.

5.3.4 Influence of frac fluid rheology

Fracture geometry and reservoir Rheology of fracturing fluid significantly influence fracture propagation dynamics, proppant placement, and stress shadow development among adjacent clusters. During the April 2024 stimulation of well 16A at the FORGE site, various fluid types were employed across different stages. Specifically, slickwater was used in stages 3R, 4, 6, and 9, while crosslinked gel was injected in stages 5, 7, and 8. To investigate the influence of fluid rheology, the Base Case simulation was modified by increasing the viscosity of the fracturing fluid in stages 5, 7, and 8 by a factor of 200, reflecting the effect of crosslinked gel.

As shown in the simulated fracture geometry in Figure 5.11b, a noticeable increase is observed in both the average fracture length and fracture nonuniformity, particularly in stage 8. Higher fracturing fluid viscosity reduces the fluid leak-off rate at the fracture-reservoir interface, thereby enhancing the volume of fluid retained within the fracture. This promotes the development of longer and wider fractures, which in turn amplifies stress shadowing effects on adjacent fractures or inner clusters. Consequently, the fracture geometry becomes increasingly asymmetric, with outer clusters dominating propagation and inner clusters receiving limited stimulation, leading to reduced cluster efficiency. Despite the increased fracture growth, the magnitude of fracture turning remains unchanged. This is attributed to the stabilizing effect of high-viscosity fluids, which distribute pressure more uniformly along the fracture front. The resulting pressure homogeneity helps stabilize the fracture tip, reducing the chance of tip splitting, branching, or turning, leading to more planar fracture growth.

Parameters	Value
In-situ stress (MPa)	43.99, 47.89, 64.83
Young's modulus (GPa)	54.8
Poisson's ratio	0.26
Biot's coefficient	0.85
Reservoir permeability (μD)	5
Reservoir pore pressure (MPa)	2.355
Fluid compressibility (10^{-10}Pa^{-1})	5
Fluid viscosity (cp)	1
Fluid density (kg/m^3)	1000
Rock density (kg/m^3)	2700
Reservoir porosity	0.01
Rock tensional strength (MPa)	1
Rock thermal conductivity (W m^{-1}K^{-1})	2
Fluid thermal conductivity (W m^{-1}K^{-1})	1
Rock heat capacity (J kg^{-1}K^{-1})	890
Fluid heat capacity (J kg^{-1}K^{-1})	4184
Thermo-elasticity coefficient (10^{-6}K^{-1})	3.3
Formation temperature (K)	494
Fracture injection temperature (K)	324

Table 5.1: Well Completion Inputs for the Base Case.

Parameters	Value
In-situ stress (MPa)	43.99, 47.89, 64.83
Young's modulus (GPa)	54.8
Poisson's ratio	0.26
Biot's coefficient	0.85
Reservoir permeability (μD)	5
Reservoir pore pressure (MPa)	2.355
Fluid compressibility (10^{-10}Pa^{-1})	5
Fluid viscosity (cp)	1
Fluid density (kg/m^3)	1000
Rock density (kg/m^3)	2700
Reservoir porosity	0.01
Rock tensional strength (MPa)	1
Rock thermal conductivity (W m^{-1}K^{-1})	2
Fluid thermal conductivity (W m^{-1}K^{-1})	1
Rock heat capacity (J kg^{-1}K^{-1})	890
Fluid heat capacity (J kg^{-1}K^{-1})	4184
Thermo-elasticity coefficient (10^{-6}K^{-1})	3.3
Formation temperature (K)	494
Fracture injection temperature (K)	324

Table 5.2: Fracture and Reservoir Simulation Inputs for the Base Case.

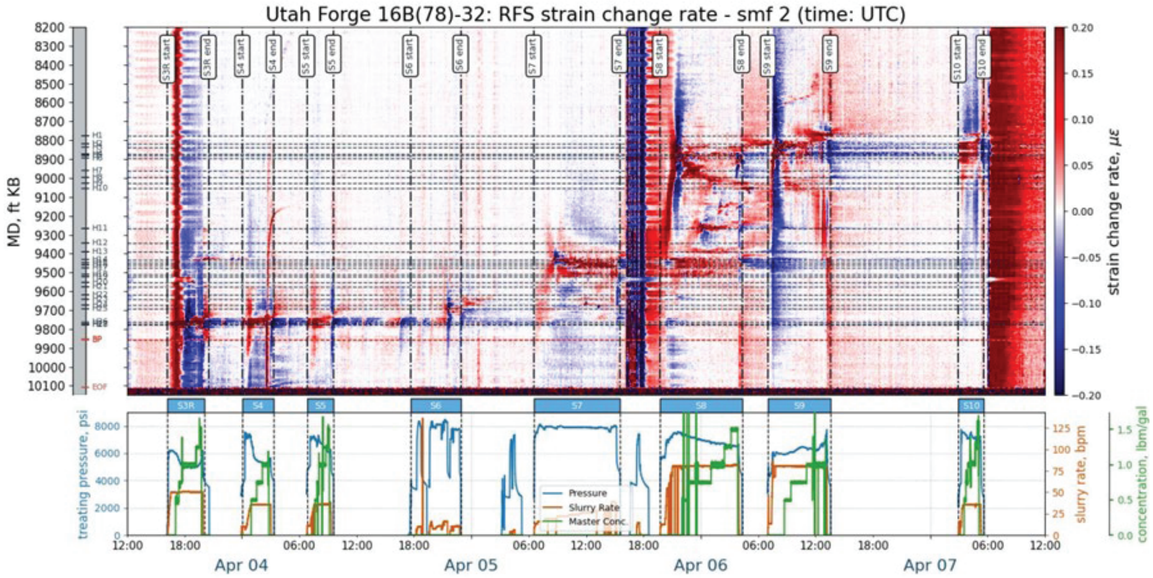

Figure 5.1: DSS-RFS strain change rate fiber optic monitoring along well 16B during the April 2024 stimulation of well 16A at the Utah FORGE site. (Jurick et al., 2025).

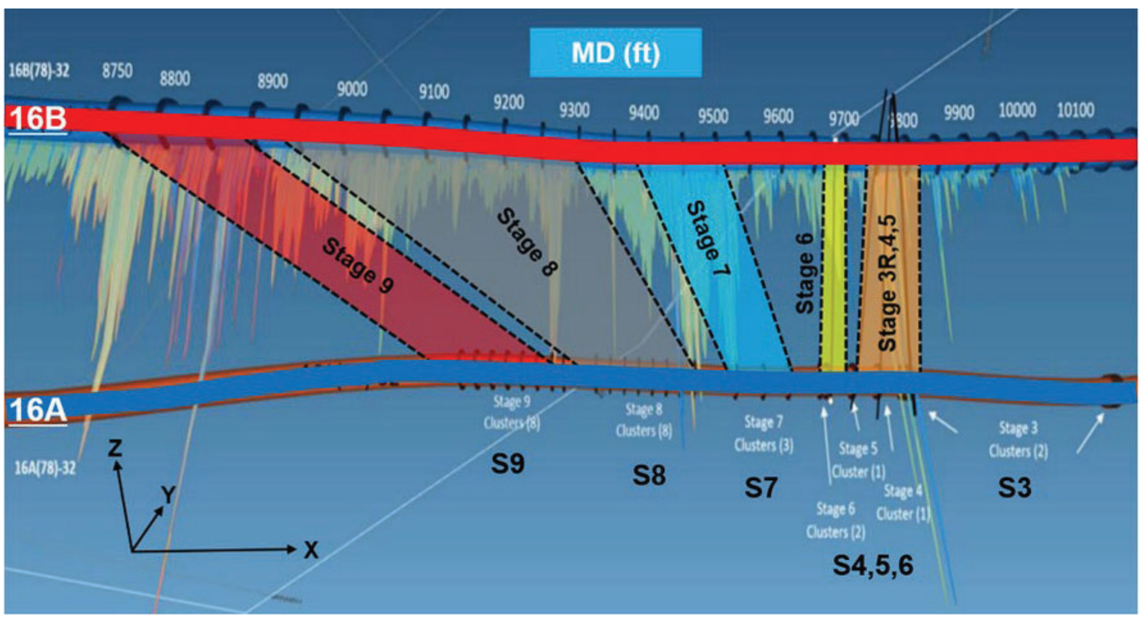

Figure 5.2: Approximate cross-well fracture intersections identified from fiber optic sensing data. Discrepancies between injector perforation locations and fracture intersections along the producer were identified, particularly in later stimulation stages (Modified from Jurick et al., 2025).

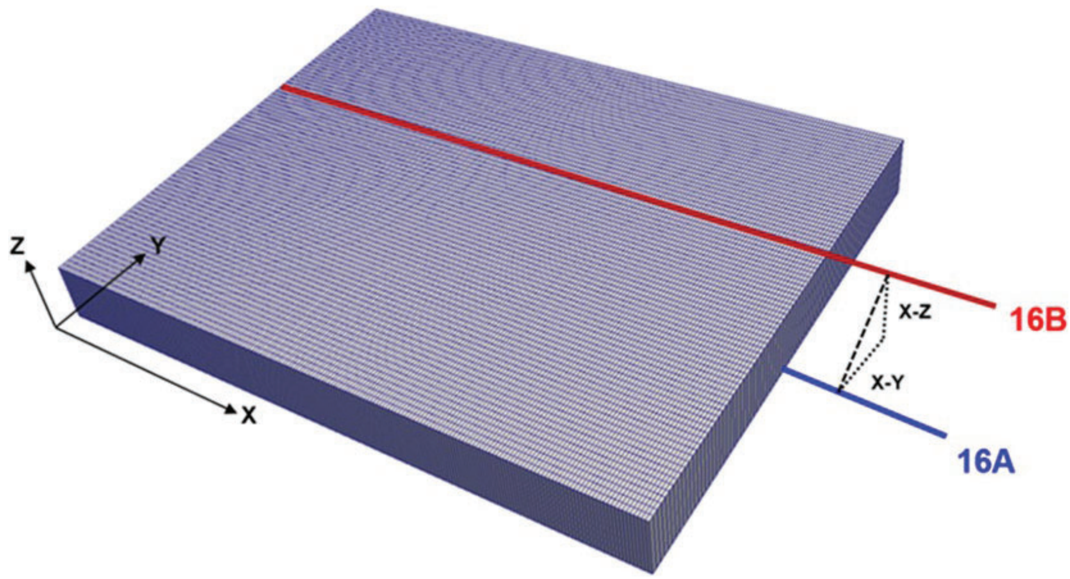

Figure 5.3: Computational mesh for the Base Case. A uniform fracture height of 120m is assumed for fracture propagation simulation in the X-Y plane. Fine global mesh and dynamic mesh refinement are employed to support a more accurate calculation of stress and strain distribution among multiple created fractures and ensure enough meshing resolution for outputting the fiber optic modeling data.

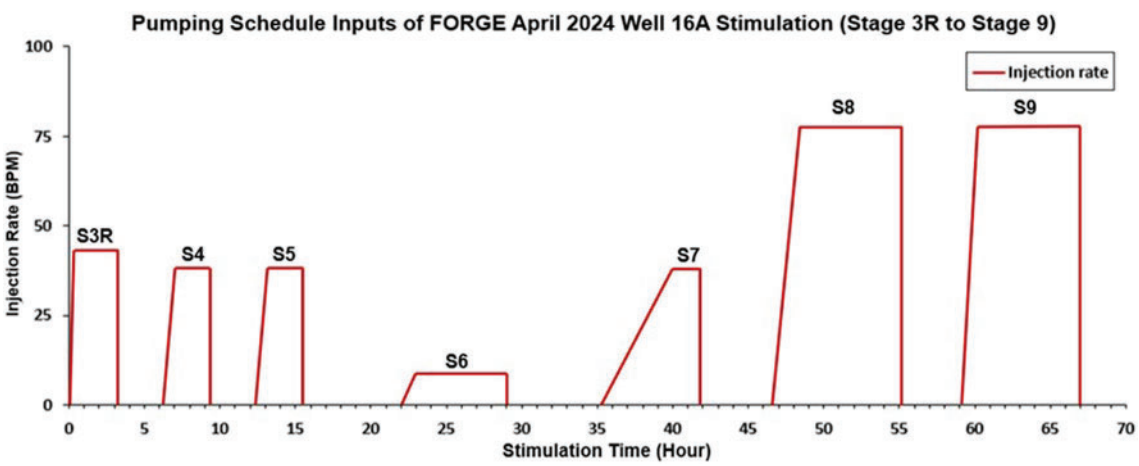

Figure 5.4: Pumping schedule modeling inputs for FORGE April 2024 well 16A stimulation (from stage 3R to stage 9).

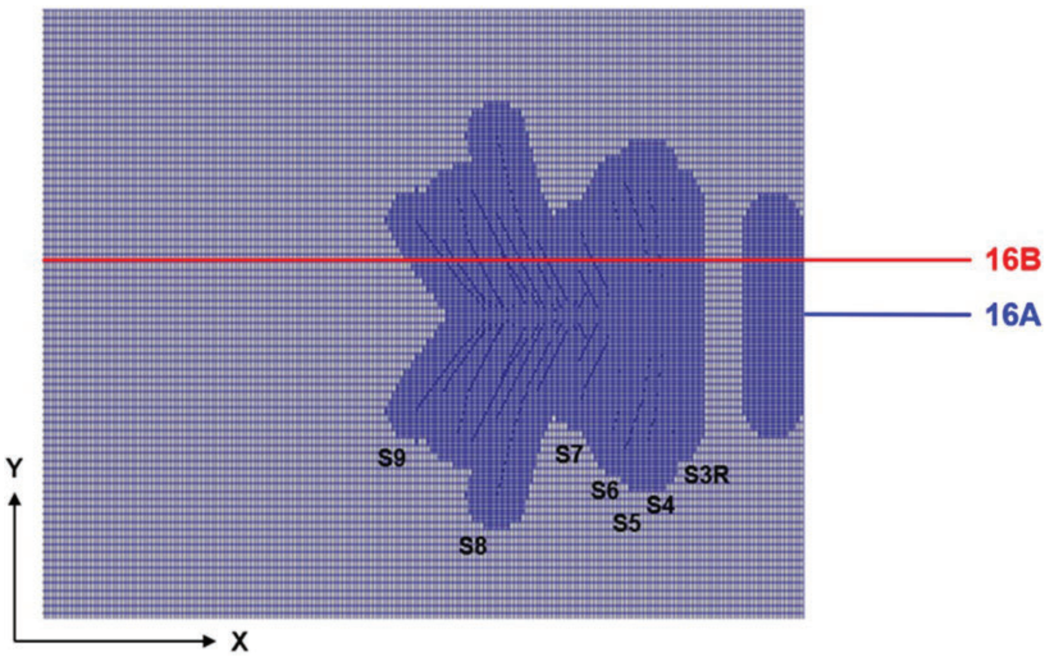

Figure 5.5: Reservoir and fracture mesh at the end of Base Case simulation with dynamic mesh refinement around created hydraulic fractures. Clear fracture reorientation is observed in the modeling results of well 16A stimulation from stage 3R to 9.

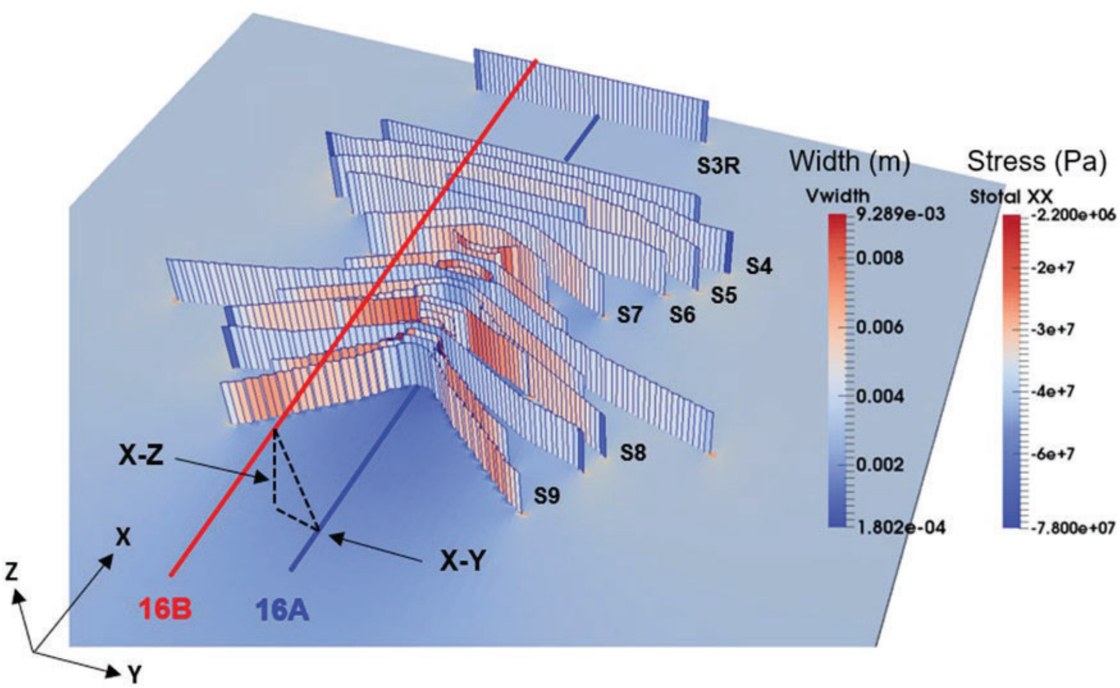

Figure 5.6: Final fracture geometry and reservoir stress distribution of the Base Case. Fractures reorient due to stress shadowing in the X-Y plane. Fractures in later stages turn more to the heel and hit the producer at larger angles due to the cumulative stress shadow from stage 3R to stage 9.

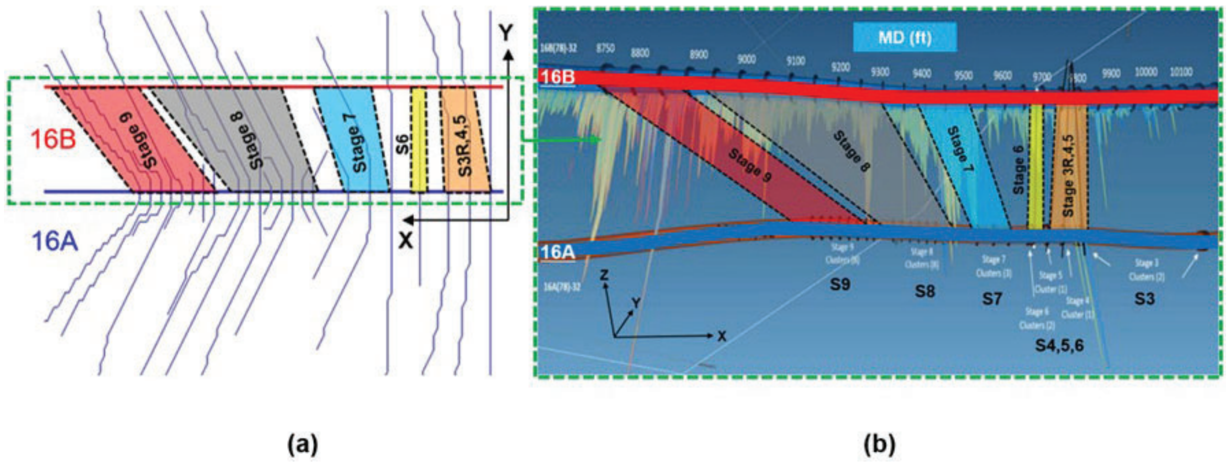

Figure 5.7: Discrepancies between the perforation locations in the injection well 16A and the corresponding fracture intersection points along the production well 16B. (a) Discrepancies observed in the Base Case simulation. (b) Discrepancies analyzed from the strain responses measured along the production well through fiber optic monitoring.

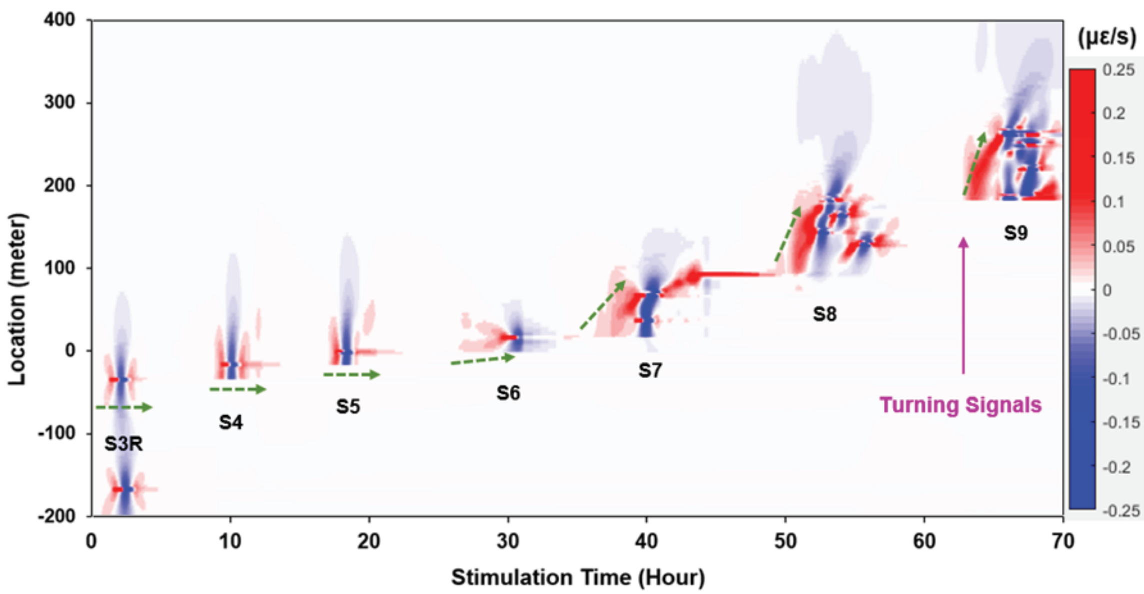

Figure 5.8: Fiber optic strain rate modeling results for the Base Case. "Red" shows tensional strain change and "Blue" implies compressional strain change. Classical "heart-shaped" strain rate signals are observed in earlier fracturing stages suggesting the time and locations of "frac-hits" at the monitor well. Unsymmetric turning signals are observed in later stages, which clearly shows fracture reorientation calculated from the numerical modeling results (consistent with fiber measurements).

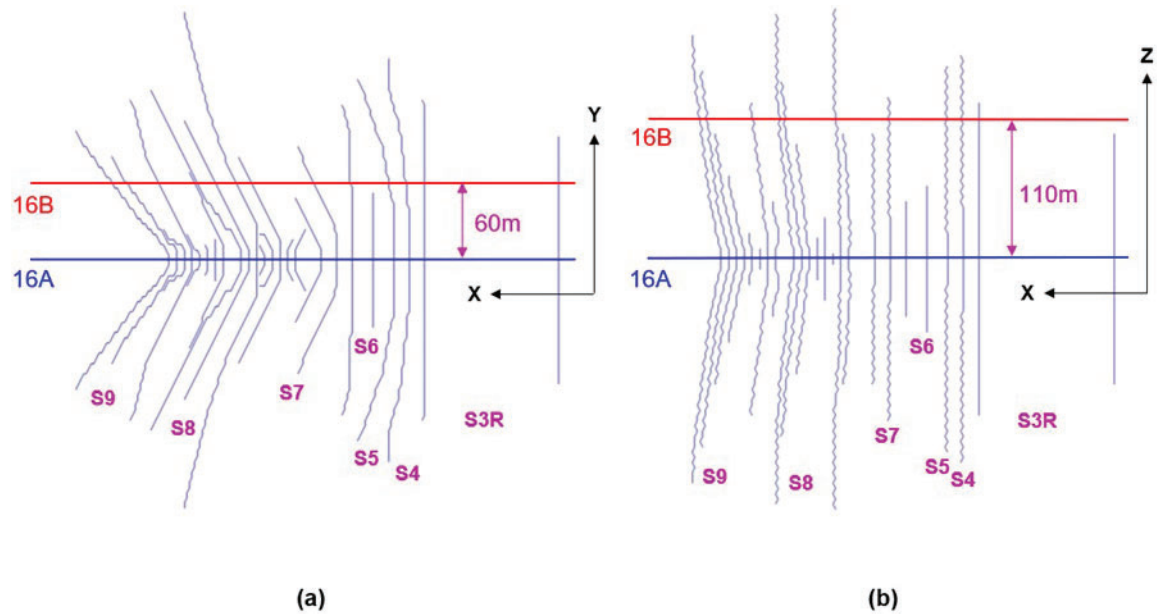

Figure 5.9: (a) Fracture geometry with in-situ stress contrast in the X-Y plane. (b) Fracture geometry with in-situ stress contrast in the X-Z plane. Fracture propagation is almost planar under a high stress contrast in the X-Z plane. The modeling results suggest a poor cluster inefficiency in well 16A stimulations.

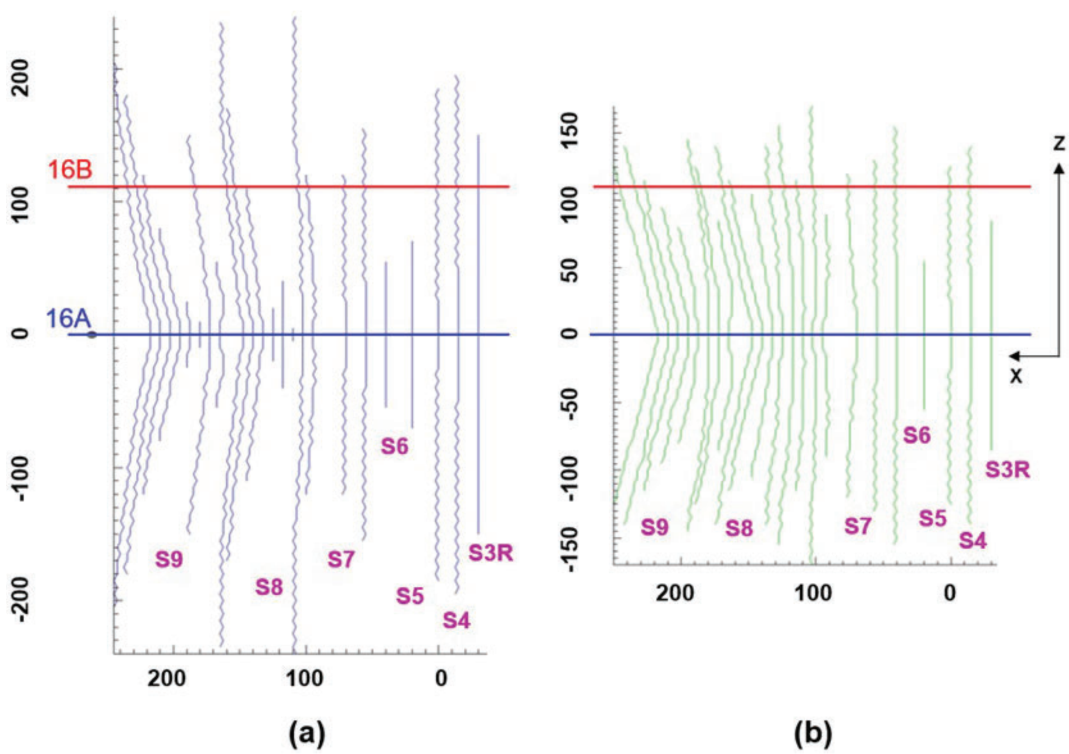

Figure 5.10: (a) Fracture geometry for well 16A. (b) Fracture geometry with limited entry completion design. Limited entry design yields significantly more uniform fracture lengths across stages and enhances the overall cluster efficiency.

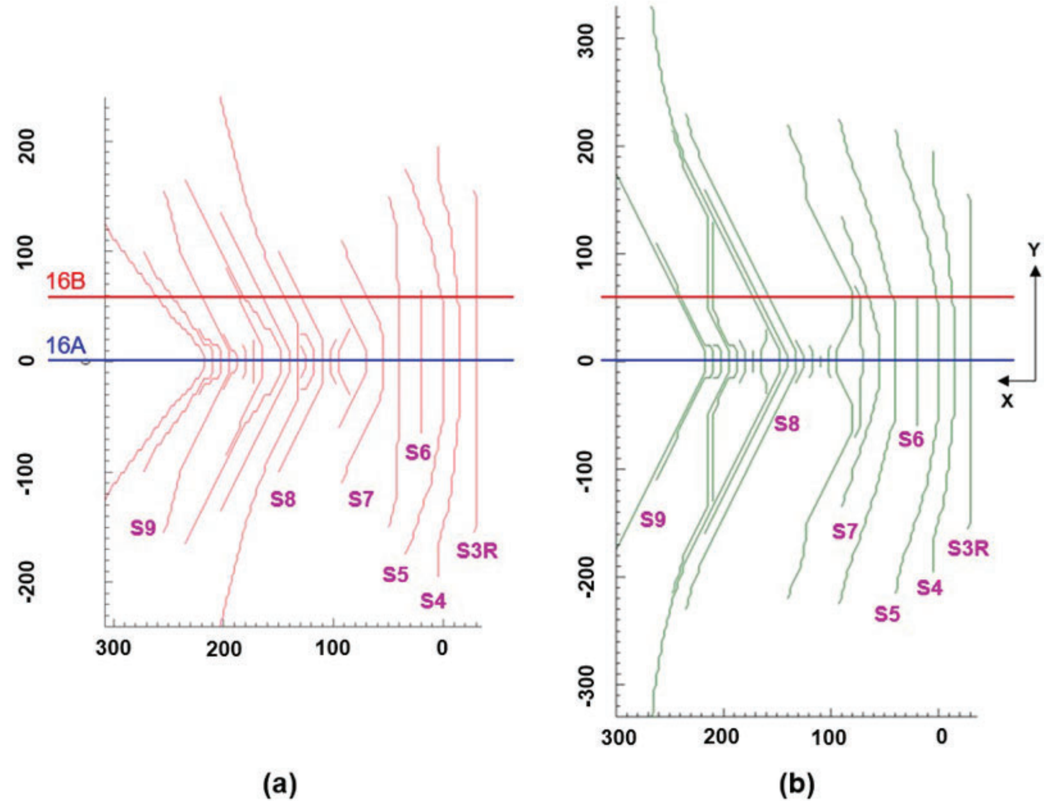

Figure 5.11: (a) Fracture geometry of the Base Case with all stages using slick water. (b) Fracture geometry of the case with cross-link gel used in stage 5, 7 and 8. A clear increase in fracture nonuniformity is seen in the biased fracture geometry in stage 8.

6. Monitoring Fluid Circulation at the Forge Site (Circulation Test 1) Using Thermo-Hydro-Mechanical Models and Fiber-Optic Distributed Strain Data

6.1 July 2023 Circulation Test

Beyond the characterization of fracture geometry obtained during stimulation, fiber-optic data acquired during fluid circulation provides a more direct approach to interpreting the hydro-mechanical behavior of fractures intersecting the production well in an Enhanced Geothermal System (EGS) (Liu et al., 2023). During hydraulic fracturing operations, distributed strain rate measurements recorded along fiber-optic cables are commonly visualized as waterfall plots, where strain rate is plotted as a function of measured depth and time. As discussed in the previous chapter, distinctive strain rate signal patterns within these plots can be used to assess fracture growth and intersection at the monitor well. Similarly, during geothermal circulation, the fiber optic distributed strain rate waterfalls reveal the presence of intersecting fractures with varying fracture conductivity and associated stimulated reservoir volume (Ou et al., 2024). These real time measurements enable operators to assess the spatial heterogeneity along the EGS producer.

At the Utah FORGE EGS test site, three initial stages of hydraulic fracturing (Stages 1 to 3) were completed in April 2022, followed by additional stimulation from Stage 3R through Stage 10 in April 2024. Further fracturing stages are planned for future operations. The target formation beneath the FORGE site comprises hot, dry crystalline rock with a high density of natural fractures. This geological setting is conducive to the formation of complex hydraulic fracture networks, including small-scale branches and secondary fractures.

During the July 2023 fluid circulation test, a constant injection rate was maintained to minimize additional fracture propagation during circulation, as illustrated by the red curve in Figure 6.1. A large pressure buildup at the injection well, depicted by the blue curve, suggests significant formation resistance to fluid flow between the injector and the producer. The gray dots represent the measured production rates at the producer well 16B. Although the injection and production rates are plotted on separate axes, it is evident that the initial production rate was significantly lower than the injection rate, with a gradual increase observed over time. This pressure–rate behavior indicates that the initial three fracture stages in well 16A failed to generate sufficiently conductive pathways to the producer. Consequently, a large portion of the injected fluid was temporarily retained within the formation.

In the fiber-optic distributed strain rate waterfall plot, distinct tensile strain rate signals, indicated by red color, are observed within the zone of interest (Figure 6.2), reflecting an overall expansion of the formation in response to fluid injection. These strain responses were initially hypothesized to result from thermally induced stress, whereby the injection of cold fluid into the formation would lead to thermal contraction of the rock matrix and subsequent fracture opening. However, this mechanism does not fully explain the observed strain behavior. If thermal contraction were the dominant driver, one would also expect to observe compressive strain signatures associated with bulk rock shrinkage. Instead, the strain rate data predominantly exhibits tensile behavior, with no corresponding compressive regions evident in the plot. Furthermore, thermal induced deformation is insufficient to account for tensile strain signals occurring only during specific intervals of the circulation test. These findings point to alternative mechanisms, such as pore pressure-driven mechanical responses or fracture-fluid interactions.

6.2 Model Setup

Based on the Utah FORGE geothermal formation, we set up coupled thermo-mechanical models to study the thermal and mechanical transients of general geothermal circulation. A 3-D base case is set up for modeling the fluid circulation with one main planar fracture. The computational mesh for the simulated reservoir domain is presented in Figure 6.3 with the producer 16B placed 120 meters above the injector, 16A. The simulated geothermal domain is $160 \times 60 \times 200\, m$, and the number of original reservoir grid cells in the x, y and z directions are 80, 12 and 40, respectively. Two levels of mesh refinement are implemented around the fracture faces, with a refined mesh size of 0.5m along the wellbore trajectory. This approach ensures sufficient spatial resolution in the simulation results to accurately capture local strain changes near the fracture. For the flow simulation, a zero-gradient boundary condition is applied, while a fixed zero-displacement boundary condition is used for the geomechanics simulation.

From some of the previous modeling work on hydraulic fracture propagation in natural fracture networks (Meng, et. al, 2023) and based on micro-seismic data that is obtained at the Utah FORGE site, the main fracture propagation is expected to be primarily planar (Figure 6.4). The main planar fracture is assumed to be surrounded by small fracture branches due to its interaction with natural fractures. The small reactivated natural fracture branches are represented as a mechanical stimulated reservoir volume (mechanical SRV) around the main hydraulic fracture in this work

(Figure 6.4). We refer to this volume as the mechanical SRV because it is created by the mechanical opening of the main hydraulic fracture. In this region near the main hydraulic fracture the permeability of the formation is assumed to be higher by a factor of 10 to represent a typical permeability enhancement in the SRV region. The mechanical properties of the formation within this SRV are also altered as shown in Table 6.1 due to the abundance of reactivated natural fractures. This is an approximation made to simplify the complex nature as the SRV that is well known to exist around the main fractures.

General porous and mechanical inputs of both the original hot-dry-rock formation and the mechanical SRV are summarized in Table 6.1 for the Base Case. These reservoir properties are set according to the Utah FORGE formation. The mechanical SRV differs from the reservoir in terms of permeability and formation compressibility. Geothermal inputs such as reservoir/injection temperature and fracture surface contact force inputs are listed in Table 6.2. The base model simulates an 8-hour fluid circulation with a constant injection rate of 0.002 m^3/s considers the effect of poro-elasticity and thermo-elasticity.

6.3 Results and Discussion

In this section, thermo-hydro-mechanical modeling results for fluid circulation for the Base Case are presented. Pressure, temperature and induced strain evolution are shown for both the fracture and reservoir, revealing the mechanisms that cause these changes in the distributed strain rate response and are detected by the fiber optic cable along the producer. Subsequently, we show sensitivity cases to demonstrate how the fiber optic strain rate waterfall is affected by fracture and the reservoir property changes within the mechanical SRV.

6.3.1 Base case results

The created hydraulic fracture gradually closes on either proppant or on its surface asperities (with no proppant pumped) during post-frac closure. The fracture width is dynamically updated within our simulation. The initial fracture width (before fluid circulation) is small since the fracture supports the large difference in the minimum horizontal stress and fluid pressure within the fracture. This leads to low initial fracture conductivity and high formation resistance to fluid flow. A large pressure build-up is seen in the formation (Figure 6.5a) as recorded in the field well injection data. As the pressure inside the fracture is increased by thousands of psi, the fracture will dilate during fluid circulation. Due to the gradual opening of the fracture and the fluid storage in the mechanical SRV, it takes hours (Figure 6.5b) for the pressure build up front to travel from the injector to the producer (formation compressibility is high within the surrounding SRV).

The fracture pressure, fracture width and fracture temperature distribution across the fracture surface at 3 selected simulation times are presented in Figure 6.6. The fracture pressure closely aligns with the fracture width evolution, as the fracture gradually opens along its length as the pressure front travels through the fracture. Fracture conductivity increases with the opening of the fracture. The injection of cold fluid will decrease the temperature within the reservoir and fracture. Due to thermo-elasticity, the fracture width will also increase under the effect of reservoir cooling. Temperature change and thermal elasticity have a larger effect on fracture dilation but is mainly restricted near the injection well, while it also increases the injectivity of the fracture reservoir system. The fracture pressure and width evolution explain the production rate data that is recorded on the Forge site. The production rate generated from the circulation model Figure 6.7) has the same trend as the field production data. The overall production rate is small during the early stages of injection due to the small initial fracture width and fluid storage in the mechanical SRV. As is mentioned in Figure 6.6, the pressure front from the injector takes hours to reach the producer, and before that we do not see much fluid production. Production will gradually increase due to the gradual dilation of the fracture until the entire fracture-reservoir system stabilizes into a more conductive pathway for fluid to flow.

Pore pressure and the induced strain across the reservoir during EGS fluid circulation, are shown in Figure 6.8 during EGS fluid circulation. The strain rate is the signal that is monitored by the fiber optic cable at the producer. As the pressure front is travelling through the fracture, there is an induced tensional strain front travelling with the pressure front. There is also a second compressional strain front caused by the temperature change, but it takes a long time for it to be sensed by the fiber along the producer and is out of the scope of this work (cooling front will arrive much later after all the heat has been recovered from the rock). When the induced strain front reaches and passes by the producer (where the fiber is deployed), we clearly see the corresponding strain rate signal.

By plotting the strain rate along the production well against circulation time, the fiber optic strain rate waterfall plot is generated and depicted in Figure 6.9. The general drop-like shape of this modeling result matches well with the Forge fiber monitoring data for an anticipated single fracture region. This basically explains why the extensional strain rate signal occurs in the fiber monitoring plot within only a certain amount of time. It indicates the approaching and passing by of the tensional strain rate front at early transient fluid circulation.

6.3.2 Fracture stiffness

A series of sensitivity cases are modeled for studying how the fiber optic strain rate signal can be used for evaluating the enhanced geothermal system in terms of fracture conductivity, the size of simulated reservoir volume and property changes within the SRV.

The induced strain front monitored by the fiber optic is mainly determined by the dynamic fracture permeability and property change in the mechanical SRV. In our model, the dynamic fracture permeability is determined by fracture stiffness. Usually, a well propped fracture with a higher value of stiffness will have a higher fracture permeability and a smaller dynamic change of fracture permeability. From Figure 6.10, a larger value of fracture stiffness will make the tensional strain rate signal occur earlier and last longer on the fiber optic strain rate waterfall plot. The pressure front travels faster in a well propped fracture with larger average conductivity, and the induced strain front arrives earlier at the fiber optic cable. When the fracture conductivity is higher, more injected fluid will directly flow through the fracture towards the producer instead of spreading into the surrounding SRV. Therefore, pressure build up in the SRV takes longer, and the induced strain front is observed to be longer across the formation in the simulation cases with larger fracture stiffness. This leads to a corresponding longer strain rate signal that occurs earlier at the producer.

6.3.3 SRV formation compressibility

Three parameters are defined in this work regarding property changes in the SRV: formation compressibility, formation Young’s modulus and the size of SRV. According to Figure 6.11, a higher value of formation compressibility will make the tensional strain rate signal occur later and last longer on the fiber optic waterfall plot. The SRV compressibility affects its ability to store the injected fluid.

When the formation compressibility is larger, the SRV receives more injected fluid during fluid circulation. This decreases the traveling speed of the pressure build up front to the production well thus the stain rate signal occurs later in the fiber optic waterfall. Similarly to the effect of large fracture conductivity, pressure build up also takes longer when SRV compressibility is larger. As a result, the length of the tensional strain rate signal is also larger.

6.3.4 SRV deformability

The formation Youngs' modulus within the mechanical SRV generally determines how deformable the SRV is, so it will not affect the flow solution within the system. Hence, both the arrival time and length of the strain rate signal will not change with the change of SRV Youngs modulus. Formation Young's modulus mainly affects the magnitude of the strain rate signal. Figure 6.12 shows that a smaller SRV Youngs modulus will result in a higher value of strain rate while its length and arrival time is not affected.

6.3.5 SRV size

Like formation compressibility, SRV size also determines its ability to store the injected fluid. Pressure build-up time is longer since the porous volume available for fluid storage is larger (Figure 6.13). As a consequence, a larger SRV size will make the signal occur later and last longer in the waterfall plot. The size of the mechanical SRV also affects the size of the strain rate signal. Larger SRV size leads to a wider signal width.

6.3.6 Multi-fracture simulation setup

During hydraulic fracturing, a well-stimulated cluster typically generates a dominant fracture with a large dynamic aperture. Such fractures are expected to induce the formation of additional secondary branches within the surrounding stimulated reservoir volume (SRV) that receive higher energy input during the fracturing treatment. The resulting mechanical SRV is characterized by an enhanced capacity to store injected fluids during subsequent circulation. Consequently, these zones are generally associated with reduced effective Young's modulus and increased formation compressibility. This conceptual understanding aligns with observations from the Utah FORGE fiber-optic monitoring data. Within the designated zone of interest, both early and prolonged tensile strain rate signals of higher magnitude, as well as later and shorter tensile responses of lower magnitude, were recorded. These variations are indicative of fractures intersecting the producer well that exhibit differing hydraulic conductivities.

To further examine the mechanical signatures of strain rate responses observed in the distributed strain rate waterfall plots and to replicate the trends noted in the FORGE July 2023 circulation test, a multi-fracture numerical model comprising five fractures was constructed (Figure 6.14). Each fracture was assigned with distinct stiffness and SRV properties, as summarized in Table 6.3, to represent the mechanical heterogeneity inferred from field observations.

6.3.7 Multi-fracture modeling results

Evolutions of fluid pressure inside the fracture, dynamic fracture width and fracture fluid temperature during EGS circulation of the multi-fracture simulation case are illustrated in Figure 6.15. Notably, the first and fifth fractures are assigned with higher stiffness values, and as a result, are expected to exhibit greater dynamic fracture conductivity during circulation. These fractures also correspond to better-stimulated clusters, which are presumed to be associated with larger stimulated reservoir volumes and enhanced formation compressibility and deformability. The pressure distribution plots reveal that the pressure fronts in the first and fifth fractures propagate more rapidly compared to those in the three centrally located fractures. This behavior indicates lower flow resistance and higher transmissivity in the outer fractures. Similarly, the fracture fluid temperature plots show more significant cooling effects concentrated in these two outermost fractures, suggesting that a larger portion of the injected fluid preferentially flows into these higher-conductivity pathways. The temperature contrast between outer and inner fractures further confirms the dominance of the first and fifth fractures in governing overall fluid distribution during the circulation process. These observations highlight the influence of fracture mechanical property on its hydrothermal behavior during EGS operations.

Figure 6.16 presents the fiber-optic modeling results from the five-fracture simulation case for matching the FORGE distributed strain monitoring data from July 2023 EGS circulation at the Utah FORGE test site. In the modeled fiber-optic strain rate waterfall plot, the first (topmost) and fifth (bottommost) fractures exhibit prominent tensile strain signals that appear earlier, persist longer, and display greater magnitudes relative to the intermediate fractures. These trends are consistent with the simulation input, where the outer fractures were assigned with higher fracture conductivity, greater SRV compressibility, and smaller Young's modulus. The correspondence between strain rate responses and fracture properties confirms that the distributed strain data effectively identify these two fractures as the primary flow pathways within the system. Although it remains challenging to identify "dead-end" fractures (fractures that intersect the production well but do not contribute to flow due to a lack of upstream connectivity as introduced by Meng et al., 2023) based solely on early-time fiber-optic responses, the distributed strain data provides valuable insight into the spatial variability in fracture conductivity across the stimulated zone. These results highlight the potential of distributed fiber-optic sensing to serve as a diagnostic tool for characterizing fracture conductivity and heterogeneity in multi-stage EGS developments.

Parameters	Reservoir Value	SRV Value
In-situ stress (MPa)	43.99, 49.49, 64.11	43.99, 49.49, 64.11
Young's modulus (GPa)	54.8	54.8
Poisson's ratio	0.26	0.26
Biot's coefficient	0.8	0.8
Pore pressure (MPa)	25.35	25.35
Reservoir porosity	0.01	0.01
Permeability (μD)	5	500
Formation compressibility (10^{-11}Pa^{-1})	5	10
Fluid compressibility (10^{-10}Pa^{-1})	5	5
Fluid viscosity (cp)	1	1

Table 6.1: Mechanical and reservoir parameters of the base case.

Parameters	Value
Reservoir temperature (K)	503
Injection temperature (K)	323
Initial contact width (m)	0.001
Fracture stiffness (Pa)	3×10^8
Wellbore diameter (m)	0.12

Wellbore roughness (μm)	0
Production skin	10

Table 6.2: Thermal and fracture contact parameters.

Fracture	Stiffness (Pa)	SRV Compressibility (Pa^{-1})	SRV Youngs' Modulus (GPa)	SRV Size (m)
1	8.5×10^8	2.5×10^{-10}	39.8	4
2	6.4×10^8	1.0×10^{-10}	52.8	4
3	6.3×10^8	1.0×10^{-10}	50.8	4
4	6.5×10^8	1.25×10^{-10}	46.8	4
5	7.0×10^8	1.25×10^{-10}	43.8	4

Table 6.3: Fracture and stimulated reservoir volume of the multi-fracture case.

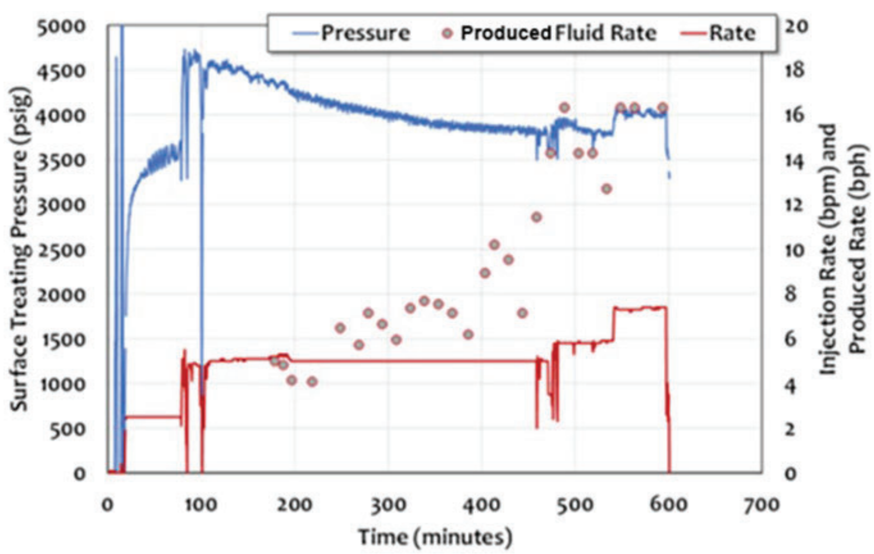

Figure 6.1: The rate-pressure data recorded during the second circulation test at the Utah FORGE site.

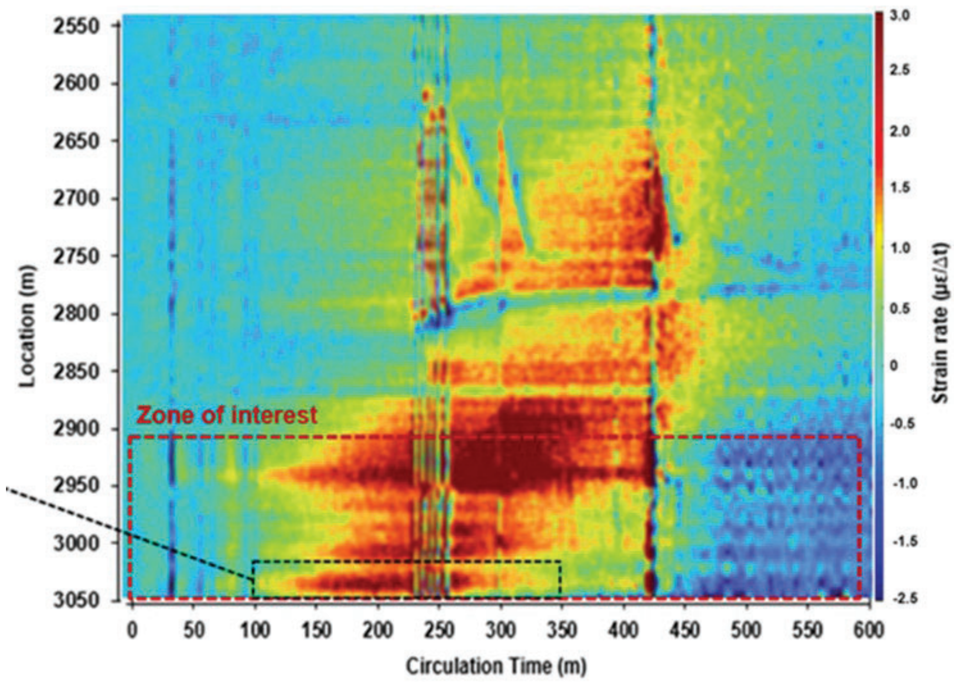

Figure 6.2: Approximate cross-well fracture intersections identified from fiber optic sensing data. Discrepancies between injector perforation locations and fracture intersections along the producer were identified, particularly in later stimulation stages (Modified from Jurick et al., 2025).

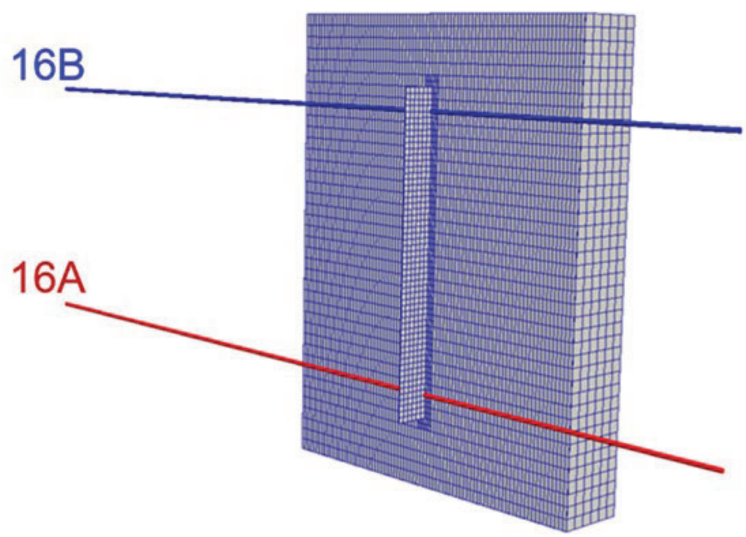

Figure 6.3: The mesh specified for the Base Case with one main planar fracture. The numerical geothermal domain is 160m x 60m x 200m. The producer 16B is placed 120 meters above the injector 16A. Mesh refinement is applied around the main planar fracture.

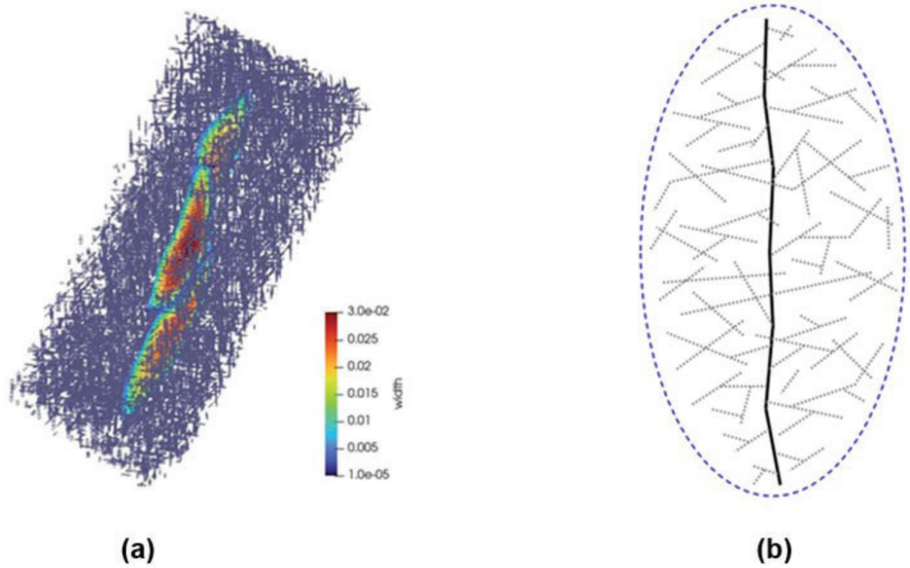

Figure 6.4: (a) Numerical study of modeling hydraulic fracture propagation in a natural fracture network (Meng et al, 2023); (b) Fracture branches represented as a mechanical simulated reservoir volume around the main hydraulic fracture.

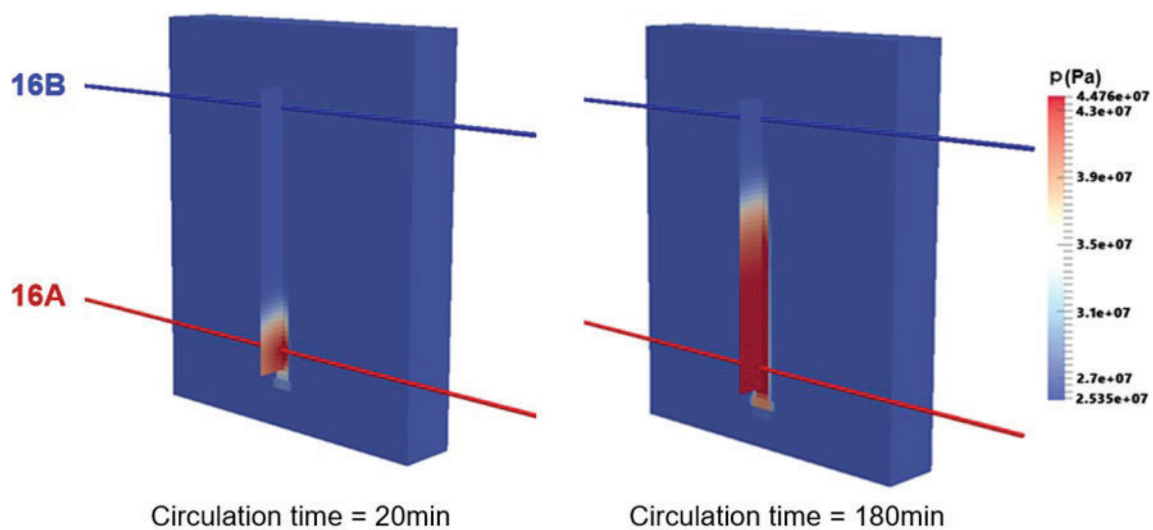

Figure 6.5: Formation pressure evolution during early fluid circulation for the Base Case. (a) Large pressure build up is seen at the fracture; (b) It takes hours for the pressure build up front to travel from the injector to the producer.

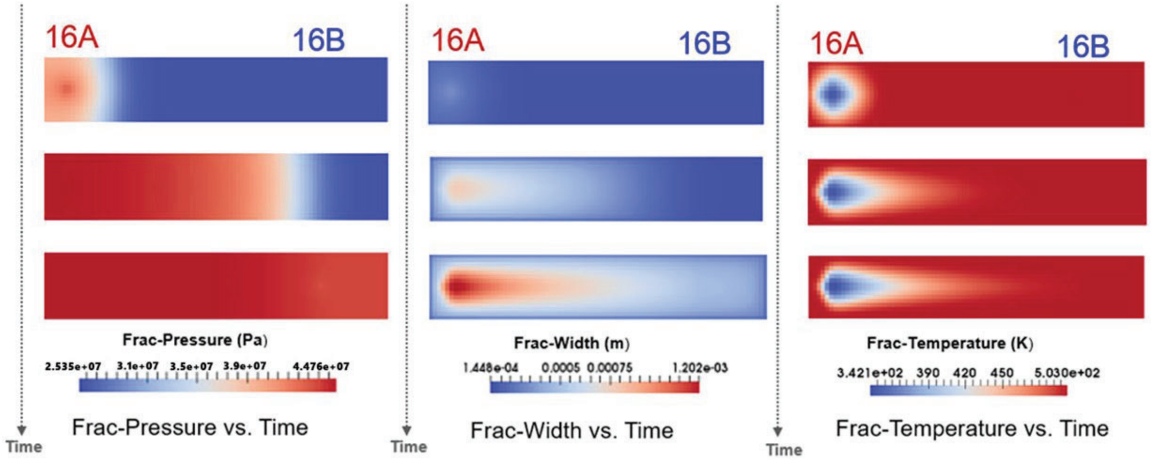

Figure 6.6: Fracture evolution during EGS circulation. (a) Fracture pressure evolution; (b) Fracture width evolution; (c) Fracture temperature evolution.

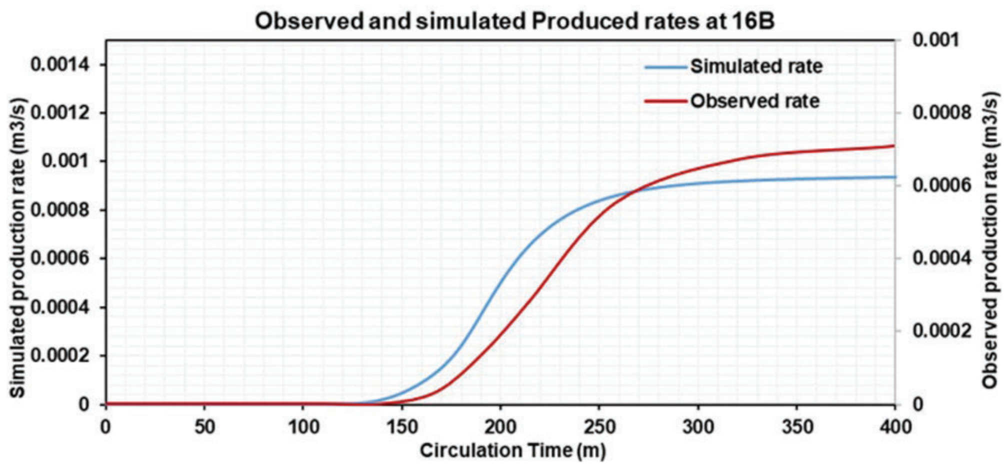

Figure 6.7: Averaged observed production rate and simulated production rate from the EGS producer.

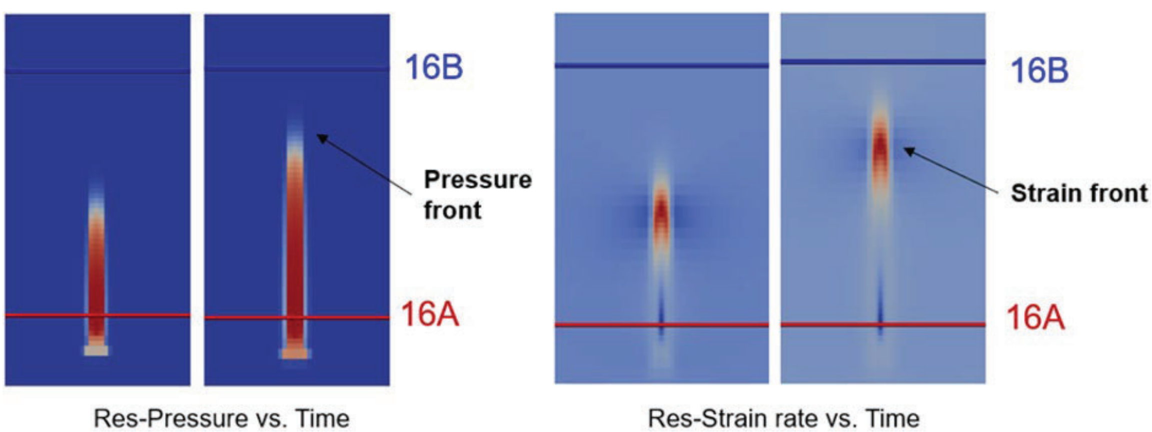

Figure 6.8: The induced strain front is traveling with the pressure front. (a) Pore pressure evolution; (b) The induced strain front evolution.

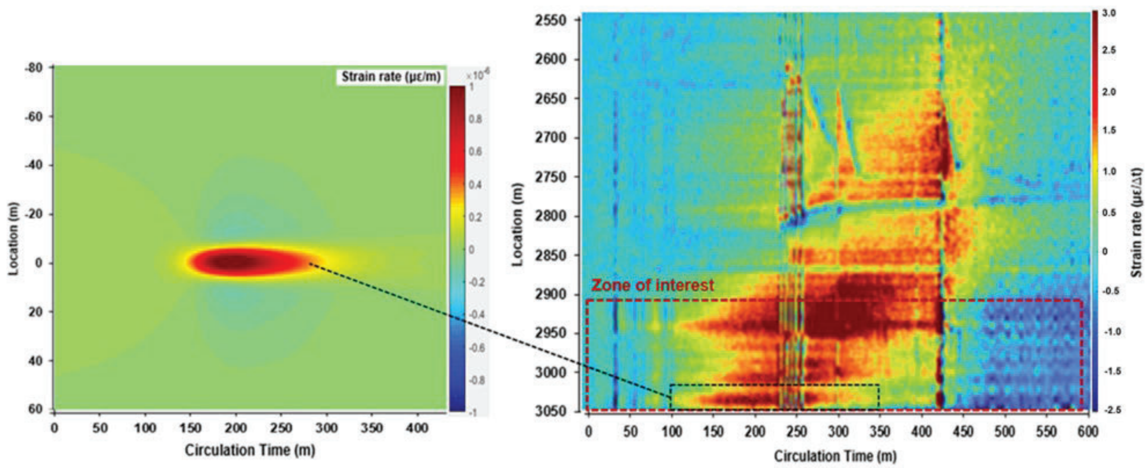

FO strain rate modeling results FORGE strain rate monitoring data

Figure 6.9: Modeling of fiber optic strain rate waterfall aligns well with field monitoring data during the circulation test. (a) Base Case fiber optic strain rate waterfall modeling results. (b) The field fiber optic monitoring data from the July 2023 circulation test.

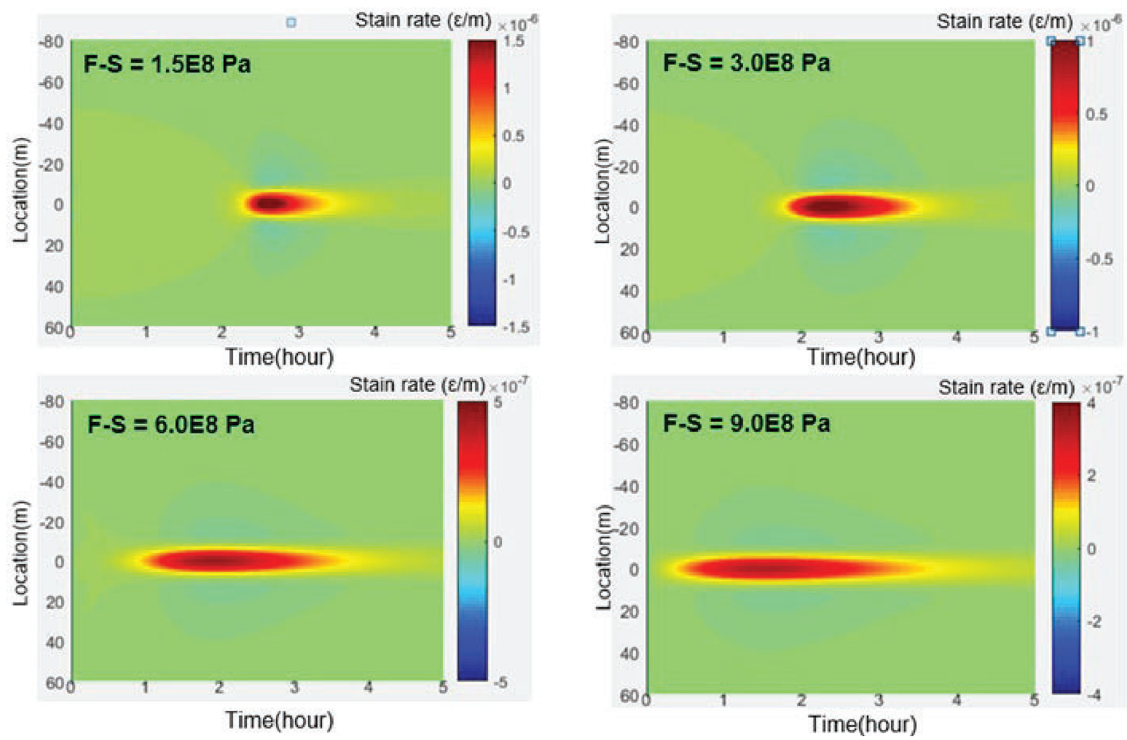

Figure 6.10: Modeling results of fiber optic strain rate waterfalls for sensitivity cases with different fracture stiffness, which leads to different overall fracture conductivity. (a) Fracture stiffness = 150 MPa; (b) Fracture stiffness = 300 MPa; (c) Fracture stiffness = 600 MPa; (d) Fracture stiffness = 900 MPa.

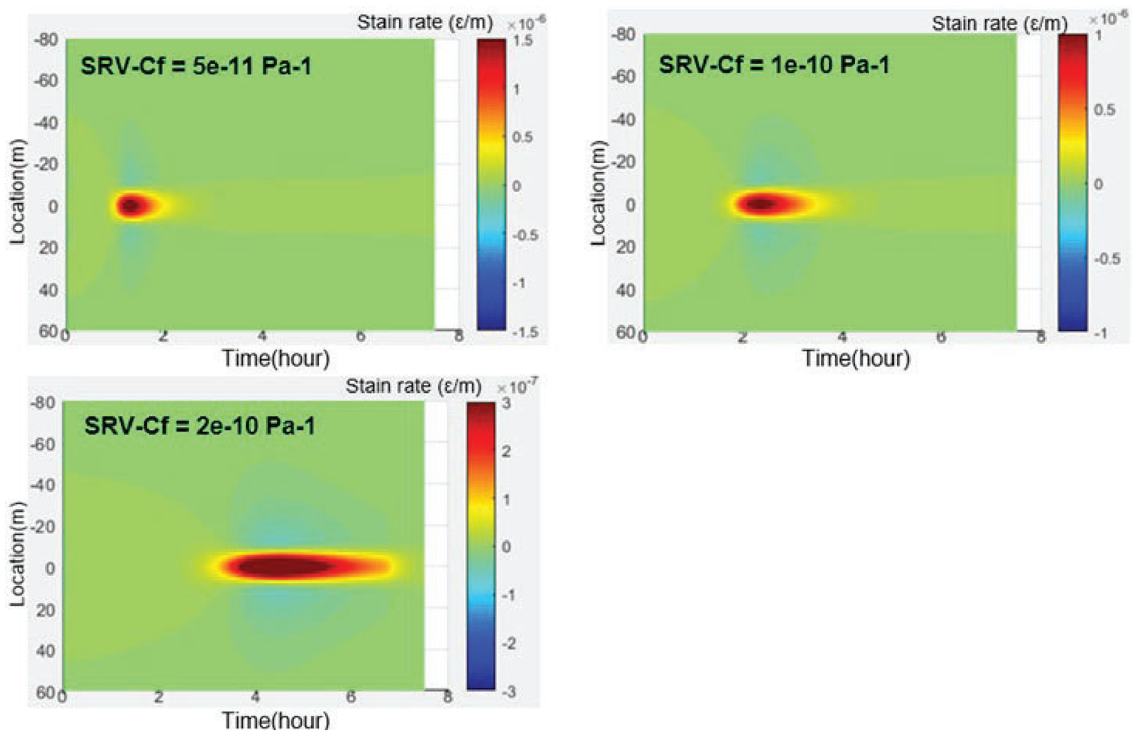

Figure 6.11: Modeling results of fiber optic strain rate waterfalls for sensitivity cases with different formation compressibility in the mechanical SRV. (a) SRV compressibility = 5e-11 Pa-1; (b) SRV compressibility = 1e-10 Pa-1; (c) SRV compressibility =2e-10 Pa-1.

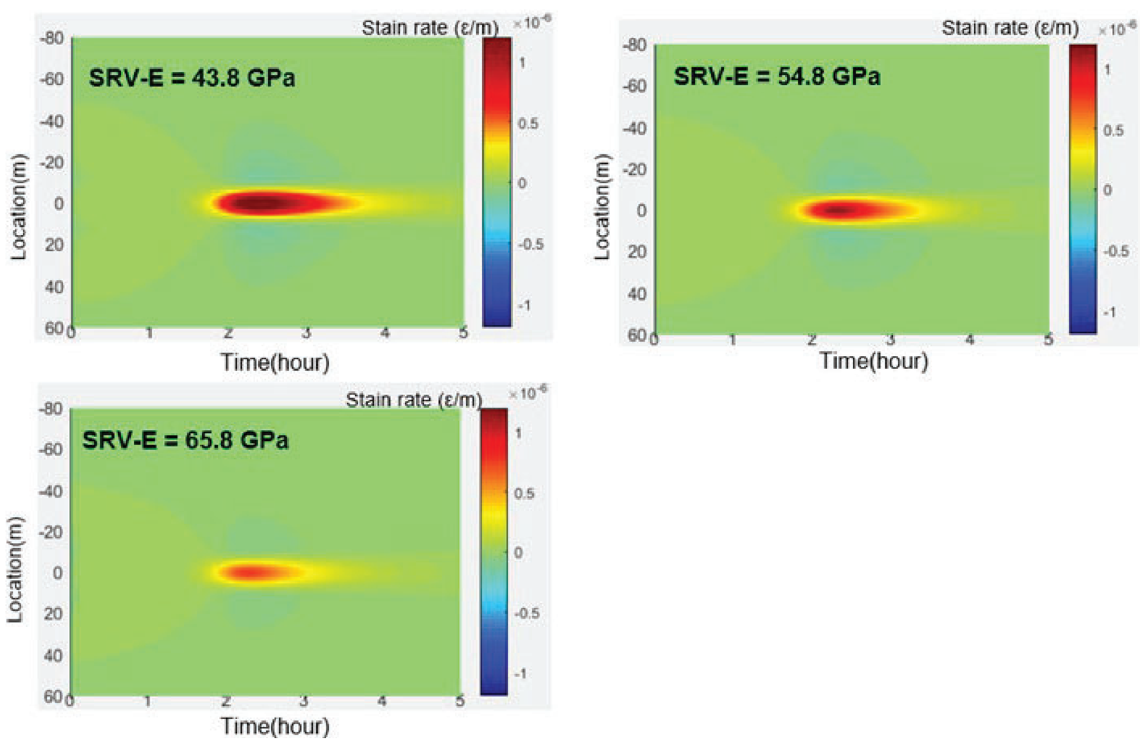

Figure 6.12: Modeling results of fiber optic strain rate waterfalls for sensitivity cases with different formation Young's modulus in the mechanical SRV. (a) SRV Young's modulus = 43.8 GPa; (b) SRV Young's modulus = 54.8 GPa; (c) SRV Young's modulus = 65.8 GPa.

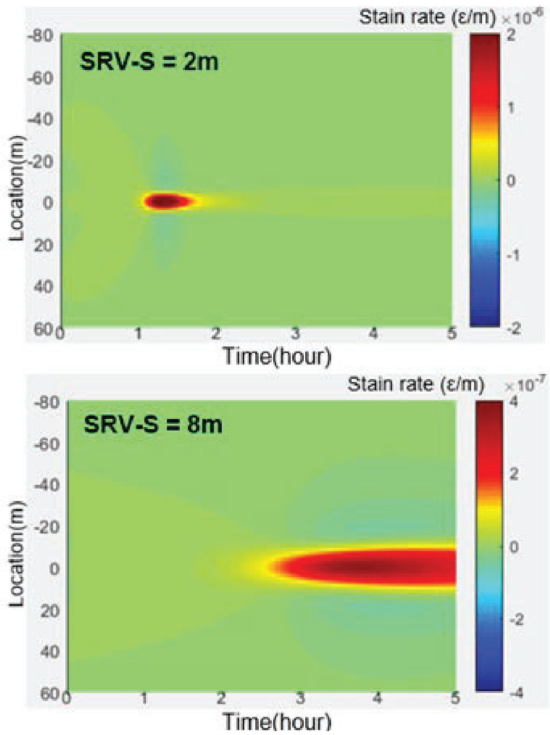

Figure 6.13: Modeling results of fiber optic strain rate waterfalls for sensitivity cases with different mechanical SRV size. (a) SRV size = 2m; (b) SRV size = 4m; (c) SRV size = 8m.

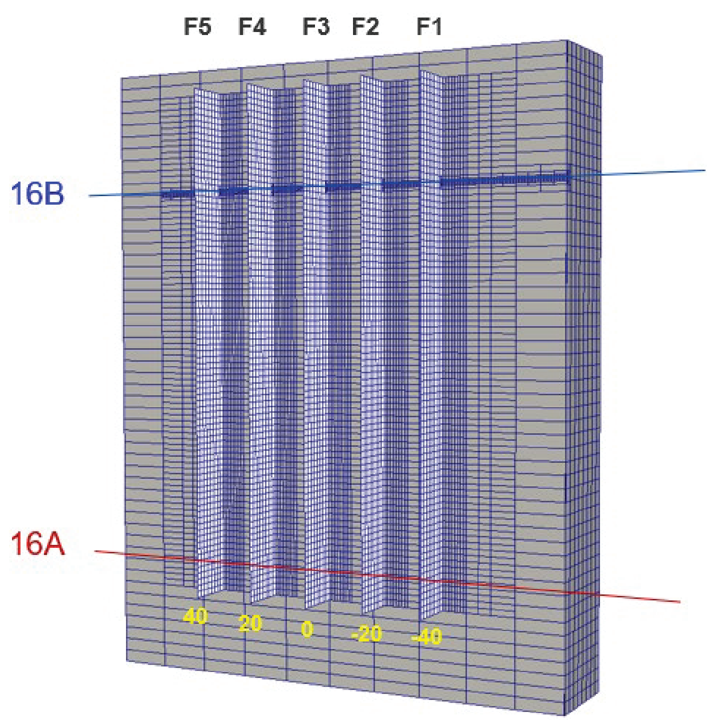

Figure 6.14: Fracture and reservoir mesh setting of the multi-fracture case. The five fractures are set up with identical fracture length but different stiffnesses and SRV properties.

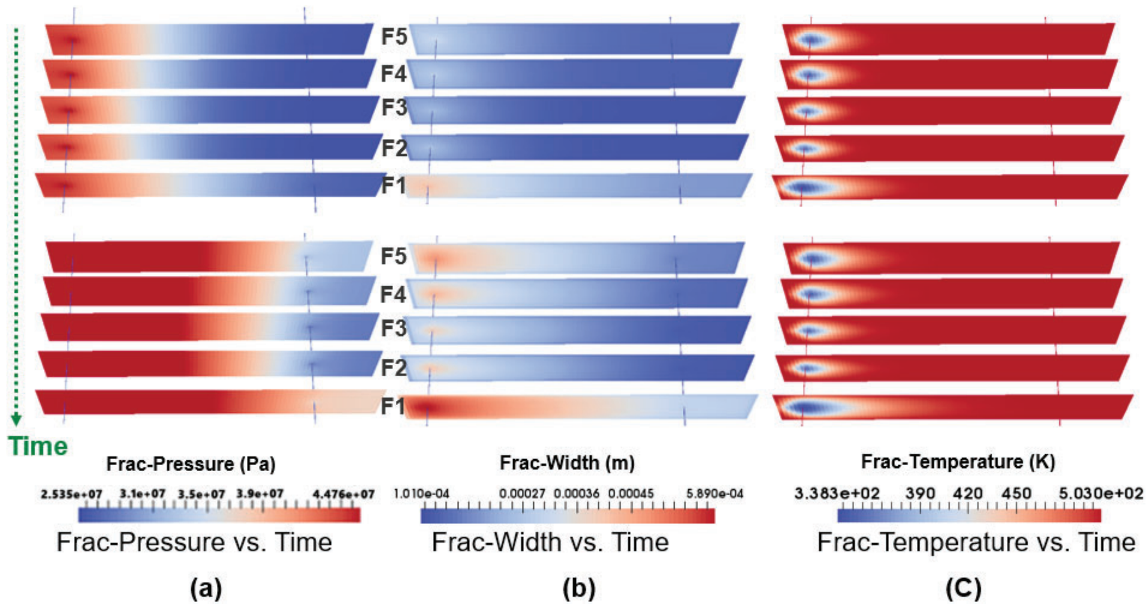

Figure 6.15: (a) Evolution of fracture pressure during the multi-fracture circulation. (b) Evolution of fracture width during the multi-fracture circulation. (c) Evolution of fracture temperature during the multi-fracture circulation.

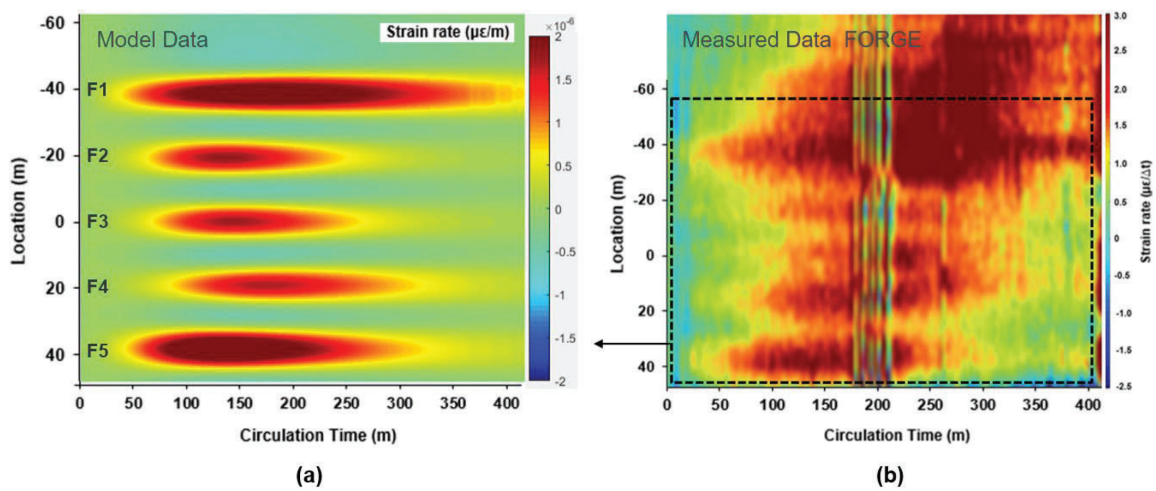

Figure 6.16: (a) Fiber optic distributed strain rate waterfall modeling results of the multi-fracture simulation case. (b) Field fiber optic monitoring waterfall within the zone of interest.

7. Monitoring Inflow Distribution in Geothermal Wells During Fluid Circulation (Circulation Test 2) Using Distributed Fiber Optic Measurements

7.1 <u>Fiber Optic Inflow Profiling via Thermal Slugging</u>

Uniform fluid inflow into a geothermal production well is a critical factor determining its effectiveness in recovering thermal energy. Insufficient or non-uniform inflow can significantly limit heat extraction, underscoring the importance of accurately identifying inflow locations and quantifying the rates at which fluids exit the injection well and enter the production well. The Rayleigh frequency shift based distributed strain sensing (DSS-RFS) and low-frequency DAS (LF-DAS) have demonstrated sensitivity to localized temperature perturbations, making them valuable tools for inflow profiling (Jin et al., 2019). Fiber-optic distributed sensing technologies can detect these perturbations via the propagation of transient thermal slugs along the wellbore during the early phases of production. When a shut-in well starts producing, the incoming fluid is at a different temperature to the previously stationary fluid, and the fiber experiences a measurable strain change. The subsequent displacement of this thermal contrast along the wellbore before reaching thermal equilibrium is referred to as thermal slugging (Mahue et al., 2022a).

Fiber-optic temperature measurements exhibit a linear correlation with borehole temperature, so the thermal slugging features observed in the diagnostic waterfall plot indicate the movement of fluid. Because these waterfall plots are presented as functions of depth and time, the velocity of the moving fluid can be inferred from the slope (i.e., gradient) of the thermal slugs. By tracking multiple thermal slugs throughout the wellbore, it is possible to construct depth-dependent velocity profiles (Figure 7.1). These profiles provide valuable insight into injection and production allocation and are particularly useful during transient shut-in and reopening cycles, where the thermal slugging velocities (also referred to as "thermal plumes") can be used to evaluate near-wellbore inflow behavior (Mahue et al., 2022b). Moreover, distributed monitoring of thermal slugging has recently been applied to assess production variations and fluid interference effects in offset wells (Mahue et al., 2022a; Lawrence et al., 2021; Lawrence et al., 2023).

7.2 Monitoring Thermal Slugging During Fluid Circulation at FORGE

The July 2023 circulation dataset revealed critical EGS characteristics, including fracture conductivity, geometry and evolving properties within the stimulated reservoir volume (SRV) (Ou et al., 2024). A more complex dataset was generated during the April 2024 circulation, reflecting a longer stimulated lateral with more hydraulic fracture intersections. Importantly, prior to the April 2024 circulation test, both the fracturing treatment and in-well circulation introduced significant thermal heterogeneity along producer well 16B. Given the high sensitivity of fiber-optic sensing to localized temperature variations, the movement of fluids with differing thermal signatures during the early stages of circulation gave rise to a pronounced thermal slugging effect (Figure 7.2). This phenomenon, caused by transient thermal contrasts moving through the wellbore, reflects fluid transport behavior influenced by prior operational history. Since fiber optic waterfall plots display data over depth and time, the velocity of wellbore fluids can be inferred from the gradient of the thermal slugging features. Consequently, tracking thermal slugs along the lateral enables the reconstruction of a depth-dependent velocity profile, offering an improved understanding of flow allocation along the production well.

7.3 Model Setup

Using the coupled reservoir-fracture-wellbore model, integrated flow and temperature simulations were conducted to investigate the driving mechanisms of thermal slugging observed in the fiber optic waterfall plot. A three-dimensional Base Case was established for modeling fluid circulation through a primary planar fracture. The computational mesh for the simulated reservoir domain, shown in Figure 7.3, features the producer well (16B) positioned 120 meters above the injector well (16A). The geothermal domain measures 128 × 64 × 200 meters, with a grid consisting of 16, 16, and 50 cells in the x, y, and z directions, respectively.

To enhance accuracy, four levels of mesh refinement were applied around the fracture faces and the production wellbore, yielding a refined mesh size of 0.5 meters. Both the injector and producer wells were modeled as one-dimensional domains, with mesh sizes of 0.5 meters that align with the surrounding refined reservoir grid blocks. This configuration ensures that the simulation effectively captures the dynamic evolution of local pressure and temperature near the fracture and wellbore, generating data with sufficient resolution to be comparable to fiber optic measurements.

Zero-gradient boundary conditions were imposed for both temperature and pressure simulations. The model assumes that the fiber optic cable attached to the casing captures all thermal disturbances within the wellbore flow. To minimize computational costs associated with the three-dimensional discretization of the casing, heat transfer between the wellbore fluid and the casing was neglected. Instead, the fine reservoir grid blocks encompassing the wellbore meshes were treated as part of the cement (Figure 7.4), and the volume of this cement cell was adjusted considering the volume of the cement ring around the borehole. Heat transfer between the wellbore and reservoir domains was computed using the heat conduction coefficient of the cement. Furthermore, heat transfer between the fracture and the wellbore was modeled by incorporating both convection and conduction to accurately represent the temperature distribution in the wellbore at the fracture intersection.

The EGS circulation simulation is designed based on reservoir parameters and in-situ conditions specific to the Utah FORGE site, as detailed in the FORGE online database. The general formation and wellbore simulation inputs for the Base Case are summarized in Table 7.1, while the thermal simulation inputs are outlined in Table 7.2. It is assumed that the casing temperature matches the wellbore fluid temperature, allowing the fiber optic cable (attached to the cemented casing) to directly capture temperature changes within the wellbore. The thermal properties of the cement are also assumed to be equivalent to those of the geothermal reservoir rock. The Base Case simulation focuses on the first three hours of the April 2024 circulation test at the FORGE site. Bottom hole pressure values for both the injector and producer wells are derived from field wellhead pressure data, as illustrated in Figure 7.5. The initial wellbore temperature distribution is established through either modeling in-well circulation or fracturing injection at the production well prior to EGS circulation.

According to Jin et al., (2019), the thermal slugging observed in the fiber optic waterfall plot arises from the non-uniform temperature distribution within the stationary fluid in the wellbore before EGS circulation commences. This study proposes two potential causes for the non-uniform wellbore temperature in the producer at the onset of EGS circulation: (1) hydraulic fracturing treatment of the production well and (2) in-well fluid circulation within the producer, implemented to cool the wellbore for the operation of other downhole diagnostic tools. After stimulating the injector, hydraulic fractures propagate to the production well. The producer is then perforated and stimulated at these fracture intersection points to establish connections with far-field fractures, thereby completing the closed-loop fluid circulation system between the injector and producer. In the Base Case, the thermo-hydro simulation of the producer treatment lasts 1.5 hours under a constant bottom hole pressure of 68.94 MPa, followed by a shut-in period of 6.5 days.

7.4 Results and Discussion

In this section, the thermo-hydro modeling results for the EGS circulation in the Base Case are presented. These results highlight the temperature and pressure distributions within the wellbore-fracture-reservoir system during fluid injection, formation warm-back, and fluid circulation. The findings explain the reasons behind the non-uniform temperature distribution along the wellbore at the start of fluid circulation. This arises from in-well fluid circulation prior to EGS circulation. This part of the data (prior to EGS fluid circulation) is useful to estimate how thermal transients occur within a wellbore during in-well fluid circulation but is beyond the scope of this paper. We focus on the temperature transients during fluid circulation between the injection and production wells.

7.4.1 Base case results

The reservoir temperature distribution at the conclusion of the 1.5-hour fracture injection and at the initiation of fluid circulation (after the 6.5-day shut-in) are illustrated in Figure 7.6. During the injection phase, with bottom hole pressures reaching approximately 10,000 psi, a significant volume of low-temperature fluid infiltrates the hot dry rock formation through the perforations along the wellbore. This leads to a rapid decrease in wellbore temperature to 303 K, resulting in a temperature difference of 191 K compared to the in-situ temperature of the Utah FORGE formation, as indicated by downhole temperature data. In the near-wellbore and near-fracture regions, the formation temperature decreases due to the combined effects of heat convection and conduction. The wellbore fluid/casing temperature remains constant at 303 K, while the reservoir temperature declines due to heat conduction between the casing and cement during the fracturing injection.

Convection primarily governs the temperature reduction of fluid within the fracture. Since the main objective of the production well stimulation is not to propagate hydraulic fractures but to establish connections at key points of fractures from the injection well stimulation, fractures are created prior to the injection treatment of the production well. Consequently, a considerable volume of cold fluid enters the fracture, lowering its temperature along the fracture's half-length as the injected fluid progresses. The injected fluid subsequently enters the adjacent reservoir through fracture leak-off, further decreasing reservoir temperature through both heat convection and conduction as it migrates within the fracture. As shown in Figure 7.6a, the production well stimulation results in a non-uniform temperature distribution in the near-wellbore region, which significantly influences the wellbore temperature during the post-injection warm-back. The effect of temperature reduction extends deeper into the formation due to ongoing heat conduction during the post-injection warm-back period (Figure 7.6b), balancing the temperature increase in the wellbore as the injection ceases.

Figure 7.7 and Figure 7.8 illustrate the fracture and wellbore temperature distributions during the early transient stages of EGS circulation. Following the post-injection warm-back, the wellbore temperature begins to recover. However, due to the non-uniform temperature field along the producer, heat conduction rates vary across different sections of the wellbore, driven by temperature differentials between the wellbore fluid and cement near fractures. During EGS circulation, fluid is injected into the injector well, flows through the fractures, and enters the producer, where the fluid exhibits a non-uniform temperature distribution (Figure 7.7a). As circulation progresses, increased pressure in the wellbore-fracture-reservoir system pushes the low-temperature fluid toward the bottom hole (Figure 7.7b), reducing the temperature in sections where the fluid was previously warmer. Nonetheless, the overall wellbore temperature rises during EGS circulation as higher-temperature fracture/reservoir fluid is introduced into the system (Figure 7.8).

The continuous variation in wellbore fluid temperature before reaching thermal equilibrium generates thermal slugging during the evolution of wellbore temperature. Fiber optic measurements are linearly correlated with local temperature changes, based on a thermal-mechanical transfer coefficient (Jin et al., 2019). Consequently, fiber optic strain rate sensing data is represented by plotting the rate of wellbore fluid temperature change against space and time. The temperature change rate waterfall plot for the Base Case is presented in Figure 7.9a. By applying the correct transfer coefficient and assuming zero temperature difference between the wellbore casing and the fluid, the actual fiber optic sensing waterfall can be obtained. The simulation results closely align with the thermal slugging patterns observed in the Utah FORGE fiber optic waterfall plot (Figure 7.2), where thermal slugging is characterized as a distinct cool ribbon pattern, depicted in blue, originating from the location of the producing fracture.

The absolute wellbore temperature waterfall is displayed in Figure 7.9b. The thermal slugging features in the waterfall data diminish in magnitude as circulation time increases, indicating a tapering effect of thermal slugs before the system reaches thermal equilibrium. The green dashed arrows in Figure 7.9 highlight the movement of the low-temperature slug (the blue ribbon in Figure 7.9b), corresponding to the movement of the zero-temperature rate line (the white line in the middle of the yellow and blue ribbons in Figure 7.9a) in the fiber optic waterfall data plot. The strong alignment between the fiber optic temperature rate waterfall and the absolute wellbore temperature values suggests that the observed thermal slugging signals in the fiber optic measurements are primarily driven by the non-uniform temperature distribution of fluid within the wellbore as it flows through the producer during EGS circulation.

7.4.2 Fluid velocity estimation

The thermal slugging signal in the fiber optic waterfall plot exhibits a ribbon-like feature, with a gradient that varies with circulation time. Since the fiber optic waterfall is plotted against space and time, tracking the gradient of the thermal slugging feature can assist in estimating the velocity of fluid flowing within the producer. Figure 7.10a shows the wellbore fluid flowing velocity relative to different locations along the wellbore for the Base Case. The section of the wellbore closest to the toe exhibits no flowing velocity, as the Base Case represents a single fracture simulation without continuous production from fractures behind it. Within the flowing section, the wellbore fluid velocity remains constant, and it increases with circulation time due to rising injection pressure (Figure 7.5).

To further analyze the original fiber optic modeling results, the rate of temperature change is processed to display only its sign within the fiber optic waterfall, allowing for the illustration of the zero-temperature change curve. This curve aids in estimating wellbore fluid velocity based on the temperature rate waterfall (Figure 7.10b). Four distinct time nodes—circulation times of 23 minutes, 57 minutes, 101 minutes, and 152 minutes—are selected for estimating wellbore fluid velocity, which is then compared to the actual velocity calculated from the model.

As indicated in Figure 7.11, the wellbore fluid velocities estimated from the processed fiber optic waterfall plot correlate well with the actual flowing velocities in the wellbore simulation, with the exception of the early times. In the Base Case the wellbore velocity is linearly correlated with the production rate from the main fracture. The gradient of the thermal slugging is too sharp during these initial periods, resulting in insufficient data resolution for accurately determining the derivative of the zero-temperature change curve. Nevertheless, the thermal slugging observed in the fiber optic waterfall serves as a reliable estimator of fluid velocity within the wellbore.

Furthermore, the fluid velocity distribution along the wellbore can be utilized to calculate production rates from different fractures by subtracting the velocities between various wellbore sections separated by producing fractures. This analysis enhances the understanding of fluid dynamics within the enhanced geothermal system and aids in optimizing production strategies.

7.4.3 Multi-fracture simulation considering in-well circulation

The thermal slugging features are influenced significantly when the simulation incorporates multiple fractures within the enhanced geothermal system (EGS). A multi-fracture case has been constructed to elucidate the thermal slugging signals observed in the Utah FORGE fiber optic monitoring waterfall plot during the April 2024 circulation test (Figure 7.12). The fracture permeability and width settings for the four fractures involved are detailed in Table 7.3.

Following the field operations at the Utah FORGE test site, in-well fluid circulation was implemented prior to the EGS circulation test. The target geothermal formation at this site has an average temperature of 494 K, which exceeds the operational limits (449 K) of many downhole monitoring tools, such as production logging tools used for other diagnostic purposes in the FORGE project. To mitigate these temperatures, in-well circulation was employed using a drill-mud cooler.

During the in-well circulation, the wellbore temperature decreased to 372 K and later resumed to approximately 429 K at the onset of fluid circulation, as indicated by downhole pressure-temperature gauge data from producer 16B. Similar to the fracturing treatment of the production well, in-well circulation results in a non-uniform wellbore temperature at the start of EGS circulation. Fluid from the in-well circulation continues to enter the fractures, affecting the temperature recovery rate at the cluster locations during the warm-up period. The multi-fracture case simulates a 2-day in-well circulation followed by a 1-day warm-up. The bottom hole pressure of the producer during this phase is calculated to be 0.2 MPa higher than the hydrostatic pressure, based on a frictional pressure loss corresponding to an in-well circulation rate of 485 gpm, selected from field data.

Modeling output for the fiber optic monitoring data is illustrated in Figure 7.13a. Thermal slugging signals appear in the modeling temperature change rate waterfall plot at the four cluster locations, resulting from the movement of wellbore fluid with a non-uniform temperature profile around these clusters. The absolute temperature of the production well is presented against space and time in Figure 7.13b. Compared to the Base Case, wellbore warming is notably more pronounced in the multi-fracture case. Despite this, a significant temperature difference (65 K) persists between the average wellbore temperature and the formation temperature, leading to larger warming slugs in the fiber optic waterfall while diminishing the size and magnitude of the cooling slugs.

Thermal slugging signals originating from individual fracture clusters exhibit distinct temperature gradients, which can be attributed to spatial variations in fluid flow velocity along different sections of the production well. Figure 7.14a presents a space-time visualization of the wellbore fluid velocity profile, illustrating the evolution of flow rates along the lateral section of the producer. At each location, the flow rate reflects the cumulative contribution from all upstream fracture inflows. The processed temperature change rate waterfall plot for the multi-fracture simulation is presented in Figure 7.14b.

The gradients of the zero-temperature-change boundary curves at a circulation time of 45 minutes were analyzed to evaluate the relative productivity of individual fractures, as illustrated in Figures 7.15 and 7.16. The production rate of each fracture is estimated by calculating the difference in wellbore rates on either side of the fracture. Notably, wellbore velocity profiles inferred from the thermal slugging gradients exhibit strong agreement with the actual velocity distributions obtained from simulation, with the exception of regions characterized by low fluid velocities, where steep temperature gradients limit the accuracy of interpolation. The fracture production rates derived from the fiber-optic-based waterfall plots also correlate well with those obtained from the fully coupled numerical model. These findings suggest that thermal slugging signals captured in distributed temperature data provide a viable diagnostic for assessing the relative productivity of hydraulically connected fractures within enhanced geothermal circulation systems.

7.4.4 Insights into Utah FORGE fiber optic monitoring data

As shown in Figure 7.17a, the four black solid lines denote the locations of perforation cluster endpoints for each stimulation stage along the production well (16B), based on fiber-optic monitoring data acquired during the Utah FORGE April 2024 circulation test. The spatial origins of the thermal slugging signals closely align with these stimulated fracture stages, supporting simulation results that indicate the utility of thermal slugging signals in fiber optic monitoring for assessing hydraulic connections at the producer during circulation.

The purple solid line at the top of Figure 7.17a displays the measured production rates from the producer during the April 2024 circulation. The fiber optic waterfall plot is segmented by the black solid line marked "T1," distinguishing between production and non-production periods during the EGS circulation. Notably, distinct normal thermal slugging signals are evident in the waterfall plot after "T1," corresponding with fluid production from the producer and demonstrating increasing gradients (green arrows in Figure 7.17a highlight the gradients of the thermal slugging signals at "T2"). Estimates of fluid velocity derived from the thermal slugging signals indicate that Stage 4 and Stage 1 in the injection well 16A exhibits higher production rates compared to Stages 2 and 3, particularly Stage 4.

Prior to the time denoted as "T2," reverse thermal slugging signals are observed in the fiber-optic data. These signals are hypothesized to result from inter-fracture crossflow occurring through the producer well during periods when well 16B was not actively producing. It is likely that the injected fluid migrated from higher-conductivity fractures toward lower-conductivity fractures inside the wellbore. This behavior is attributed to elevated pressures within the more conductive fractures at the onset of circulation, which drive crossflow in the absence of active production.

To further examine this phenomenon, the multi-fracture simulation case was modified to account for inter-stage crossflow during the non-production period, incorporating updated fracture properties as detailed in Table 7.4. Specifically, the primary fracture width for each perforated stage was adjusted based on the number of perforation clusters treated in each stage of the 16B stimulation. The revised simulation assumes that the producer well remains shut-in for the initial 60 minutes, replicating the non-production interval inferred from the FORGE fiber-optic data, after which standard injection–production circulation is resumed.

During the non-production period, distinct reverse thermal slugging signals were detected at the fracture locations, suggesting crossflow from Stage 4 to Stages 2 and 3 during the shut-in period. Furthermore, wellbore section velocities and stage-specific production rates, as estimated from both the field-measured fiber-optic data and the simulated fiber-optic waterfall plot, are presented in Figures 7.18 and 7.19. A strong correlation is observed between the estimations derived from field measurements and those obtained from simulation, confirming the validity of the thermal diagnostic approach. Stage 4 is consistently identified as the dominant flow conduit during the April 2024 EGS circulation test, owing to its connection with a greater number of proppant-enhanced fractures. These modeling results further reinforce that the fractures associated with Stage 4 in well 16B exhibit significantly higher conductivity and productivity compared to those in Stages 2 and 3. The interpolated insights extend beyond pure wellbore velocity estimates derived from gradients of thermal slugging signals, providing a deeper understanding of the development of multi-stage fracture network within the EGS system.

Parameters	Value
Rock thermal conductivity ($W\ m^{-1} K^{-1}$)	2
Cement thermal conductivity ($W\ m^{-1} K^{-1}$)	2
Fluid thermal conductivity ($W\ m^{-1} K^{-1}$)	1
Rock heat capacity ($J\ kg^{-1} K^{-1}$)	915
Cement heat capacity ($J\ kg^{-1} K^{-1}$)	915
Fluid heat capacity ($J\ kg^{-1} K^{-1}$)	4184
Propped fracture permeability (D)	5
Formation temperature (K)	494
Circulation injection temperature (K)	324
In-well circulation temperature (K)	372

Table 7.1: Formation and wellbore inputs for the Base Case.

Parameters	Value
In-situ stress (MPa)	43.99, 47.89, 64.83
Young's modulus (GPa)	54.8
Poisson's ratio	0.26
Biot's coefficient	0.85
Reservoir permeability (μD)	5
Reservoir pore pressure (MPa)	2.355
Fluid compressibility ($10^{-10} Pa^{-1}$)	5
Fluid viscosity (cp)	1
Fluid density (kg/m^3)	1000
Rock density (kg/m^3)	2700
Reservoir porosity	0.01
Rock tensional strength (MPa)	1
Rock thermal conductivity ($W\ m^{-1} K^{-1}$)	2
Fluid thermal conductivity ($W\ m^{-1} K^{-1}$)	1
Rock heat capacity ($J\ kg^{-1} K^{-1}$)	890
Fluid heat capacity ($J\ kg^{-1} K^{-1}$)	4184
Thermo-elasticity coefficient ($10^{-6} K^{-1}$)	3.3
Formation temperature (K)	494
Fracture injection temperature (K)	324

Table 7.2: Thermal simulation inputs for the Base Case.

Fracture number	Fracture Width (mm)	Fracture permeability (D)
F1	4	10
F2	4	1
F3	4	4
F4	4	6

Table 7.3: Fracture conductivity setting of the multi-fracture case.

Stage number	Fracture Width (mm)	Fracture permeability (D)
S1	12	14
S2	7	5.5
S3	8	7
S4	17.5	22.5

Table 7.4: Fracture conductivity setting of the modified multi-fracture case.

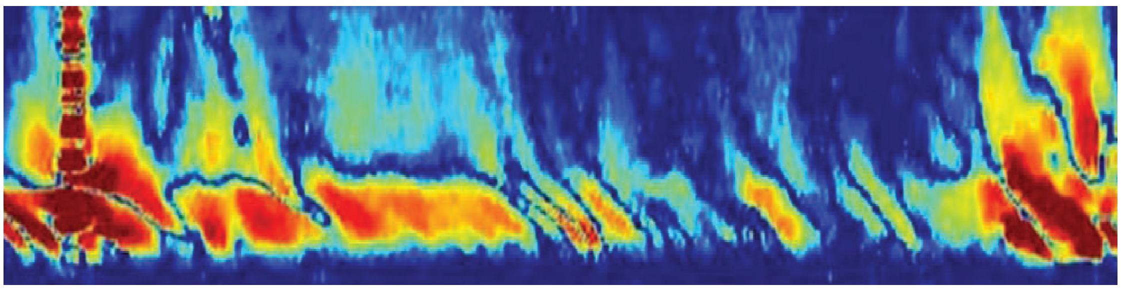

Figure 7.1: DAS slow strain waterfall for inflow profiling. X axis is the locations along the horizontal well, and Y axis is the monitoring time (Mahue et al., 2022a).

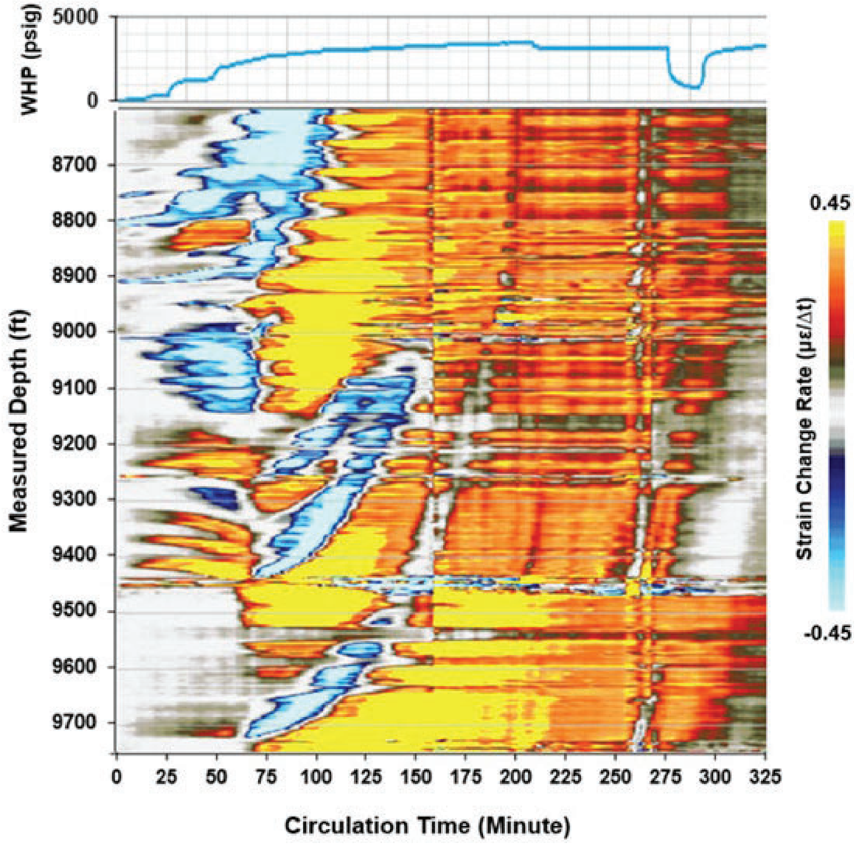

Figure 7.2: Fiber optic strain rate waterfall plot obtained from the Utah FORGE April 2024 fluid circulation test. (Ou et al., 2025b).

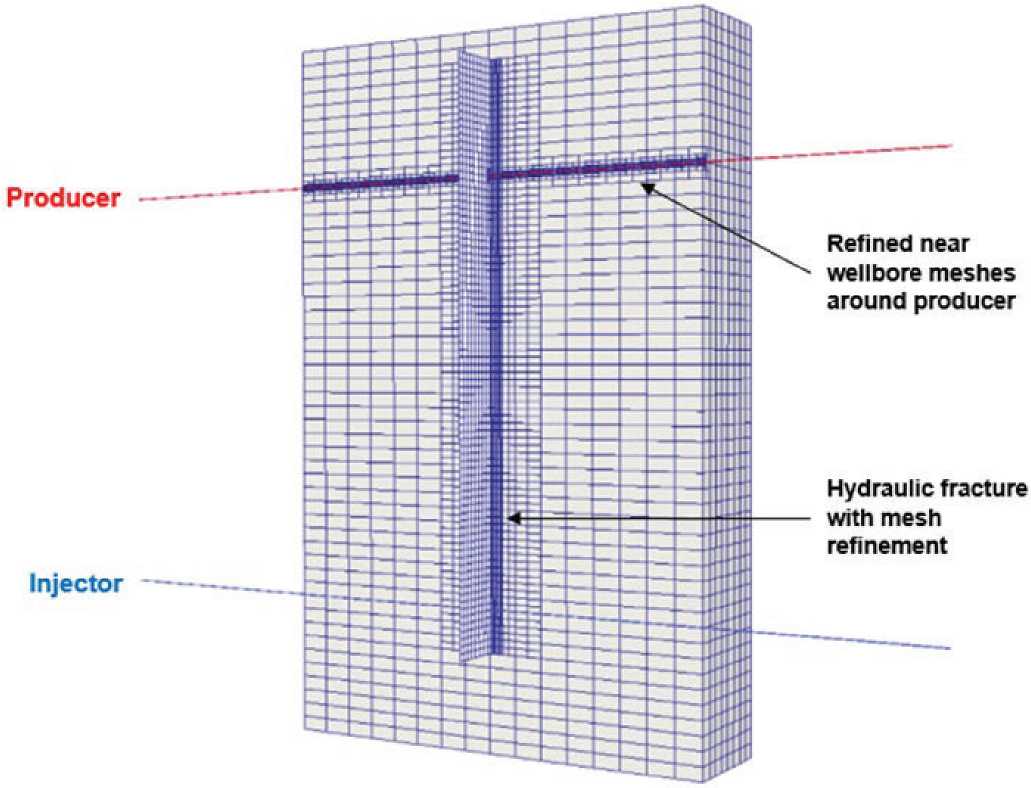

Figure 7.3: Computational mesh of the Base Case with one main planar fracture. The numerical geothermal domain is 128m x 64m x 200m. Producer 16B is placed 120 meters above the injector 16A. Mesh refinement is applied around the main planar fracture and the producer.

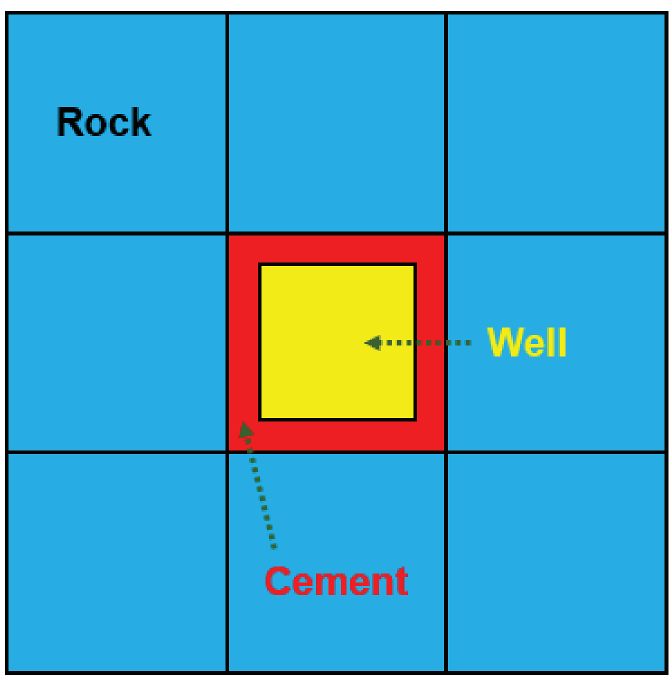

Figure 7.4: Computational mesh setting of the near wellbore region. The blue region depicts the reservoir rock cells. The red region expressed the cement cell intersected by the wellbore mesh.

The volume of this cement cell was adjusted considering the volume of the cement ring around the borehole. The yellow region is the cell of the numerical wellbore domain.

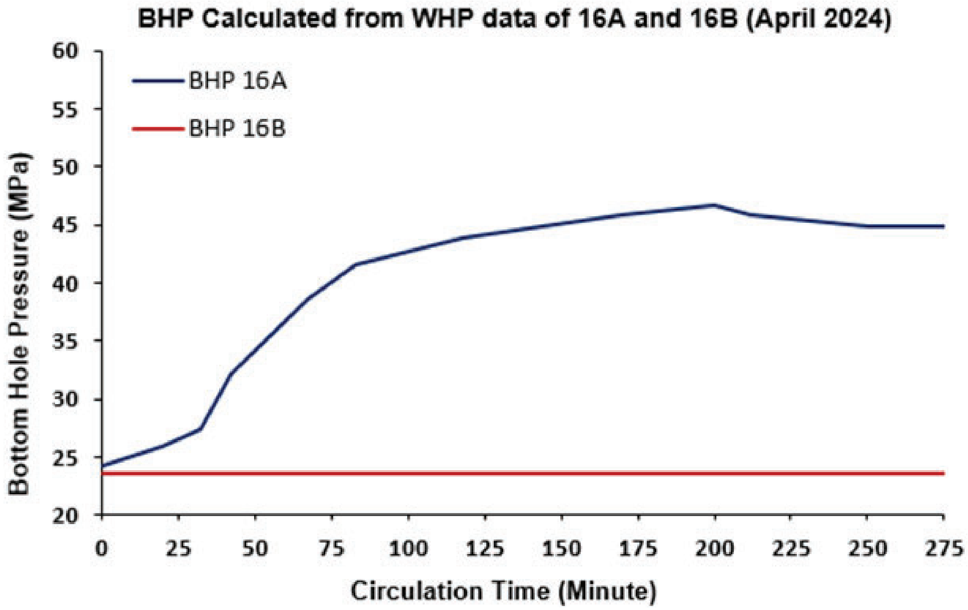

Figure 7.5: Bottom hole pressure values of the injector and the producer for the April 2024 EGS circulation simulation calculated based on field wellhead pressure data from the FORGE site.

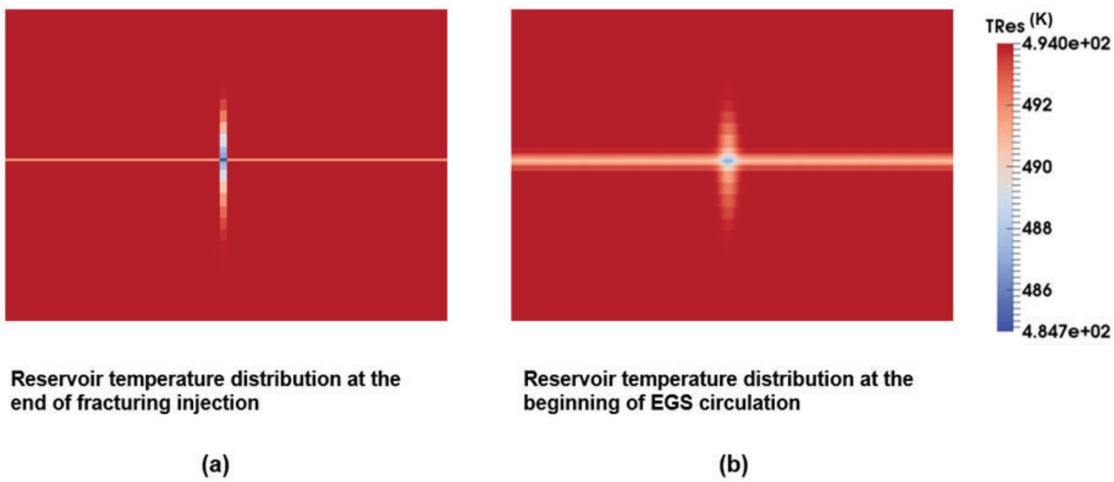

Figure 7.6: Reservoir temperature distribution of the Base Case simulation. (a) At the end of 1.5-hour fracturing injection. (b) At the beginning of the EGS fluid circulation after 6.5-day of post-frac shut-in.

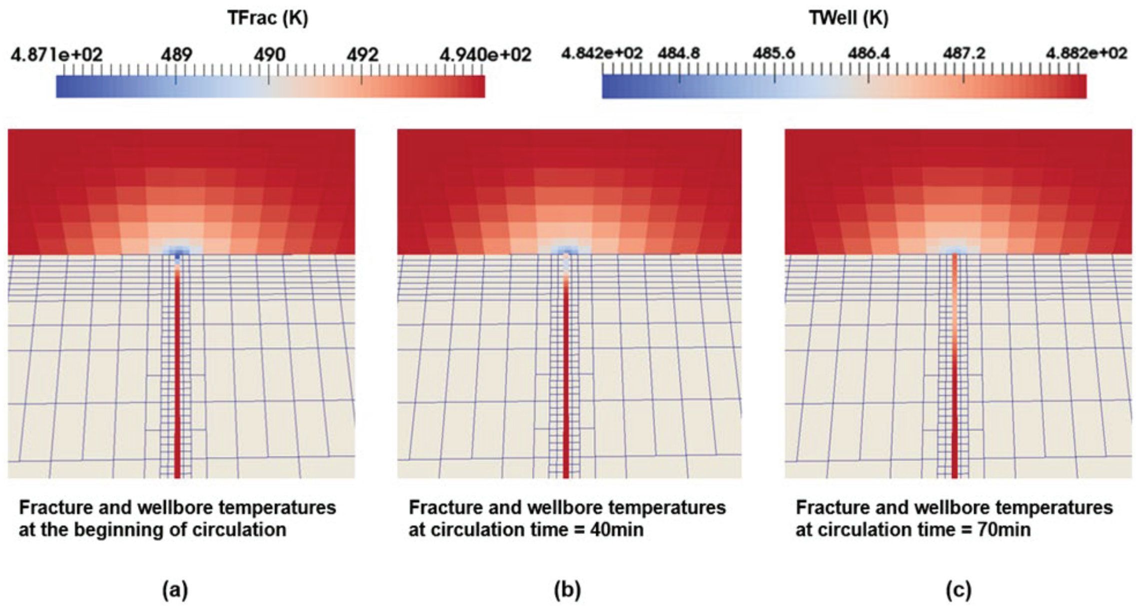

Figure 7.7: Fracture and wellbore fluid temperature distribution of the Base Case simulation during early transient EGS circulation. (a) At the beginning of the EGS fluid circulation. (b) At circulation time = 40min. (c) at circulation time = 70min.

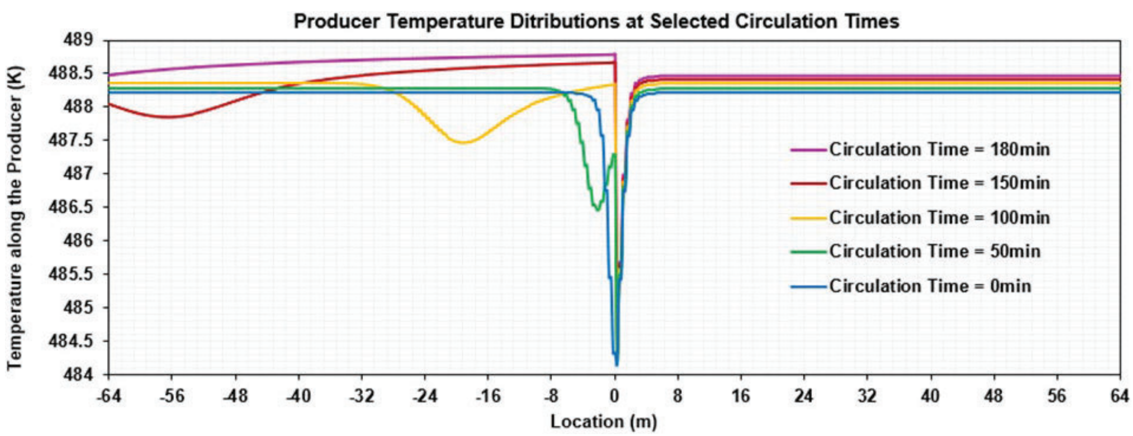

Figure 7.8: Wellbore temperature evolution during EGS fluid circulation along the producer.

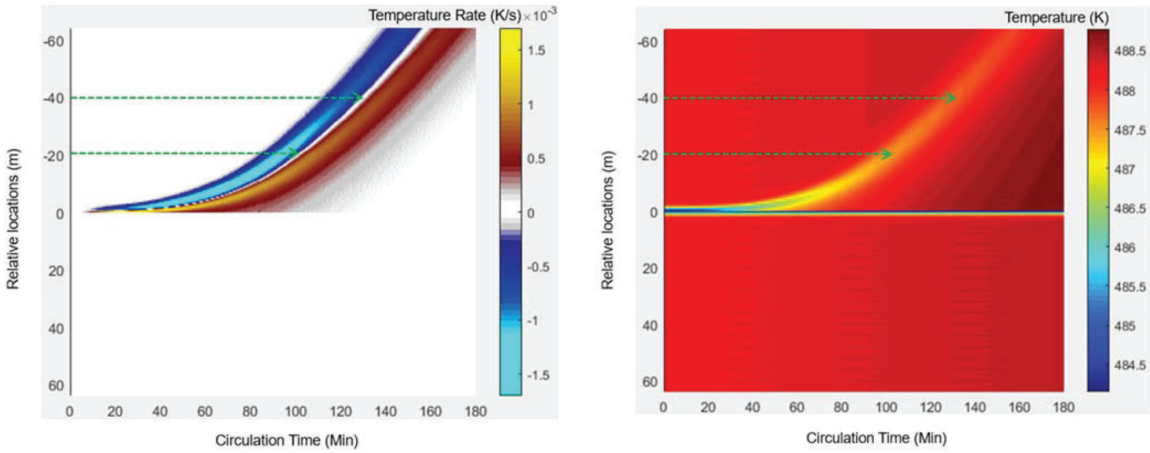

(a) (b)

Figure 7.9: Thermal simulation waterfall plots of the Base Case. (a) Temperature change rate waterfall plot representing the fiber optic strain rate monitoring plot in this work. (b) Production wellbore temperature waterfall plot during EGS circulation of the Base Case.

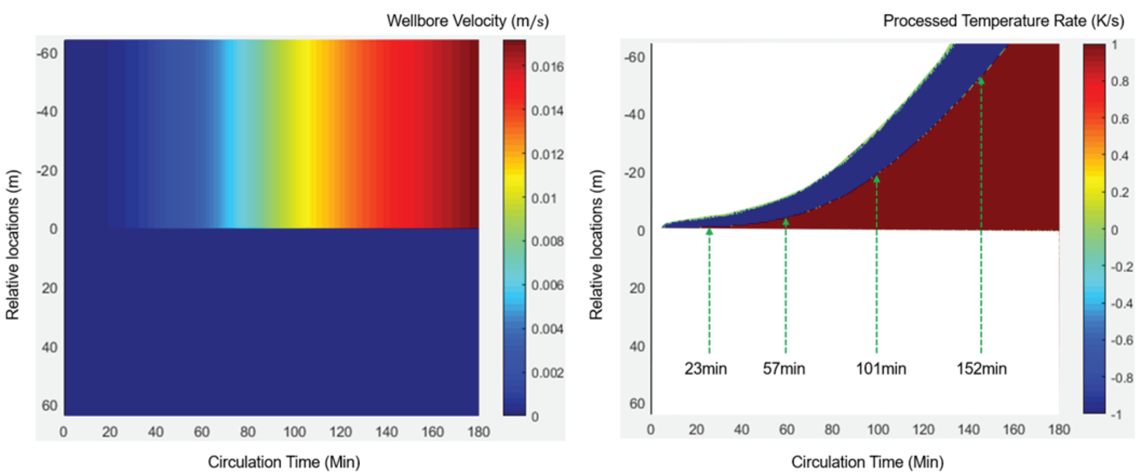

(a) (b)

Figure 7.10: (a) Wellbore fluid velocity during circulation modeling of the base case. (b) Processed temperature change rate waterfall plot for the Base Case. The boundary between the red and blue-ribbon region is the zero-temperature change curve that is processed to calculate the gradient of the wellbore thermal fronts.

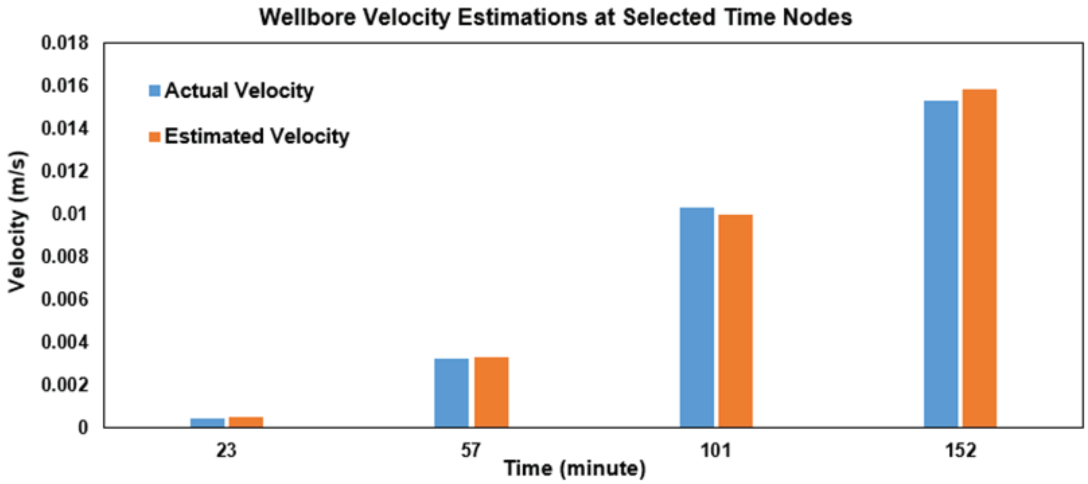

Figure 7.11: Wellbore velocity/production from fracture estimations at selected time nodes of the Base Case. In the Base Case the wellbore velocity is linearly correlated with the production rate from the main fracture. The velocities estimated from the thermal slugging signals show a good agreement with the actual wellbore velocities estimated from the model.

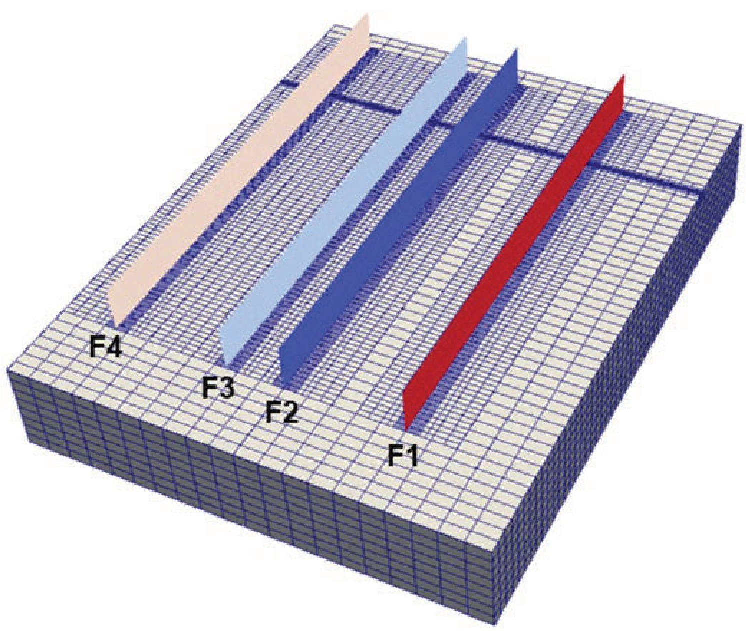

Figure 7.12: Computation mesh of the multi-fracture simulation with 4 connected fractures.

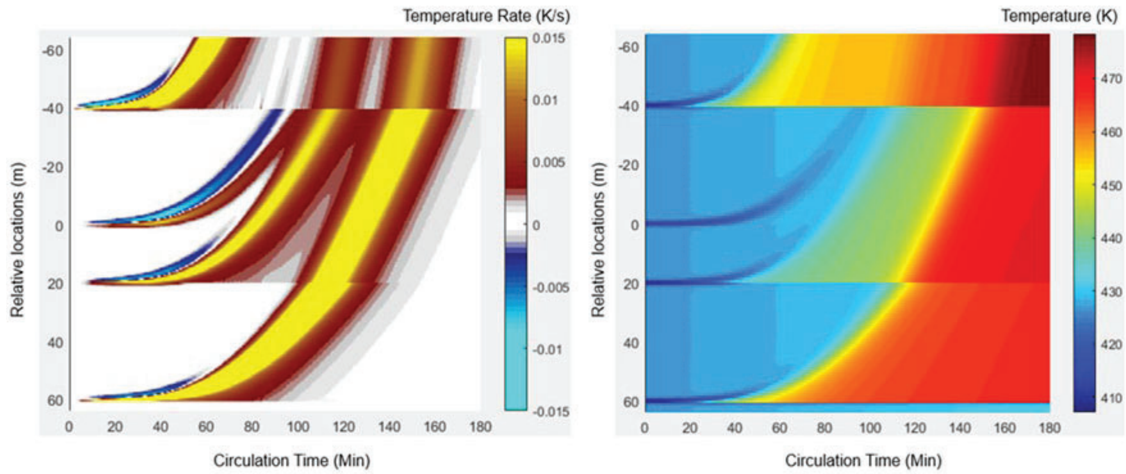

(a) (b)

Figure 7.13: (a) Fiber optic monitoring waterfall plot of the multi-fracture case. (b) Absolute temperature evolution along the producer during circulation simulation of the multi-fracture case.

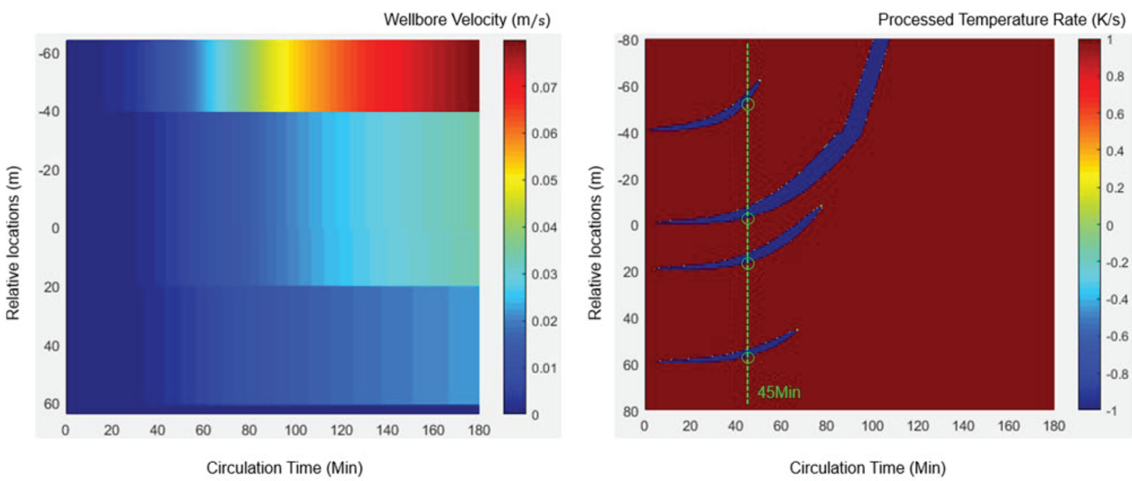

(a) (b)

Figure 7.14: (a) Calculated wellbore velocity evolution along the producer during circulation simulation of the multi-fracture case. (b) Processed temperature change rate waterfall plot for the multi-fracture case. Green circles are locations selected for fracture production rate estimation at 45 minutes circulation.

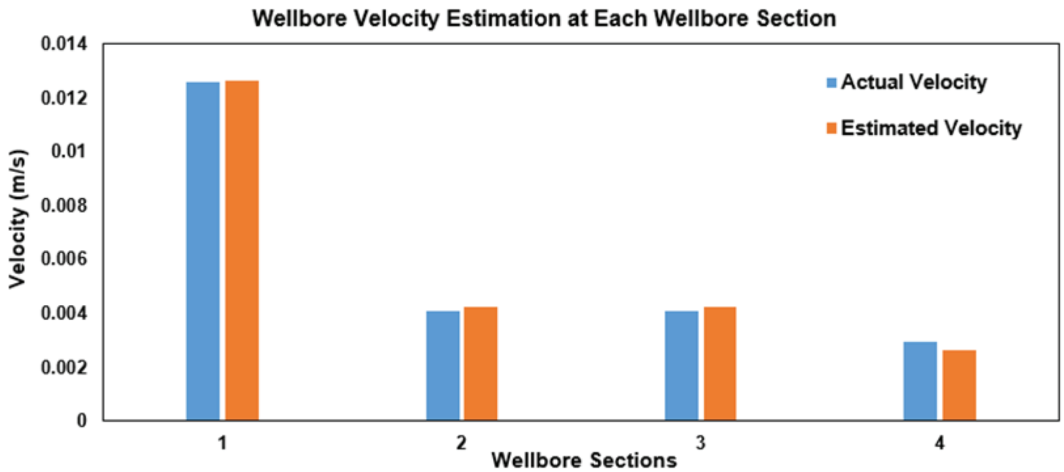

Figure 7.15: Wellbore fluid velocity estimates within different sections of the producer of the multi-fracture case at circulation time of 45 minutes. The wellbore fluid velocities estimated from the thermal slugging signals in the fiber optic waterfall closely align with the actual fluid velocities calculated from the numerical model except for low velocity sections where the gradients are too sharp for data interpretation.

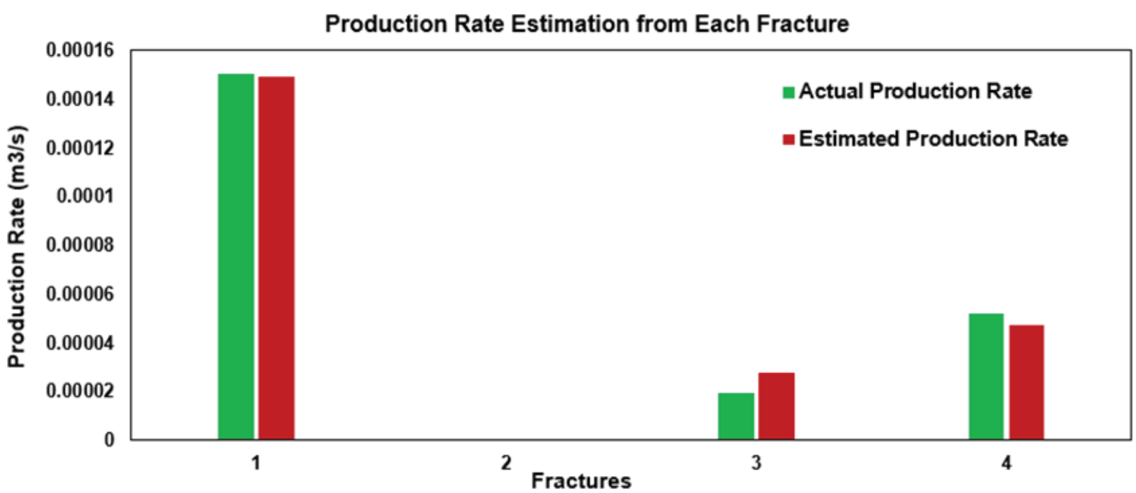

Figure 7.16: Production rates from each fracture estimated by the fiber optic data in the multi-fracture case at circulation time of 45 minutes. Production rates estimated from the thermal slugging signals show good agreement with the actual production rates calculated from the numerical model. Higher error is seen in less productive fractures where changes in gradient are too small in the corresponding thermal slugging signals.

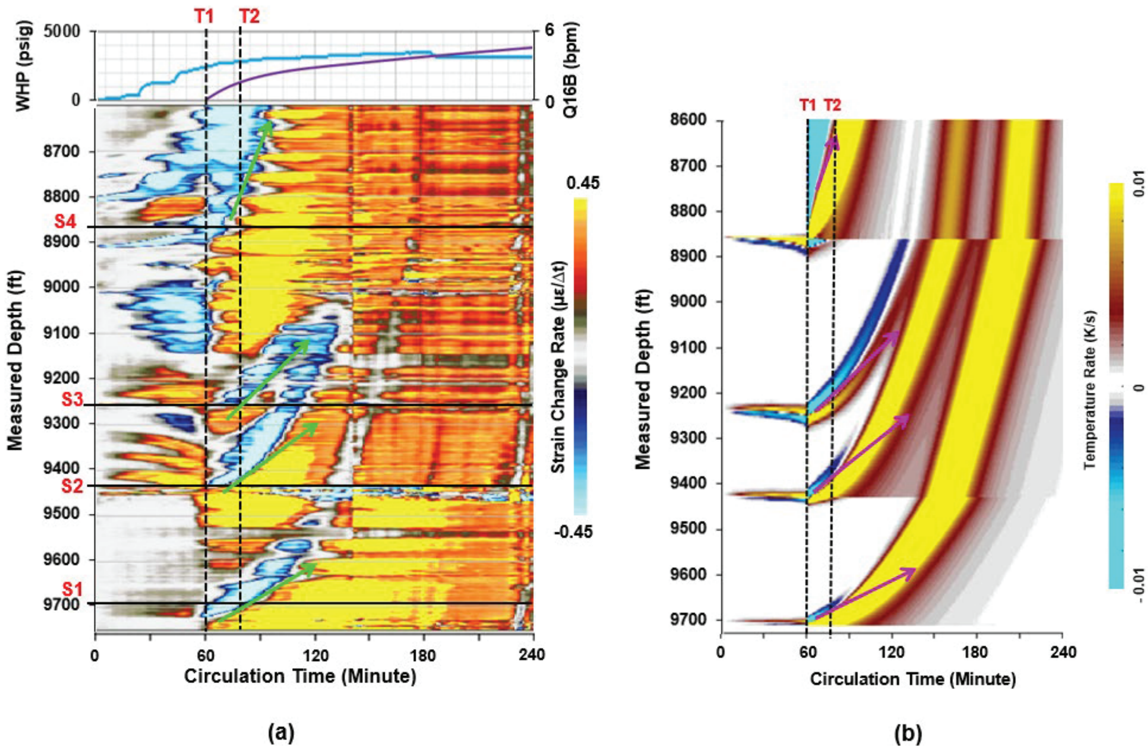

Figure 7.17: (a) Fiber optic monitoring waterfall data plot from the FORGE April 2024 circulation test. Green arrows deliver the estimated average wellbore fluid velocities from different perforated stages. (b) Simulated fiber optic waterfall plot considering the crossflow among fractures. Purple arrows deliver the estimated average wellbore fluid velocities from different perforated stages in the simulation.

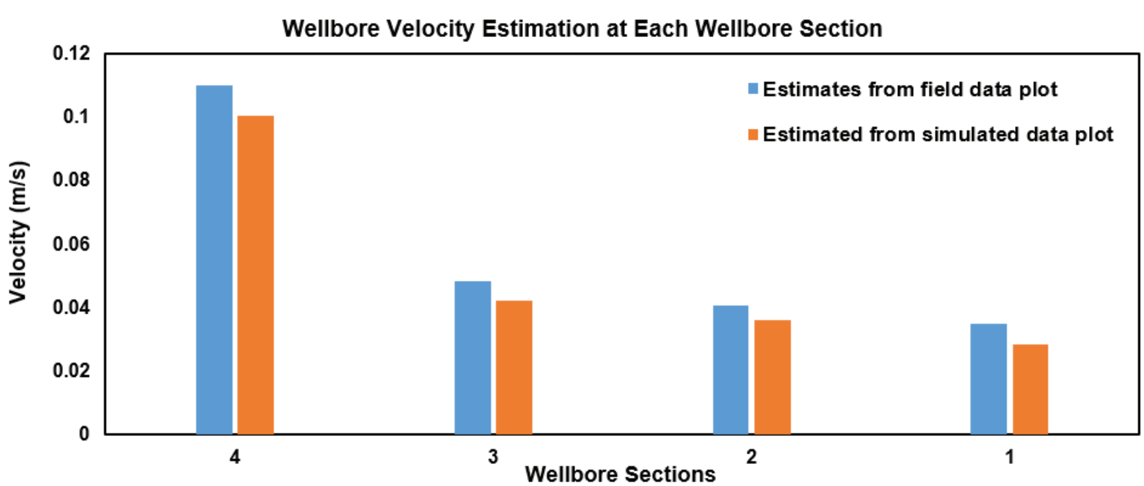

Figure 7.18: Wellbore section velocities within different stages of the producer estimated from the field fiber optic data and the simulated fiber optic waterfall.

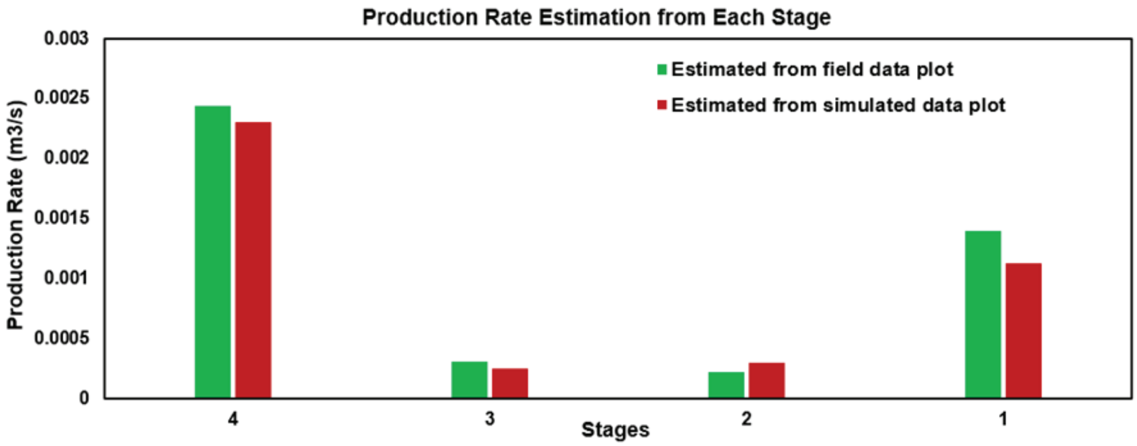

Figure 7.19: Wellbore section velocities within different stages of the producer estimated from the field fiber optic data and the simulated fiber optic waterfall.

8. Integration of Fiber Optic Data with FMI and Chemical Tracer Data to Evaluate Inter-well Fracture Connectivity and Fluid Circulation in Geothermal Well Pairs

8.1 Downhole Monitoring Data from the Utah FORGE EGS Test Site

At the Utah FORGE test site, three stages of hydraulic fracturing stimulation were completed in April 2022 without proppant injection. The production well 16B was drilled and completed in April 2023. Formation micro-resistivity imaging (FMI) log was employed during this drilling process to detect pre-existing fractures and faults along the producer (Jones et al., 2025).

Stages 3R to stage 10 in 16A were completed later in April 2024 with additional fracturing stages still to be planned. During most of these stages, proppant was used. Fiber optic distributed sensing was employed to monitor the fracture intersections along the production well 16B originating from the adjacent injection well (stage 3R to stage 10 in 16A). During the hydraulic fracturing treatment of each 16A stage (from stage 3R to stage 10), a specific set of chemical tracers was injected along with the fracturing fluid for quantifying the flow contribution, tracking the connectivity, and characterizing the fracture system (Fredd et al., 2025).

Following the stimulation of production well 16B, fiber optic monitoring remained active throughout the April 2024 fluid circulation test. During the early stages of circulation, thermal slugging behavior, characterized by abrupt temperature changes along the wellbore, were observed in the fiber optic waterfall plot originating from the five perforated stages completed along well 16B. Additionally, since Stages 3R to 10 in well 16A were injected with different signatures of chemical tracers during the hydraulic fracturing treatment, the injected tracers was extracted from the production well 16B during fluid circulation through conductive pathways created by the corresponding treatment stages of the injection well 16A. Fredd et al. (2025) reported that the production contribution of each 16A stage can be obtained from the tracer production during the EGS fluid circulation test.

This work aims at integrating fiber optic distributed sensing data with FMI log and tracer data collected from the Utah FORGE EGS test site. Locations and inclinations of pre-existing fractures and faults along the production well 16B collected from the FMI log were compared to the "frac hits" signals in the fiber optic strain rate waterfall for assessing fracture growth and intersections during April 2024 injection well stimulation. The stage flow contribution delivered from the chemical tracer data was matched with the production allocation calculated from the thermal slugging velocities in the fiber optic waterfall plot during the corresponding fluid circulation test. The unique and comprehensive downhole diagnostic dataset, at the FORGE site, provides an invaluable opportunity to better understand and confirm the subsurface processes within EGS development by combining different perspectives from various monitoring techniques.

8.2 Integration of Fiber Optic Data with FMI Log

The formation micro-resistivity imaging (FMI) log collected during the drilling process of the production well 16B is introduced to evaluate the fracture propagation and reorientation during the hydraulic fracturing treatment of the injection well 16A. Contrast between the measured depths of the natural fractures from FMI data and the fracture-driven interactions from the fiber optic waterfall plot is presented to better understand how the development of EGS fracture network is reflected in the fiber optic data.

8.2.1 Shifts in the injector perforation depths and production intersections

Fiber optic data is usually visualized in the form of waterfall plot where the distributed sensing data is plotted against measured depth and operation time (Figure 3.4 and Figure 3.7). During the April 2024 injection well stimulation at the FORGE site, fiber optic distributed sensing continuously monitored the locations and time of fracture intersections along the production well 16B where the fiber cable was deployed. Analysis of fracture-driven interaction signals, as captured in fiber-optic strain rate waterfall plots, reveals notable discrepancies between the perforation locations in the injection well and the corresponding fracture intersection points along the production well (Figure 5.2). These observations indicate that hydraulic fractures undergo significant reorientation and turning during multi-stage stimulation, particularly in the later stages of the treatment.

Using a fully implicit pad scale hydraulic fracturing simulator that models multi-stage fracture propagation and reservoir geomechanics with a combined finite volume (FV) and finite area (FA) approach, Ou et al. (2025c) simulated the Utah FORGE April 2024 injection well stimulation. Discrepancies between injector perforation locations and fracture intersections along the producer observed from the fiber optic data were proposed to be caused by the cumulative stress shadowing effect. Stress shadowing leads to fracture reorientation and the stress shadow increases as more fracture stages are stimulated. Fractures in later stages exhibit a greater tendency to turn toward the heel, resulting in higher-angle intersections with production well.

The fiber optic modeling results were outputted by sampling the reservoir deformation along the production well 16B (Figure 5.8). Classical "heart-shaped" strain rate signals are observed in earlier fracturing stages suggesting the time and locations of "frac-hits" at the monitor well (Liu et al. 2020). Unsymmetric turning signals are observed, which corresponds to the fracture reorientation in the numerical modeling results. The gradient of the turning signal increases in later stages, suggesting the accumulating effect of stress shadow as the multi-stage hydraulic fracturing treatment proceeds. However, the idea of stress shadow induced fracture reorientation remains insufficient in explaining some of the strong turning signals in later stages of the April 2024 16A well stimulation. Two strong reorientation events are observed at the beginning of injection in stages 8 and 9 (Figure 3.7), suggesting rapid arrivals of fractures at the production well with large reorientation angles. Therefore, apart from fracture reorientation in the horizontal plane due to stress shadowing effect, fracture-fault interaction in the vertical plane (Guo et al., 2015) is proposed to be an alternative explanation to some of the fracture growth at the FORGE site.

8.2.2 Fracture-fault interaction

Fiber optic data is usually visualized in the form of waterfall plot where the distributed sensing Depending on the mechanical status of the pre-existing fracture/fault, the interaction between hydraulic fracture and fault in this work is divided into 2 parts: (1) smaller faults act as pre-existing planes of mechanical weakness within the rock, so they can strongly influence the trajectory of hydraulic fractures; (2) larger faults with more fragmented contact surfaces was directly reopened by hydraulic fractures after intersection.

It is hypothesized that the strong turning signals in the fiber optic waterfall data from the Utah FORGE site are induced by fracture–fault interactions, whereby hydraulic fractures intersect and subsequently propagate along pre-existing tectonic faults in the vertical plane of the geothermal formation. To investigate this hypothesis, a representative simulation model case is constructed to simulate fracture-fault interaction in the vertical plane (X-Z plane in Figure 8.1). The fully implicit pad scale hydraulic-fracturing simulator discussed by Ou et al. (2025c) is utilized. The numerical modeling approach for simulating multi-stage fracture propagation is discussed in detail by Manchanda et al. (2020) and Zheng et al. (2019, 2020).

The simulation only considers fracture growth in the X-Z plane and the effect of stress shadow on fracture reorientation is neglected, due to the large X-Z stress contrast. A vertical in-situ stress gradient is applied to promote upward fracture growth, with a fixed fracture half-length of 160 meters. Two major tectonic faults are embedded within the reservoir mesh, positioned above the potential vertical propagating path of stage 8 and stage 9. This preliminary fracture-fault interaction simulation is based on the following assumptions: (1) hydraulic fractures are unable to cross the fault planes upon intersection, and (2) tectonic faults represent pre-existing planes of mechanical weakness within the rock, so they can strongly influence the trajectory of hydraulic fractures. To reflect this mechanical contrast, the tensile strength of the reservoir rock KIc is reduced by 35% along the fault planes. During the stimulation of well 16A, this reduction in fracture resistance and potential for dilation along the fault renders it a preferred pathway for fracture propagation (Figure 8.2 and Figure 8.3). The reoriented fractures reach the producer 16B at larger angles and within a shorter time duration.

The corresponding simulated fiber-optic strain rate waterfall plot for this fracture–fault interaction scenario is shown in Figure 8.4. Two distinct turning signals are observed at the beginning of stages 8 and 9, exhibiting steep gradients and propagation characteristics that are consistent with the “red-blue” patterns identified in the field fiber optic monitoring data (Figure 3.4). Simulation results in which fractures grow along pre-existing faults intersect the producer 16B at larger angles and in a shorter time. The presence of these mechanical weakness planes provides a plausible explanation for the rapid and directional fracture propagation, suggesting that fracture–fault interactions can give rise to additional, high-magnitude reorientation signals beyond those caused by the accumulated stress shadow during multi-stage hydraulic fracturing.

8.2.3 Pre-existing faults from FMI log and frac-hits from fiber optic data

The primary fracture-driven interactions, observed in the fiber optic strain rate waterfall plot during injection well stimulation, are highlighted in Figure 8.5. “Frac-hit” signals, labeled with pink letters, were characterized by heart-shaped signatures that are typically indicative of the creation of new fractures. This type of fracture-driven interactions is proposed to be caused by small pre-existing faults that act as pre-existing planes of mechanical weakness within the geothermal formation. The resulting redirection of hydraulic fracture propagation when the pre-existing faults intersect the producer with angles will lead to unsymmetrically heart-shaped turning signals as expressed in Figure 8.4. On the contrary, the absence of heart-shaped signature in “frac-hits” signals labeled with green letters are associated with the reopening of large pre-existing faults rather than the initiation of new failures according to Srinivasan et al. (2025).

The FMI logs at the measured depths of primary fracture-driven interactions/connections from the fiber optic data monitored along producer 16B are summarized in Appendix A. The existence and inclination of pre-existing fractures/faults delivered from the FMI logs match well with the proposed “frac-hits” signals in the fiber optic waterfall plot. At the measured depths of “frac-hits” signals labeled with pink letters, the FMI logs show clear existence of faults. Particularly at the locations of signal “B”, “C”, “D” and “L”, the pre-existing faults are found to intersect the producer 16B at large angles. This suggests that small pre-existing faults may influence the trajectory of hydraulic fractures.

At the measured depths of “frac-hits” signals labeled with green letters, the FMI logs show dense pre-existing faults with apparently more fragmented contact surfaces. These large faults will be reopened by hydraulic fractures, leading to fiber optic strain rate signals that are not the classic heart-shaped signatures. Moreover, at the measured depth of signal “N”, a large region of dense pre-existing faults/fractures is observed in the FMI data, which suggests that hydraulic fractures originating from stage 3R, 4, 5 and 6 were all caught up by the same group of pre-exiting faults, thus leading to fracture-driven interactions at similar measured depth in the fiber optic strain rate waterfall plot.

The good correlation between FMI log and fiber optic monitoring data from the Utah FORGE test site suggests that, in hard-dry-rock formations with abundant natural fractures or faults, EGS fracture propagation is very likely to be affected by fracture-fault interactions. Fiber optic distributed sensing provides an effective method to determine the complex interactions between hydraulic and natural fractures and the resulting fracture network geometry.

8.3 Integration of Fiber Optic Data with Chemical Tracer Data

The flow contribution of each stage in injection well 16A was calculated based on the chemical tracer data extracted from the production well 16B during the April 2024 fluid circulation test. The stage connectivity between well 16A stages and well 16B stages drawn from the fiber optic data during well 16A stimulation are now compared with the production allocation along the production well 16B. The production profile can also be compared with that calculated from the thermal slugging signals in the fiber optic waterfall plot during the fluid circulation test. Good agreement between the production contributions of well 16B stages obtained from the fiber optic distributed sensing data and chemical tracer data will show the applicability of using thermal perturbations in fiber optic data for production allocation along an EGS producer. Moreover, the flow contribution per injection well stage reveals critical insights into the performance of EGS completion design regarding the connectivity, conductivity and uniformity of the created hydraulic fractures.

8.3.1 Stage connections detected in fiber optic data

Based on the previous discussion on fracture-fault interaction in Figure 8.5, the following conclusions can be drawn:

- Stage 1 in well 16B is apparently connected to Stage 3R, 4, 5 and 6 in well 16A.

- During the fracturing treatment of Stage 7 in well 16A, fracture reactivation signals were detected at the locations of previous fracture-driven interactions associated with Stage 6. Therefore, some fractures originating from Stage 7 in well 16A should overlap with fractures from Stage 6 and connect to Stage 1 in well 16B.
- Since Stage 7 in well 16A has 3 perforation clusters, this work assumes that one cluster within Stage 7 is redirected to previous fractures within Stage 6 and connected to the producer 16B at Stage 1. This assumption is consistent with the chemical tracer interpretation, which detected a flow connection between 16B Stage 1 and 16A Stage 7 as illustrated by the light blue line in Figure 8.7b (Fredd et al., 2025).
- During the fracturing treatment of Stage 8 in well 16A, fracture reactivation signals were detected at the locations of previous fracture-driven interactions associated with Stage 7. Given Stage 8 is perforated with 8 clusters, it is concluded that one cluster within Stage 8 is redirected to previous fractures within Stage 7 and connected to the producer 16B at Stage 2.
- The perfect match between one FDI signal during the stimulation of Stage 8 in well 16A and the thermal slugging signal of Stage 3 in well 16B suggests that another cluster of Stage 8 in well 16A is connected to Stage 3 in well 16B.
- During the fracturing treatment of Stage 9 in well 16A, fracture reactivation signals were detected at the locations of previous fracture-driven interactions associated with Stage 8. Given Stage 9 is also perforated with 8 clusters, it is proposed that two clusters within Stage 9 are redirected to previous fractures within Stage 8 and connected to the producer 16B at Stage 4.

8.3.2 Stage connections integrating the micro-seismicity data

Agreement between the pre-existing fractures observed in the FMI log and the fracture driven interactions detected in the fiber optic data suggest that fracture intersections at the producer 16B at the Utah FORGE site primarily resulted from the reactivation of pre-existing fractures/faults. Nevertheless, the relatively sparse distribution of pre-existing fractures is not sufficient to explain another field observation that some clusters/stages are caught up by the same natural fractures and intersect the producer at identical locations. The overlapping of fracture propagation was also clearly reflected in the micro-seismicity data (Figure 8.6) reported by Pankow et al (2025).

The micro-seismic clouds of Stage 3R, Stage 4, Stage 5 and Stage 6 coincide, while the micro-seismic clouds of the heel-side of Stage 8 overlaps that of Stage 9. Although the micro-seismic clouds of Stage 8 and 9 follow the same inclined fracture propagation plane, an obvious distance is seen between this fracture plane and the perforated clusters where the fractures initiate. The hypothesis of bedding plane redirection proposed by Srinivasan et al. (2025) can be adopted to address the overlapping fracture propagation where the fracturing fluid injection was redirected by large bedding planes to adjacent pre-existing fractures/faults. The recharged natural fractures were then reactivated and the corresponding fracture driven interaction signals were detected by the fiber optic cable along the producer 16B.

The stage connections between injector 16A and producer 16B are depicted in Figure 8.7a where the overlap of fractures in Stage 7 with Stage 6 and Stage 8 in well 16A agrees with the stage flow connections determined from the dynamic tracer response (Figure 8.7b). The flow connections measured from the dynamic tracer response provide confirmation of hydraulic connections between the various stages with each line representing at least one connection (i.e., the FDIs did not pinch off and lose conductivity after the stimulation treatments).

8.3.3 Stage connections and fiber optic 16B production allocation

Production allocation for 16B well derived from the thermal slugging signals indicate that Stage 5, 4 and 1 exhibit higher production rates compared to Stages 2 and 3, particularly Stage 5 (Figure 8.8). This observation aligns with the completion design of the injector well 16A as shown on Figure 8.9. Stages 2 in well 16B intersects most of the fractures originating from Stages 7 of the injector well 16A, which was stimulated without the use of proppant. Stage 3 in well 16B is inferred to be hydraulically connected to a small number of toe-side clusters from Stage 8 in well 16A. Fractures associated with Stage 3 are expected to exhibit poor conductivity. On the contrary, Stage 5 in well 16B intersects fractures from Stages 8, 9 and 10 of injector well 16A, all of which involved proppant injection into a larger number of perforated clusters (eight clusters were treated in Stage 8 and Stage 9). These contrasts in fracture conductivity and connectivity are clearly manifested in the thermal slugging signals associated with each production stage.

8.3.4 Flow contributions from chemical tracer data and fiber optic data during EGS circulation

Chemical tracer was injected during the hydraulic fracturing treatment of each stage along the injector 16A (from 3R to 10) and during the circulation tests. Prior to the EGS fluid circulation test, different signatures of chemical tracers will remain inside the fracture networks created by the corresponding 16A stages. As discussed in detail by Fredd et al. (2025), the fluid flow contribution among all 16A stages can be calculated by the concentrations of tracers extracted from the producer 16B during the fluid circulation test (Figure 8.10).

Based on the stage connections between injector 16A and producer 16B drawn from the fiber optic data, the production contribution of the 5 stages in 16B can be obtained according to the flow contribution per 16A stage during the April 2024 fluid circulation test. Assuming the injected fluid is distributed equally into all clusters of each 16A stage, the production contribution of each 16B stage can be calculated as the summation of the flow contribution of all connected clusters from the injector 16A (Figure 8.11). The production contribution per 16B stage derived from the thermal slugging velocity in the fiber optic data aligns closely with that from the chemical tracer data (Figure 8.12). This good agreement in both data sets further confirms the reliability of inflow allocation based on thermal slugging signals in the fiber optic data of EGS producer. The integration of fiber optic distributed sensing data and chemical tracer data provides a practical assessment of stage connections and production in this EGS well pair.

8.4 <u>Appendix A</u>

This Appendix presents the FMI logs at the measured depths corresponding to the primary fracture-driven interactions observed in the fiber optic strain rate waterfall plot during the April 2024 injection well stimulation. The data is presented in the sequence of measured depth along the production well 16B. The labels (from “A” to “N”) refer to the fracture-driven interactions classified in Figure 8.5.

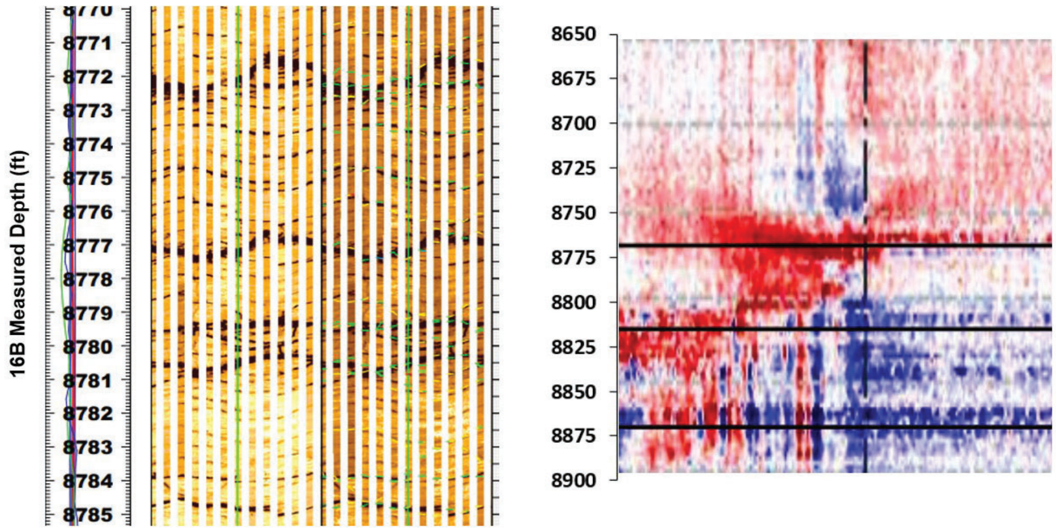

Figure A.1: FMI log and fiber optic "frac-hit" signal at the measured depth of fracture-driven interaction "A" observed in the fiber optic strain rate waterfall plot.

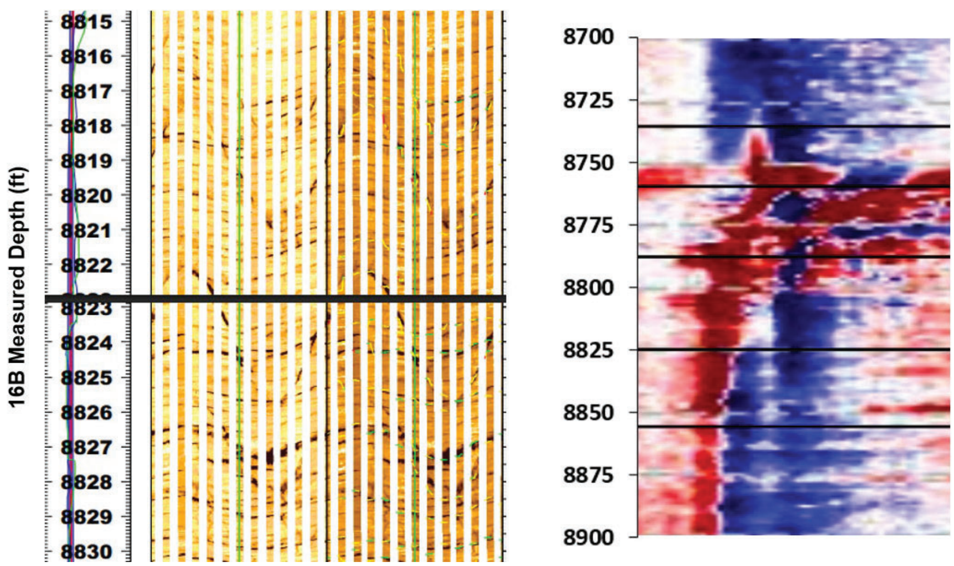

Figure A.2: FMI log and fiber optic "frac-hit" signal at the measured depth of fracture-driven interaction "B" observed in the fiber optic strain rate waterfall plot.

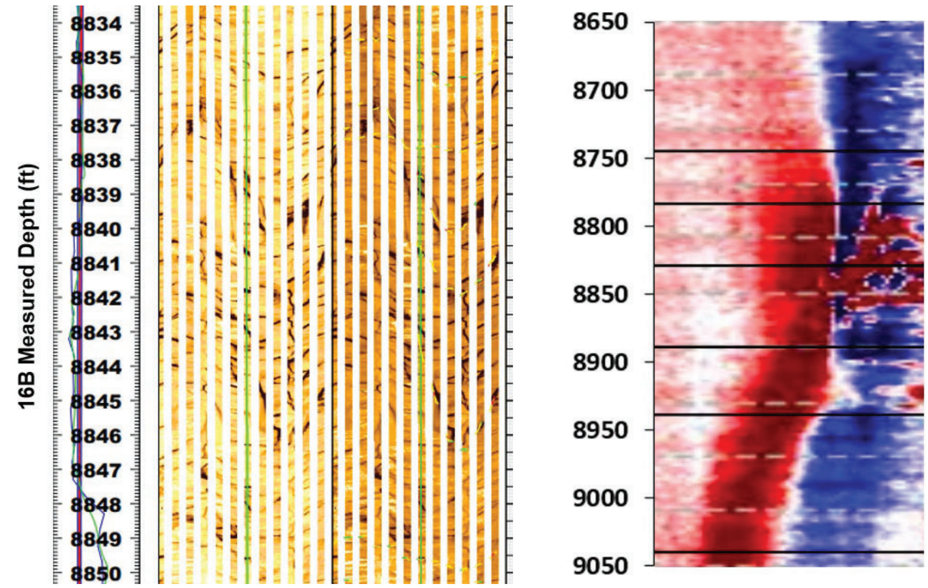

Figure A.3: FMI log and fiber optic “frac-hit” signal at the measured depth of fracture-driven interaction “C” observed in the fiber optic strain rate waterfall plot.

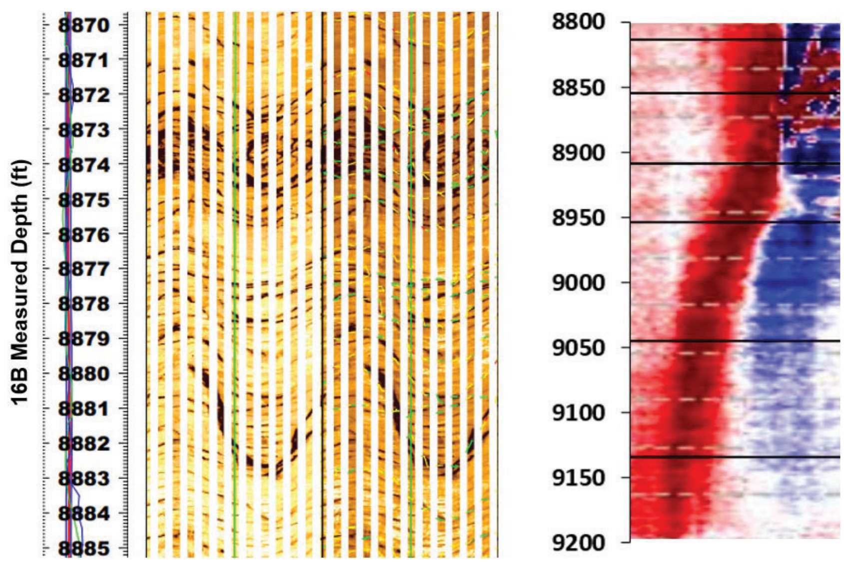

Figure A.4: FMI log and fiber optic “frac-hit” signal at the measured depth of fracture-driven interaction “D” observed in the fiber optic strain rate waterfall plot.

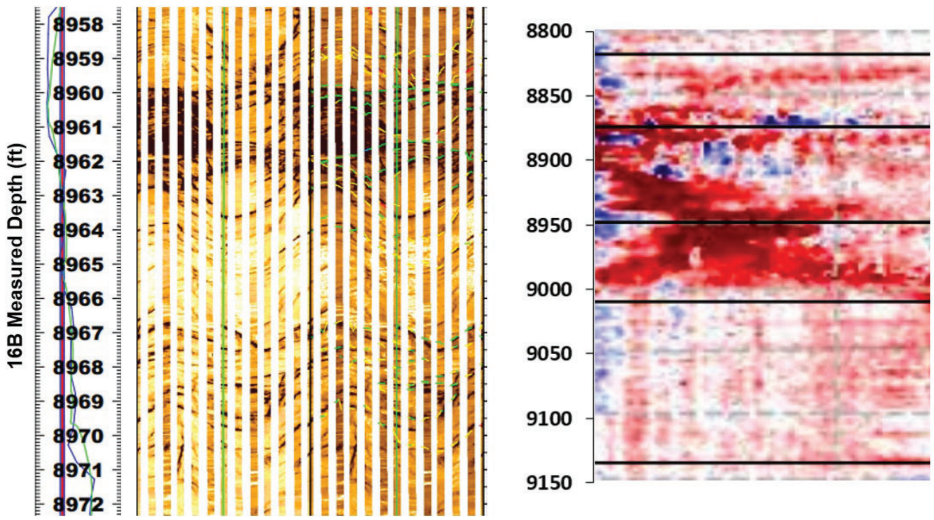

Figure A.5: FMI log and fiber optic “frac-hit” signal at the measured depth of fracture-driven interaction “E” observed in the fiber optic strain rate waterfall plot.

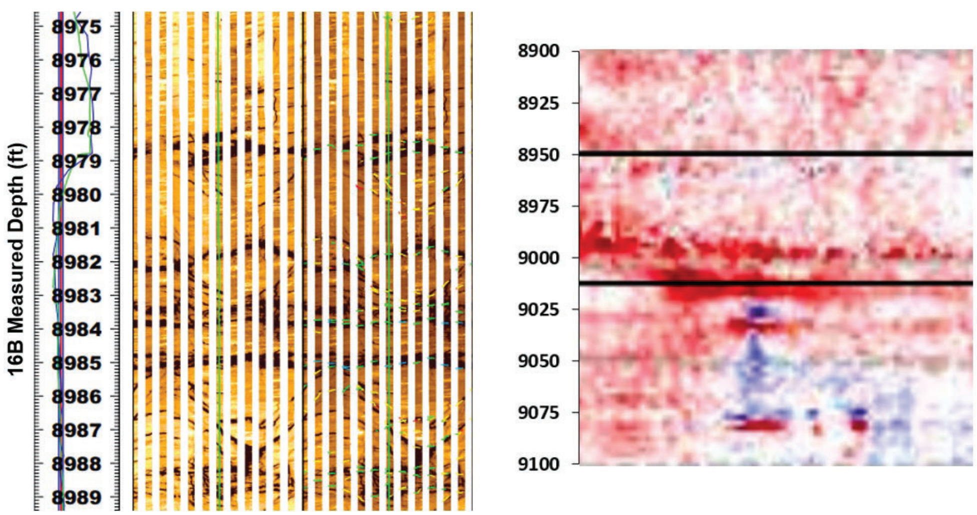

Figure A.6: FMI log and fiber optic “frac-hit” signal at the measured depth of fracture-driven interaction “F” observed in the fiber optic strain rate waterfall plot.

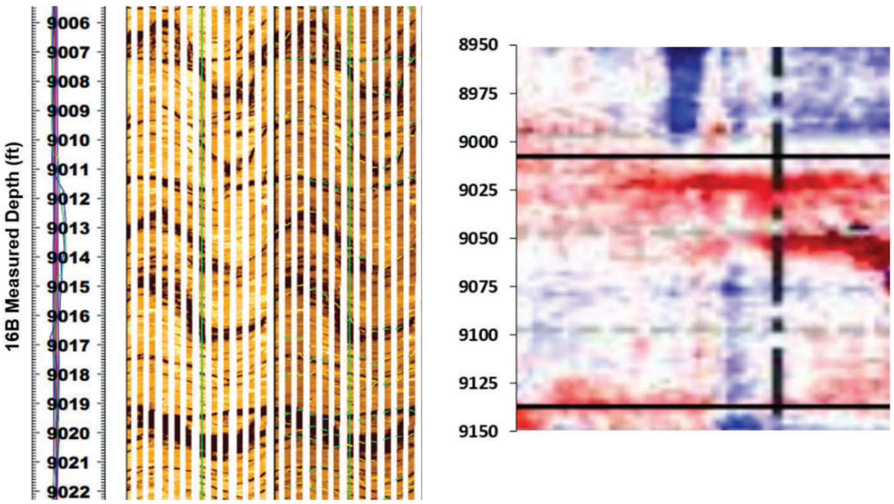

Figure A.7: FMI log and fiber optic "frac-hit" signal at the measured depth of fracture-driven interaction "G" observed in the fiber optic strain rate waterfall plot.

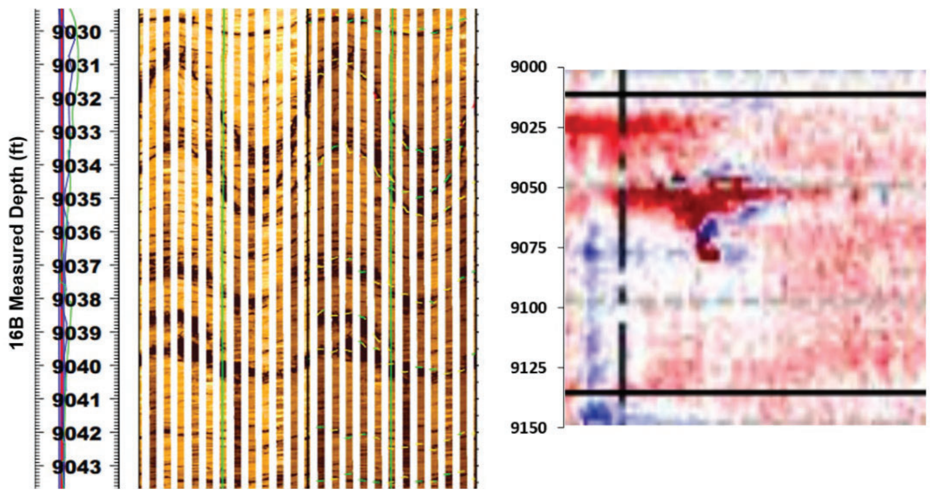

Figure A.8: FMI log and fiber optic "frac-hit" signal at the measured depth of fracture-driven interaction "H" observed in the fiber optic strain rate waterfall plot.

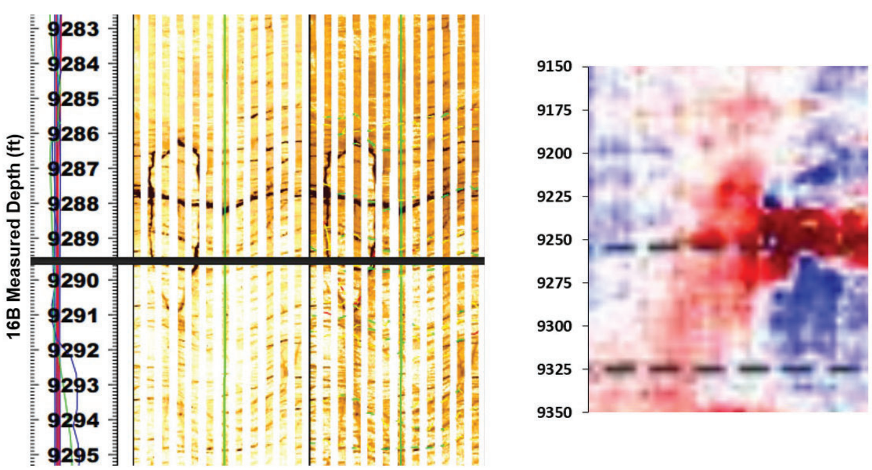

Figure A.9: FMI log and fiber optic "frac-hit" signal at the measured depth of fracture-driven interaction "I" observed in the fiber optic strain rate waterfall plot.

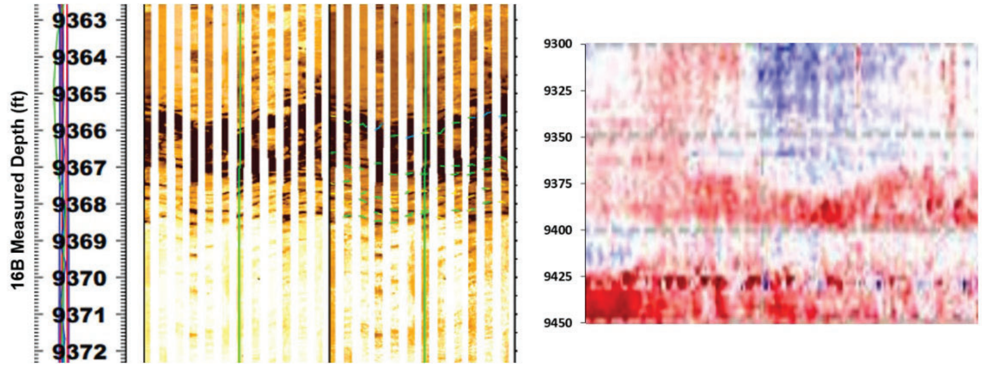

Figure A.10: FMI log and fiber optic "frac-hit" signal at the measured depth of fracture-driven interaction "J" observed in the fiber optic strain rate waterfall plot.

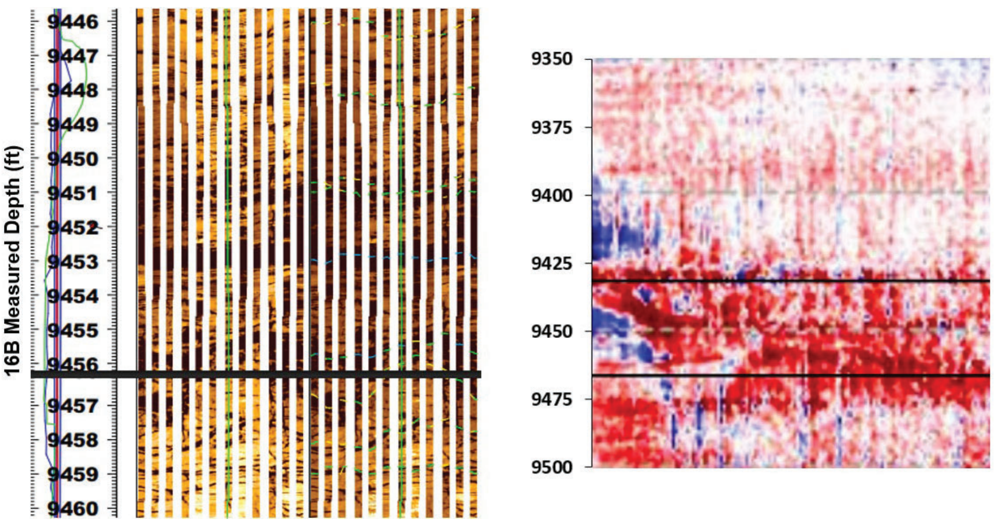

Figure A.11: FMI log and fiber optic "frac-hit" signal at the measured depth of fracture-driven interaction "K" observed in the fiber optic strain rate waterfall plot.

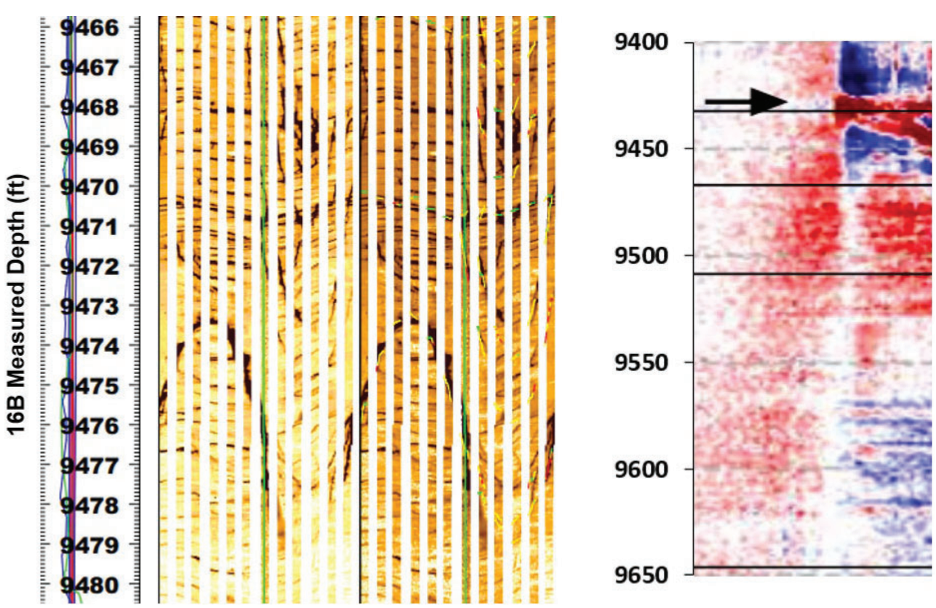

Figure A.12: FMI log and fiber optic “frac-hit” signal at the measured depth of fracture-driven interaction “L” observed in the fiber optic strain rate waterfall plot.

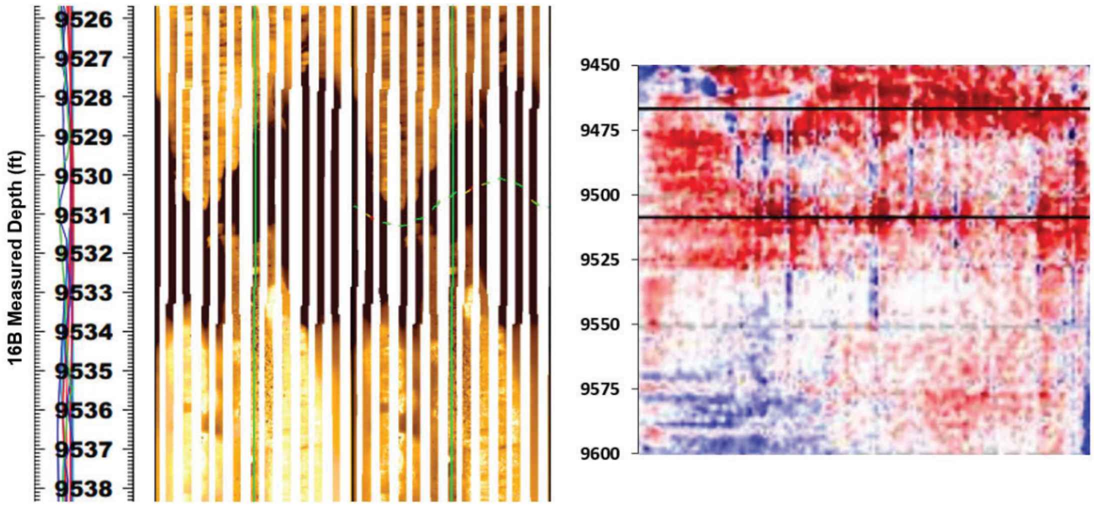

Figure A.13: FMI log and fiber optic “frac-hit” signal at the measured depth of fracture-driven interaction “M” observed in the fiber optic strain rate waterfall plot.

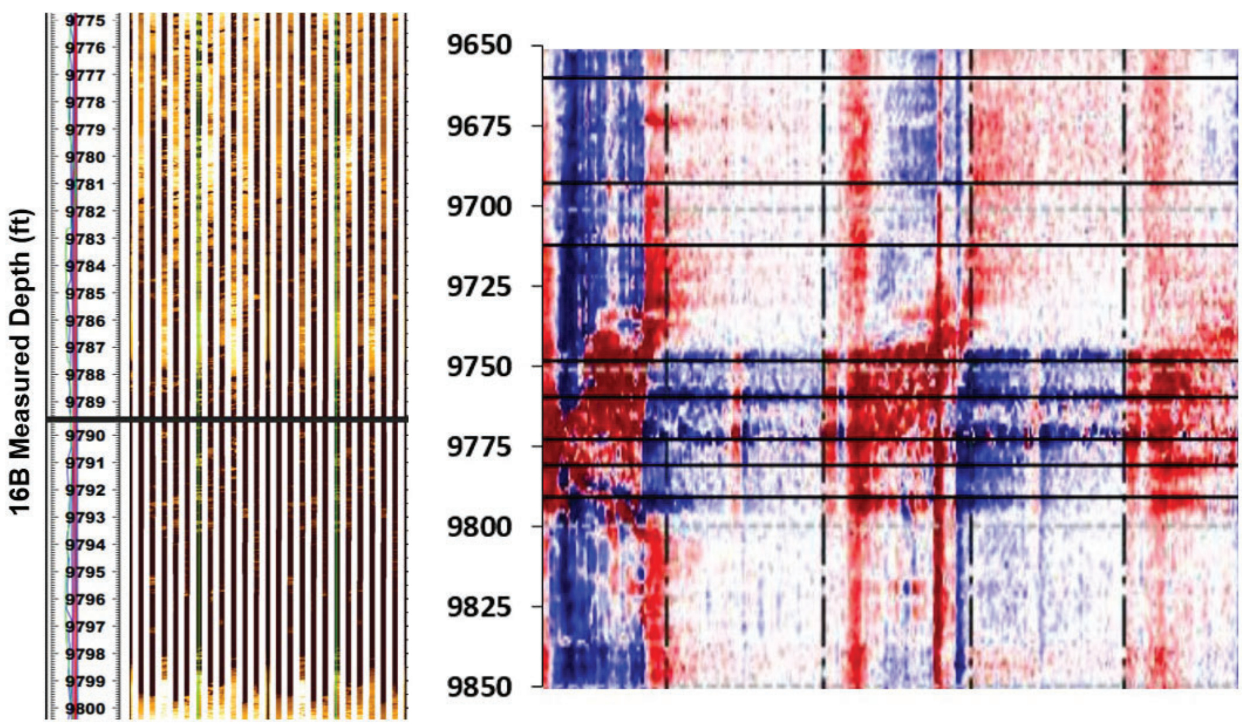

Figure A.14: FMI log and fiber optic “frac-hit” signal at the measured depth of fracture-driven interaction “N” observed in the fiber optic strain rate waterfall plot.

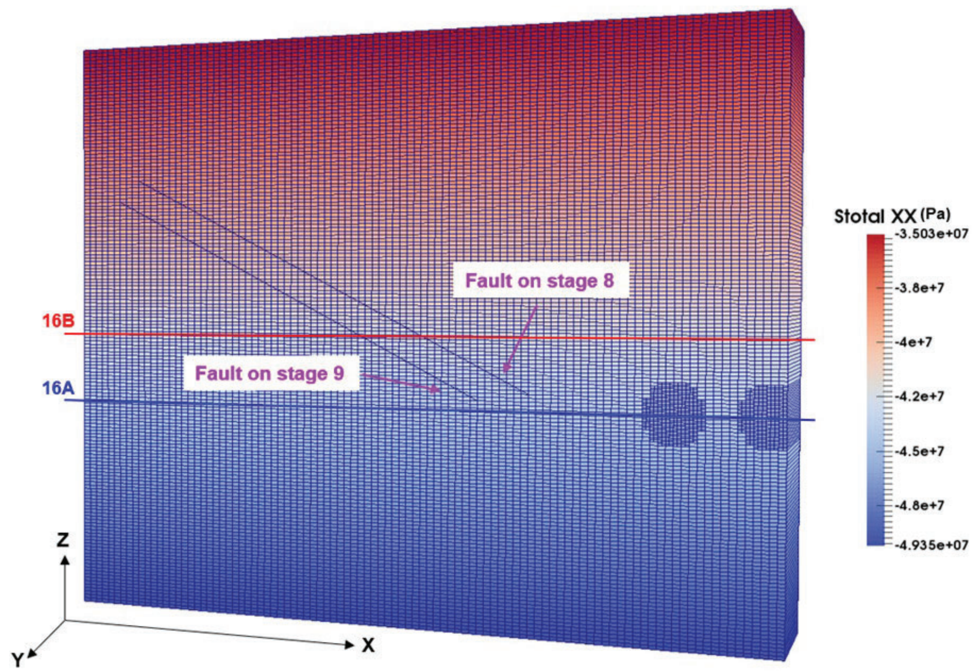

Figure 8.1: Computational mesh for the fracture-fault interaction case in the X-Z plane. Formation stress gradient is applied to promote upwards vertical fracture growth. Two pre-existing faults are placed above the fracture propagation paths of stage 8 and stage 9.

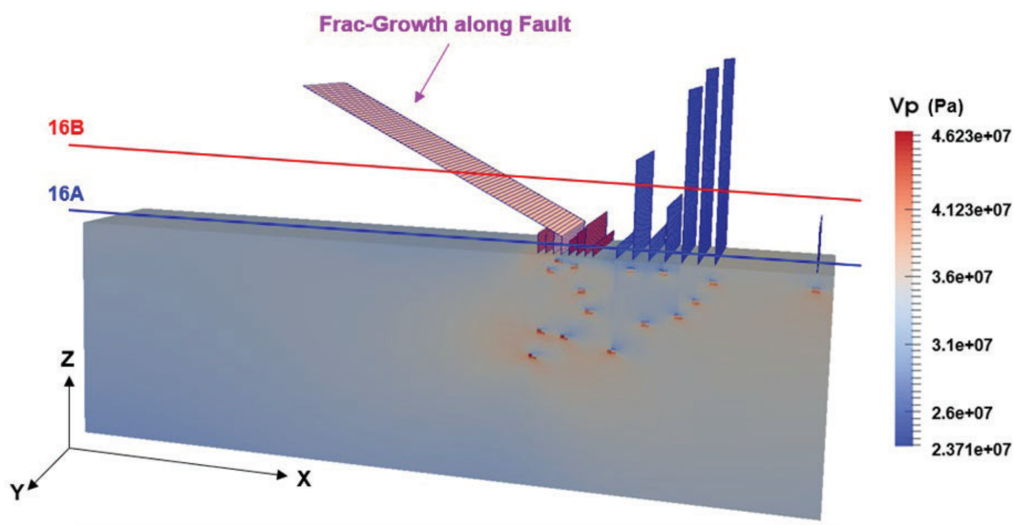

Figure 8.2: Fractures in stage 8 grow preferentially along the pre-existing tectonic fault as a plane of mechanical weakness. These reoriented fractures reach the producer 16B at larger angles and in a shorter amount of time.

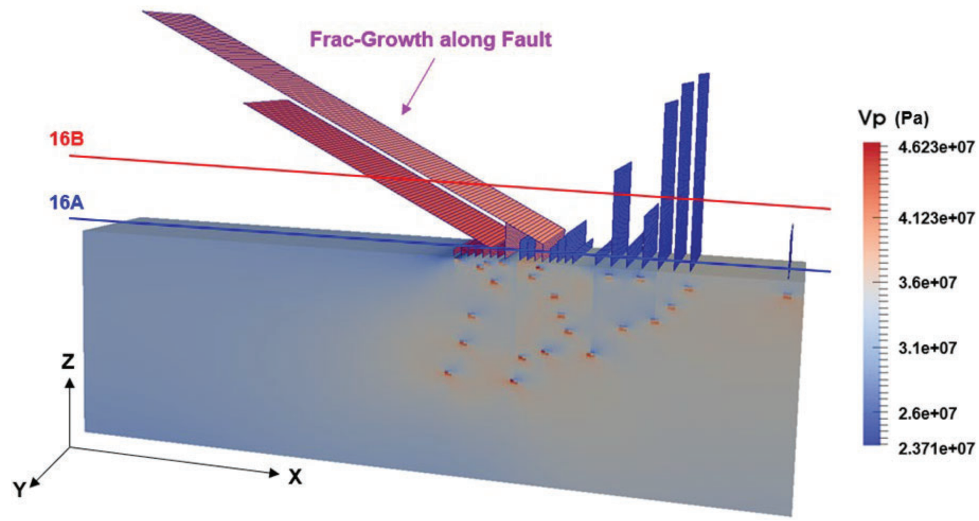

Figure 8.3: Fractures in stage 9 grow preferentially along the pre-existing tectonic fault as a plane of mechanical weakness. The reactivation of faults leads to 2 strong turning signals in the fiber optic waterfall plot.

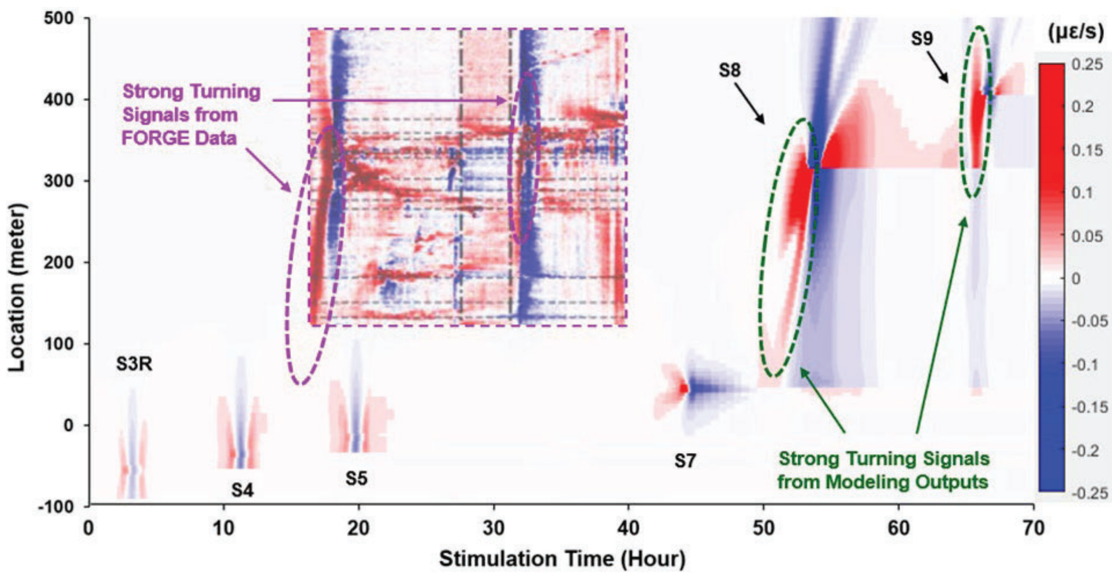

Figure 8.4: Modeling results of fiber optic strain rate waterfall of the fracture-fault interaction case. Strong turning signals, consistent with our fiber optic data, are observed at the beginning of Stage 8 and 9 treatments. In these simulations fractures are redirected by pre-existing faults.

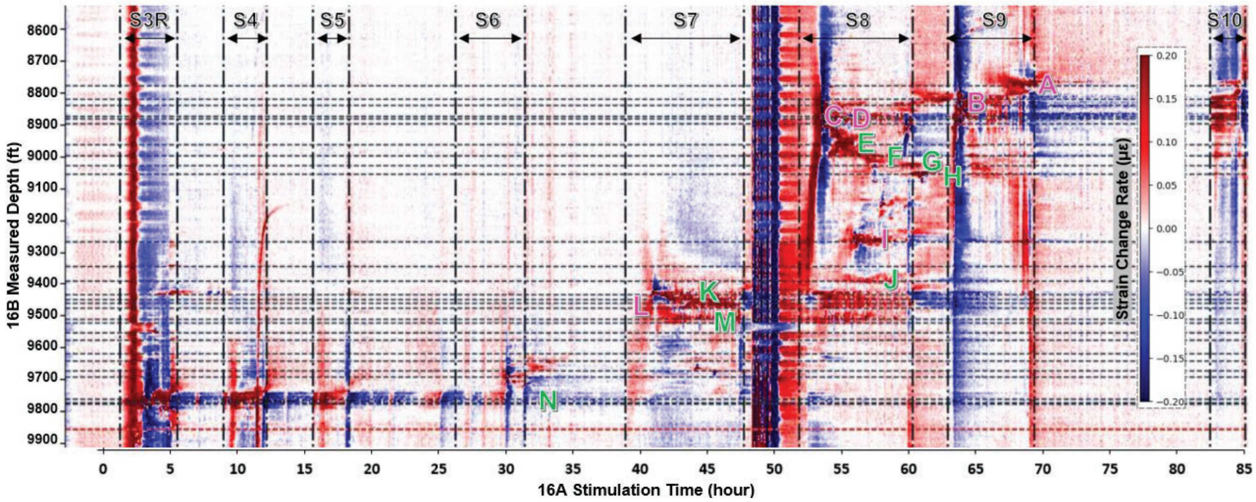

Figure 8.5: Primary fracture-driven interactions in the fiber optic distributed strain rate waterfall plot during April 2024 16A stimulation. Pink letters correspond to small pre-existing faults that redirect the path of hydraulic fracture propagation. Green letters correspond to large pre-existing faults that will be reopened by hydraulic fractures after intersection.

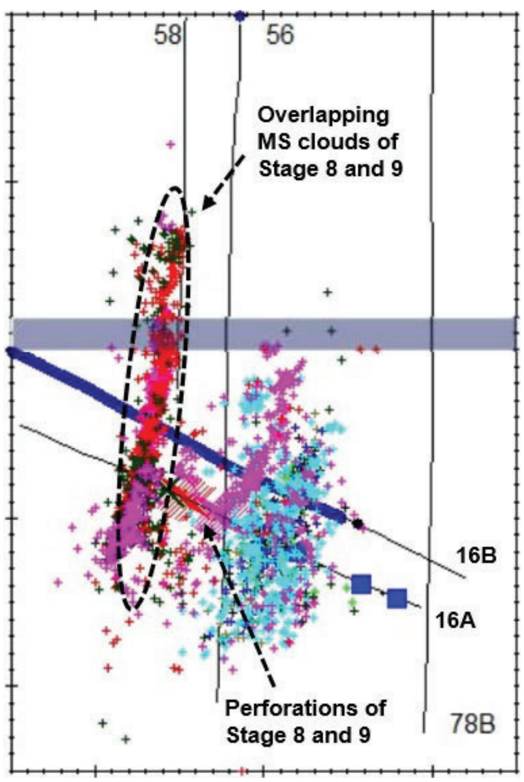

Figure 8.6: Micro-seismicity (MS) clouds data during the Utah FORGE April 2024 injection well stimulation (Pankow et al. 2025). The heel-side MS clouds of Stage 8 (depicted in pink color) follow the same inclined natural fracture with MS clouds of Stage 9 (depicted in red color).

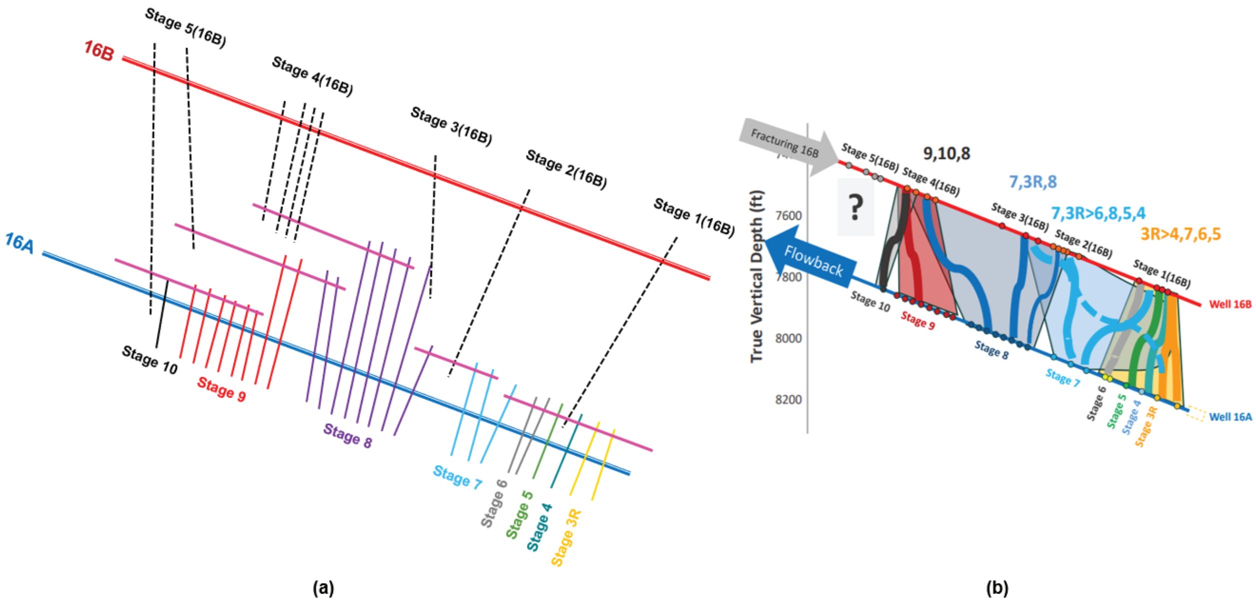

Figure 8.7: (a) Stage connections between injector 16A and producer 16B determined from the fiber optic data considering bedding plane (pink solid lines) and fracture-fault interaction. Black dashed lines represent pre-existing faults observed in the FMI log. (b) Stage flow connections determined from the dynamic tracer response (Fredd et al. 2025).

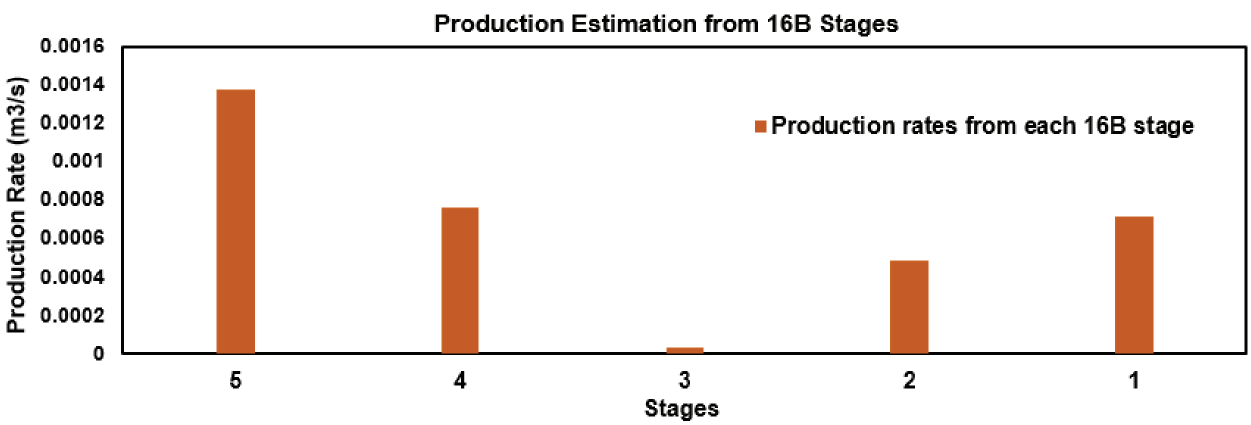

Figure 8.8: Production estimation along the production well 16B from fiber optic thermal slugging velocities (modified from Ou et al. 2025b).

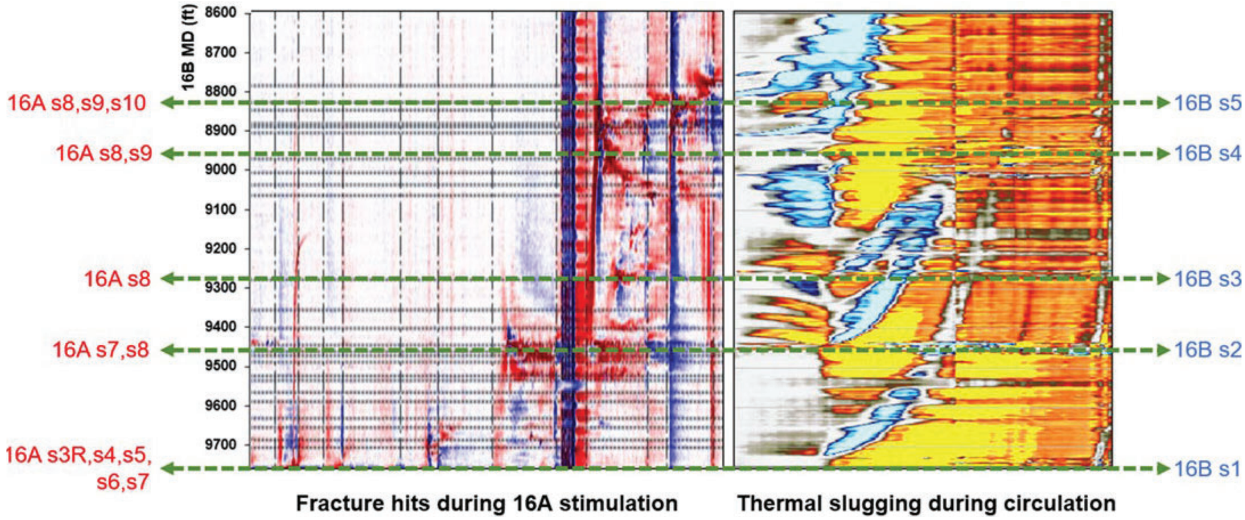

Figure 8.9: Comparison of fiber optic monitoring waterfall plots monitored during April 2024 16A stimulation and the following fluid circulation. The thermal slugging signals during early circulation originate from fracture intersection locations observed during the 16A stimulation. These main intersections are also locations where the production well is perforated.

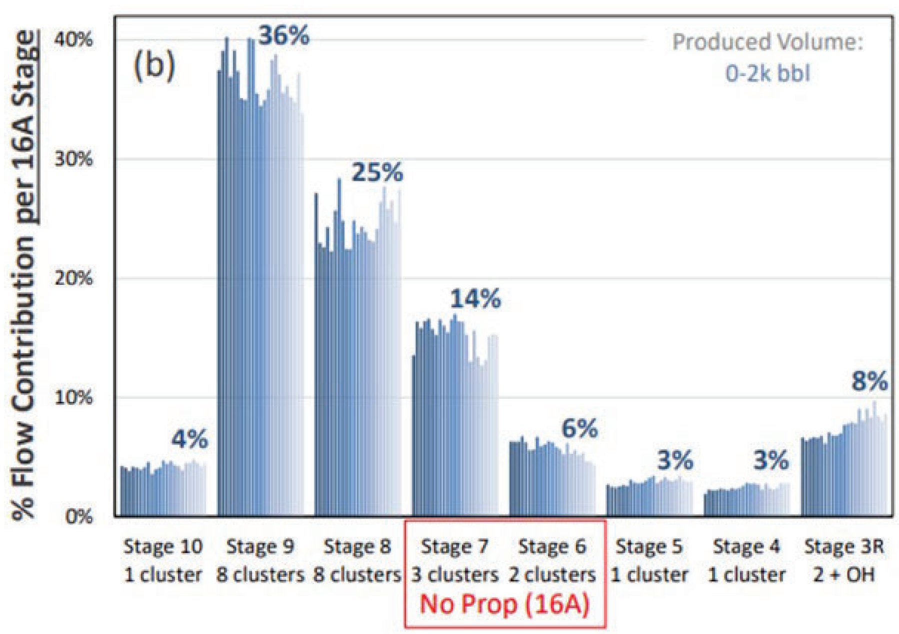

Figure 8.10: Quantitative estimates of the percent flow contribution for each 16A stimulation stage during the circulation test in April 2024 (Fredd et al. 2025).

16B Stage / 16A Stage	S1	S2	S3	S4	S5	16B Stage / 16A Flow%
S3R	1					8%
S4	1					3%
S5	1					3%
S6	1					6%
S7	1/3	2/3				15%
S8		1/8	1/8	1/2	1/4	25%
S9				1/4	3/4	36%
S10					1	4%
16A Stage / 16B Flow%	24.67%	12.46%	3.13%	21.25%	37.25%	16A Flow% / 16B Flow%

Figure 8.11: 16B production contribution derived based on the 16A-16B stage connections and the 16A flow contribution from the tracer data.

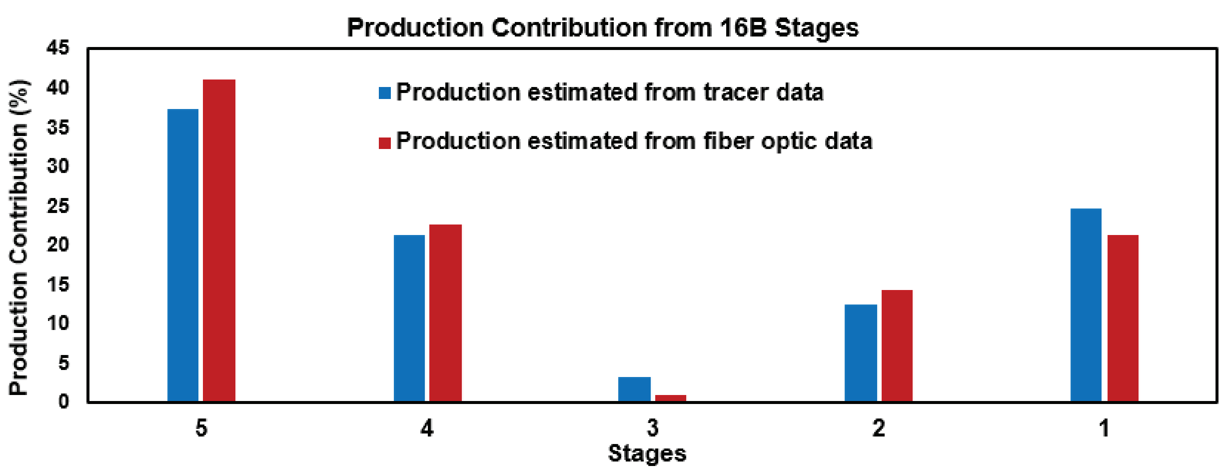

Figure 8.12: 16B inflow allocation percentages estimated from tracer data and fiber optic data. Good agreement is seen in the 16B production contributions derived from tracer data and fiber optic data.

9. Strategies for Improving Inter-Well Connectivity and Proppant Placement in EGS Well Pairs

9.1 Inter-well Connectivity and Uniformity in Fluid and Proppant Distribution

The effectiveness of an enhanced geothermal system (EGS) is strongly influenced by the hydraulic connectivity between injection and production wells, as well as the conductivity of the induced flow pathways. Unlike fracturing in unconventional oil reservoirs, where increasing the total surface area of created fractures is the priority, hydraulic fractures in geothermal injection wells must intersect production wells so that good fluid communication can be maintained between the wells. A uniform distribution of fracturing fluid and proppant are critical to ensure good inter-well connectivity within EGS well-pairs.

To address the non-uniform distribution of proppant and ensure that all clusters take proppant and slurry, changes need to be made to the completion and the fracture design. Multifrac-3D is used to investigate the performance of different fracture designs. Numerical models are constructed to simulate the Utah FORGE April 2024 fracturing treatments of both well 16A and 16B. An empirical correlation is incorporated to account for in-well proppant allocation and cluster screen-out due to perforation plugging. Modeling results of the injector 16A are used to assess fracture growth as well as the uniformity of fracture connectivity and conductivity, while 16B simulations focus on the distribution of injected slurry and proppant. By integrating the fiber optic data with the modeling results, key patterns of fracture growth and proppant placement are revealed suggesting ways in which well completion and fracture design can be modified to improve the EGS well performance.

9.2 Modeling Analysis of Fracturing Treatments in Injection Well 16A

In this section, we present numerical simulations and the corresponding analysis of the Utah FORGE April 2024 injection well stimulation. A fully implicit hydraulic fracturing simulator is utilized and details regarding the methodology of this coupled simulator can be found in Appendix A. Modeling results and interpretation of injector 16A will focus on the created fracture geometry and the inter-well connectivity. The insights regarding fracture intersections at the producer 16B as well as the uniformity of fracture conductivity was compared to the observations from the FORGE fiber optic monitoring data (Jurick et al., 2025) and chemical tracer data (Fredd et al. 2025).

9.2.1 Model setup

A three-dimensional Base Case model was constructed to simulate the Stage 9 hydraulic fracturing treatment of well 16A during the FORGE April 2024 injection well stimulation. The computational domain dimensions were set to $1000 \times 800 \times 120m^3$ in the x, y, and z directions, respectively, as illustrated in Figure 9.1. The production well 16B is situated approximately 100 m vertically above the injection well 16A. To ensure an accurate resolution of fracture growth, mesh refinement was applied in the vicinity of the treatment interval at the corresponding measured depth. To capture the realistic mechanical behavior of the subsurface, an in-situ stress gradient was imposed across the reservoir domain, allowing for a more representative simulation of hydraulic fracture propagation in enhanced geothermal systems.

The Base Case simulates a six-hour fracturing treatment aligned with the actual pumping schedule executed for Stage 9 of well 16A (Figure 9.2). The multi-cluster hydraulic fracturing simulation is set-up according to reservoir parameters, in-situ conditions and completion designs specific to the Utah FORGE EGS test site. The general reservoir-fracture-well simulation inputs for the Base Case are summarized in Table 9.1.

9.2.2 Base case results

Simulated fracture geometry at the end of the 6-hour fracturing treatment is shown on Figure 9.3. The cluster spacing is enlarged by 10 times for observation convenience. Since the hard-dry-rock formation has a high Young's modulus of 54.8GPa, the effect of stress shadowing is very evident among the 8 created fractures. The in-situ vertical stress gradient promotes upward fracture growth and fluid gravity helps the fractures propagate downward. Therefore, fractures in the Base Case simulation avoid each other by growing upwards and downwards due to the stress shadow (Guo et al., 2017). The large effect of stress shadowing and the small cluster spacing substantially restrict the fracture propagation of fractures emanating from the inner clusters. The proppant allocation updated according to Eq. 8 leads to toe-side dominated proppant distribution along the treatment stage. Perforation plugging is observed in the toe-side cluster "C8" where 16 out of 18 perforations are plugged at the end of the stage treatment. This will dramatically reduce the fluid injection into the toe-side cluster at later time, so the heel-side fracture becomes the dominant conductive pathway.

The Base Case shows poor inter-well connectivity. Of the 8-clusters, 4 fractures act as thief-fracture zones. This is consistent with the results derived from the fiber optic monitoring data and the chemical tracer analysis during the corresponding EGS fluid circulation test. In Figure 3.4, Stage 9 in well 16A has obviously fewer fracture-driven interaction signals (the sign of fracture intersection at the producer 16B according to Jurick et al., 2025) compared with Stage 8 in the fiber optic waterfall plot. In addition, during the April 2024 fluid circulation test the chemical tracer data (Fredd et al., 2025) shows that there is a dominant hydraulic connection in Stage 9.

The existence of such thief-fracture zones with substantially higher conductivity is harmful to the overall performance of EGS thermal recovery where a uniform distribution of fracture conductivities is the priority. Therefore, the stage treatment strategies should be modified to (1) increase the number of fracture intersections; and (2) achieve a more uniform distribution of fracture conductivity.

9.2.3 Effect of fluid viscosity

We explore the impact of fracturing fluid viscosity on fracture propagation dynamics, proppant placement, and stress shadow development among adjacent clusters. During the April 2024 stimulation of well 16A, various fluid types were employed across different stages. Specifically, slickwater was used in Stages 9, while crosslinked gel was injected in Stages 8. To investigate the influence of fluid rheology, two sensitivity simulations were performed by increasing the viscosity of the fracturing fluid from 1cp to 20 cp and 100 cp.

Simulated fracture geometries of cases with fracturing fluid viscosities of 20 cp and 100 cp are presented in Figure 9.4. Comparing these results with the Base Case results using slick water (Figure 9.3), it is evident that increasing the viscosity of fracturing fluid promotes more uniform fracture propagation across multiple clusters. High viscosity fluids can better transport the proppant in the wellbore and into the perforations so that the proppant and slurry are more evenly distributed into all clusters. This reduces the dominance of certain clusters and the stress shadow effect that often leads to uneven fracture growth. Modeling outputs of the two fluid viscosity sensitivity cases show no perforation plugging throughout the stage treatment. This reduces the possibility of the occurrence of thief-fracture zones.

In Figure 9.4b (where the frac fluid viscosity is 100 cP) all 8 fractures are well connected to the producer 16B with a good uniformity in fracture conductivity. The good inter-well connectivity in the modeling outputs aligns with FORGE fiber optic monitoring data as depicted in Figure 3.4 where Stage 8 with cross-linked gel has obviously more connected fractures than Stage 9 with slick water.

High viscosity fracturing fluid also increases the total surface area of the created hydraulic fractures since the fluid leak-off volume into the surrounding formation will be dramatically reduced as the fluid viscosity increases. Moreover, as shown in Figure 9.5, larger pressure difference is needed in the fracture-wellbore system to sustain fracture propagation with high viscosity fluid (injection volume is identical). This results in higher average fluid pressure within the fracture, which further enhances the fracture surface area. Larger fracture height has an advantage in supporting EGS fluid circulation with larger well spacing, which would significantly improve the long-term thermal extraction.

9.2.4 Effect of completion design

The injection well 16A incorporated 18 perforations per cluster for Stage 8 and Stage 9, causing resulting in a very small flow rate and pressure drop in each perforation. The nonuniform fluid distribution can be mitigated by employing a limited entry completion design where the number of perforations per cluster is reduced. Limited entry perforation increases the perforation pressure drop and maintains sufficiently high injection pressure to promote a more balanced distribution of fluid across all clusters. This approach addresses low cluster efficiency due to stress shadow and minimizes preferential growth toward the outermost or more compliant fractures.

Two sensitivity simulations, in which the perforations per cluster decreased to 6 and 2, were performed to study the influence of such limited entry designs. Simulated fracture geometries for cases with 6 and 2 perforations per cluster are presented in Figure 9.6. The high perforation pressure drops force an even fluid distribution and increases the uniformity of fracture surface areas. However, there is no significant improvement in fracture connections at the producer since the fracture and wellbore hydraulics are not changed due to the unaltered fracturing fluid viscosity. Fracture geometry created under limited entry completion will remain relatively nonuniform due to the large stress shadow among fractures. Moreover, toe-side dominated proppant distribution as well as perforation plugging were still observed in both limited entry cases. Overall, reducing the number of perforations per cluster improves EGS inter-well connectivity by promoting even fluid injections, but the influence is not significant in contrast to the approach utilizing high viscosity fracturing fluid.

9.2.5 Effect of pumping schedule

In typical hydraulic fracturing treatments, the stage pumping rate will gradually increase from zero to a maximum value within certain period (around half hour). However, this injection pressure build-up duration might have a negative effect on uniform fracture growth. A sensitivity case employing the maximum pumping rate at the beginning of the fracturing treatment was performed and the simulated fracture geometry is shown in Figure 9.7b. The modeling results show a more uniform fracture geometry when pumping the maximum rate at the beginning of fracturing treatment.

When the fluid injection ramps up slowly, the pressure may first exceed breakdown pressure at only the weakest cluster (typically the outer clusters). The dominant clusters initiate first, take most of the fluid, grow preferentially and suppress neighboring clusters via stress shadow.

Applying the maximum injection rate at the onset of pumping generates a more rapid pressure equilibration across all perforation clusters, allowing fractures to initiate and propagate more uniformly before large stress shadows develop. This reduces early fracture dominance and results in a more uniformly developed fracture network.

9.3 Fiber Optic Monitoring Data and Modeling Interpretations of Treatment in Production Well 16B

This section first introduces the fiber optic data acquired during the fracturing treatment of the production well 16B. Numerical simulations and the corresponding analysis of the Utah FORGE April 2024 production well stimulation is then presented. The model set-up is based on the previous simulations regarding the injection well stimulation. The modeling outputs and discussion was concentrated on the allocation of fracturing fluid and proppant. The evolution of injection contribution is analyzed to get information regarding perforation plugging and cluster screen-out.

9.3.1 HF-DAS data during the stimulation of well 16B

Figure 9.8 shows high frequency DAS data from Stage 3 in well 16B during its hydraulic fracturing treatments conducted in April 2024. This is a representative data set for one stage and results for other stages are shown in Appendix B. It is evident from the data that for all stages, the toe side clusters take proppant for only the early part of the treatment. After some time, the perforations screen out and no more fluid/proppant enters the toe side clusters, resulting in a very non-uniform placement of proppant in the treatment stage.

We simulated the fracture treatments in well 16B to explore how the treatments can be improved. As shown earlier. DAS data clearly indicate heel dominated fractures. Several completion and fracturing design parameters were changed to show that it is possible to get more uniform proppant placement in all the clusters.

9.3.2 Modeling well 16B: base case results

The Base Case represents the reference fracturing condition of Stage 3 in production well 16B stimulation. Figure 9.9a presents the final cluster-level fluid allocation. The results show that the heel cluster receives the largest fraction of injected fluid, while the toe cluster contributes the least, indicating strong non-uniformity along the stage. Figure 9.9b shows the final proppant allocation, which mirrors the fluid trend, most of the injected proppant accumulates near the heel cluster, while the toe cluster receives only a small fraction.

Figure 9.10 depicts the temporal evolution of fluid and proppant distribution among clusters. During the initial stages of pumping, the flow distribution is nearly uniform. However, as the injection continues and the local proppant concentration increases, bridging and deposition begin first near the toe perforations. The formation of local bridges restricts the effective flow area and causes a sharp decline in toe-side inflow. Once the toe cluster begins to plug, the injected fluid is diverted toward the middle and heel clusters. With time, the middle cluster also starts accumulating proppant, while the heel cluster remains the primary open flow path. This sequence matches the high-frequency DAS data (Figure 9.8), where toe-side acoustic energy decays earlier while heel-side strain signals persist for longer durations.

9.3.3 Methods to optimize proppant and fluid distribution in clusters

Achieving uniform fluid and proppant placement across perforation clusters is critical for maximizing fracture efficiency and ensuring balanced stimulation along the wellbore (Guo et al., 2015). By mitigating heel dominance and promoting even proppant transport, overall fracture conductivity and stage productivity can be significantly improved. In this study, three optimization strategies are evaluated to enhance near-wellbore flow distribution and improve proppant placement:

(1) The application of viscous carrier fluids to stabilize slurry transport and delay early bridging,

(2) The use of lightweight proppants to increase particle suspension time and reduce gravitational settling, and

(3) The adoption of a tapered perforation design to counteract wellbore pressure losses through hydraulic balancing.

The following sections present and compare the results from each method, highlighting their influence on fluid allocation, proppant transport, and screen-out progression relative to the Base Case.

9.3.4 Effect of fluid viscosity

Fluid viscosity plays a crucial role in governing near-wellbore flow distribution and proppant transport. In slickwater fracturing, the low-viscosity carrier fluid offers minimal resistance to flow imbalances along the wellbore, allowing the upstream (heel-side) clusters to draw a disproportionately larger fraction of fluid and proppant. Increasing the viscosity of the injected fluid enhances momentum coupling between the fluid and suspended particles, reduces inertial segregation, and stabilizes the flow regime across perforations. To evaluate this effect, two simulations were performed with fluid viscosities increased by an order of magnitude (10 cP) and two orders of magnitude (100 cP) relative to the base case.

Figure 9.11 presents the final cluster-level fluid allocations for the base case, 10 cP, and 100 cP simulations, while Figure 9.12 shows the corresponding proppant allocations. Compared with the base slickwater case (1 cP), both the 10 cP and 100 cP cases exhibit a distinctly more uniform distribution of injected fluid and proppant along the stage. At 10 cP, the heel cluster no longer dominates the inflow, and the middle and toe clusters contribute a larger share of the total volume. When viscosity increases to 100 cP, the allocation becomes nearly balanced among all clusters.

Figure 9.13 shows the temporal evolution of cluster-level fluid allocation for the base, 10 cP, and 100 cP simulations, while Figure 9.14 presents the corresponding proppant allocation versus time. At the early stages of pumping, all clusters exhibit comparable inflow. As injection proceeds in the 10 cP case, the toe cluster begins to experience localized proppant bridging. In contrast, the 100 cP simulation maintains a nearly uniform flow partitioning throughout the entire pumping duration, with no significant toe-side plugging observed. Consequently, increasing fluid viscosity is an effective means of reducing flow asymmetry, delay screen-out, and achieve balanced near-wellbore inflow, ultimately improving stage efficiency and fracture uniformity.

9.3.5 Effect of lightweight proppant

April 2022 without proppant injection. The production well 16B was drilled and completed in Proppant density strongly influences the hydraulic and inertial behavior of particles within the slurry. In conventional fracturing operations, high-density sand particles (≈2650 kg/m³) tend to settle rapidly, especially in low-viscosity slickwater, resulting in uneven transport and early bridging near heel-side perforations. Reducing proppant density lowers its inertia and velocity relative to the fluid and improves hydraulic coupling with the carrier fluid, allowing the particles to remain suspended for longer, turn the corner into perforations and travel farther along the wellbore. To evaluate this effect, a lightweight proppant case (density ≈ 1010 kg/m³) was simulated using the same injection schedule and fluid properties as the Base Case.

Figure 9.15 presents the final cluster-level fluid allocation for the base and lightweight proppant cases, while Figure 9.16 shows the corresponding proppant distributions. Compared to the base case, both fluid and proppant allocations become more uniform across the clusters. The heel cluster no longer dominates flow intake, while the middle and toe clusters receive a larger and more sustained share of both fluid and particles.

Figure 9.17 illustrates the temporal evolution of cluster fluid allocation for the Base Case and the lightweight proppant case, while Figure 9.18 presents the corresponding proppant allocation versus time. The results show that the lightweight proppant leads to an almost perfectly uniform flow and transport behavior across the stage. Enhanced suspension of light-weight proppant prevents the early formation of proppant bridges near the toe, resulting in delayed or even suppressed plugging events. Overall, the use of lightweight proppant not only mitigates heel-dominated behavior but also ensures more homogeneous proppant placement, promoting effective stimulation of all perforation clusters.

9.3.6 Effect of tapered perforation design

Perforation geometry strongly influences near-wellbore flow balance and cluster efficiency. In the16B well, the large number of perforations (15 per cluster) combined with the relatively low injection rate caused very low-pressure contrast among clusters, leading to minimal sensitivity to geometric tapering. To better evaluate the impact of perforation design, the total perforation count was reduced to 10 per cluster, and this configuration was treated as the new uniform-perforation Base Case. A second simulation was then performed using a tapered design with 5, 10, and 15 perforations in the heel, middle, and toe clusters, respectively, while keeping the injection schedule identical.

Figure 9.19 presents the final cluster-level fluid allocation for the uniform 10-perforation base case and the tapered perforation case, while Figure 9.20 shows the corresponding proppant distributions. In the 10-perforation base case, the heel cluster continues to dominate fluid and proppant intake, receiving more than two-thirds of the injected solids, while the toe cluster remains under-stimulated. In contrast, the tapered design shows a markedly more balanced distribution, with the middle and toe clusters contributing nearly equal shares of the total proppant mass.

The temporal evolution of this behavior is shown in Figure 9.21 and Figure 9.22 for fluid and proppant allocations versus time, respectively. In the uniform-perforation case, the toe cluster plugs early, diverting subsequent flow toward the heel, whereas in the tapered design, all clusters maintain stable inflow throughout the pumping period. The progressive increase in perforation counts toward the toe balances the hydraulic resistance along the stage, delays bridging, and sustains toe participation until the end of the injection. The results demonstrate that optimizing perforation geometry can be an effective strategy to enhance stimulation uniformity, particularly in low-rate injection scenarios where total flow area strongly influences cluster communication and inflow partitioning.

Parameters	Value
In-situ stress (MPa)	43.99, 51.09, 65.71
Young's modulus (GPa)	54.8

Poisson's ratio	0.26
Biot's coefficient	0.85
Reservoir porosity	0.01
Reservoir permeability (μD)	5
Reservoir pore pressure (MPa)	2.355
Fluid viscosity (cp)	1
Fluid compressibility (10^{-10}Pa^{-1})	5
Proppant density (kg/m^3)	2650
Proppant diameter (m)	0.0002
Cluster spacing (m)	7.5
Clusters per stage	8
Perforations per cluster	18
Perforation diameter (inch)	0.33
Perforation plugging concentration	0.115
Rock tensional strength (MPa)	5

Table 9.1: Reservoir-fracture-well modeling inputs of the Base Case.

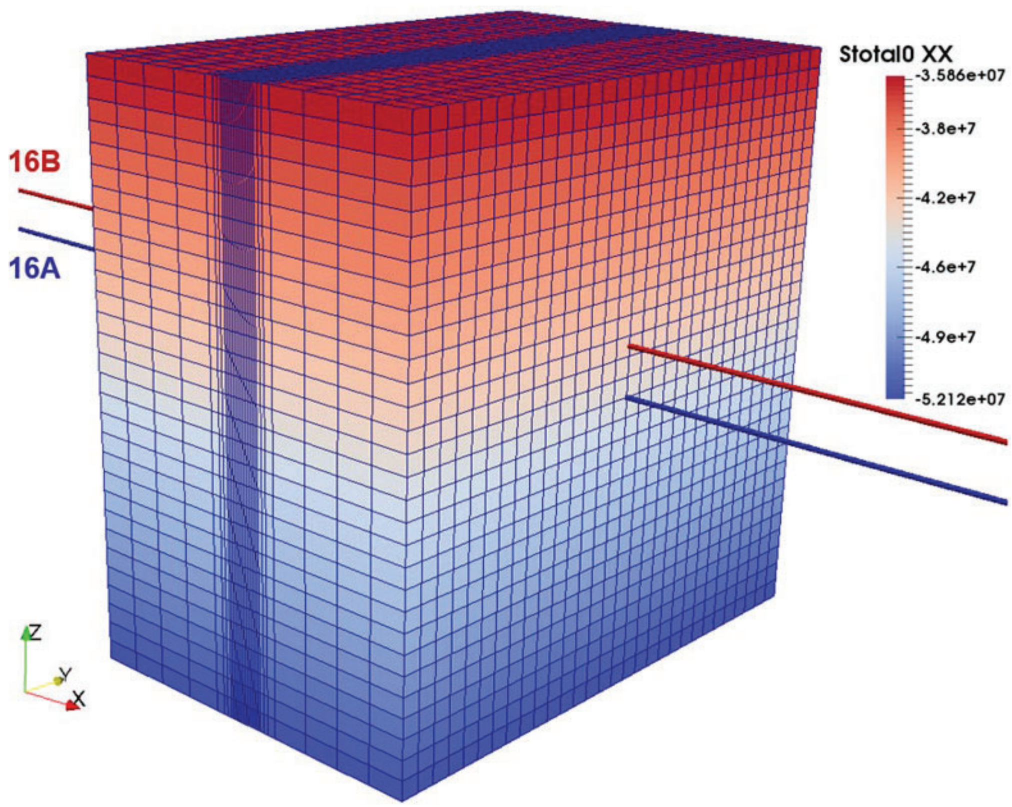

Figure 9.1: Computational mesh for the Base Case. In-situ stress gradient is applied to the simulated domain.

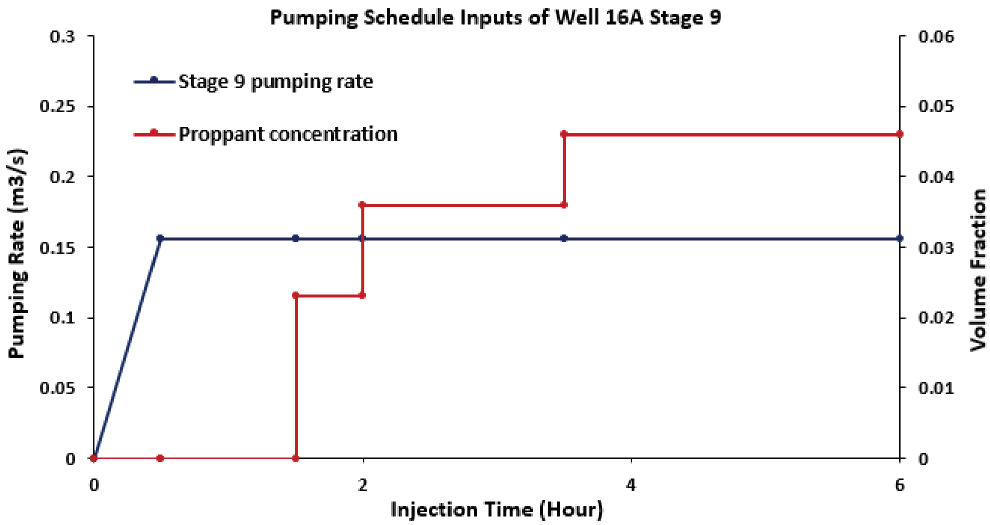

Figure 9.2: Pumping schedule modeling inputs for FORGE April 2024 well 16A Stage 9 stimulation.

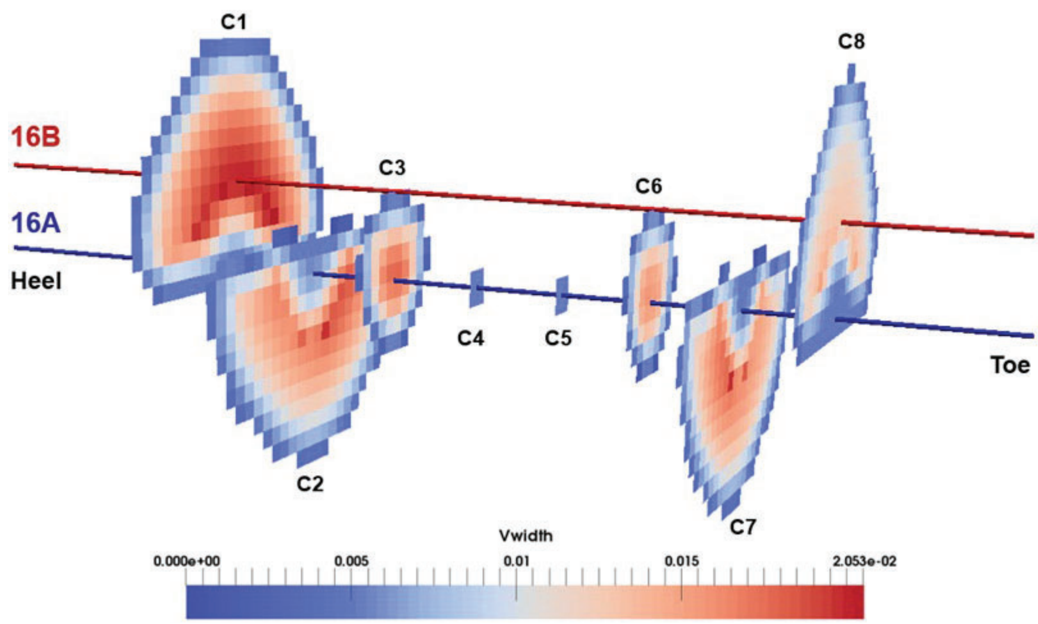

Figure 9.3: Simulated fracture geometry at the end of the 6-hour fracturing treatment. Distance in the direction of the wellbore is enlarged by 10 times for clearer visualization.

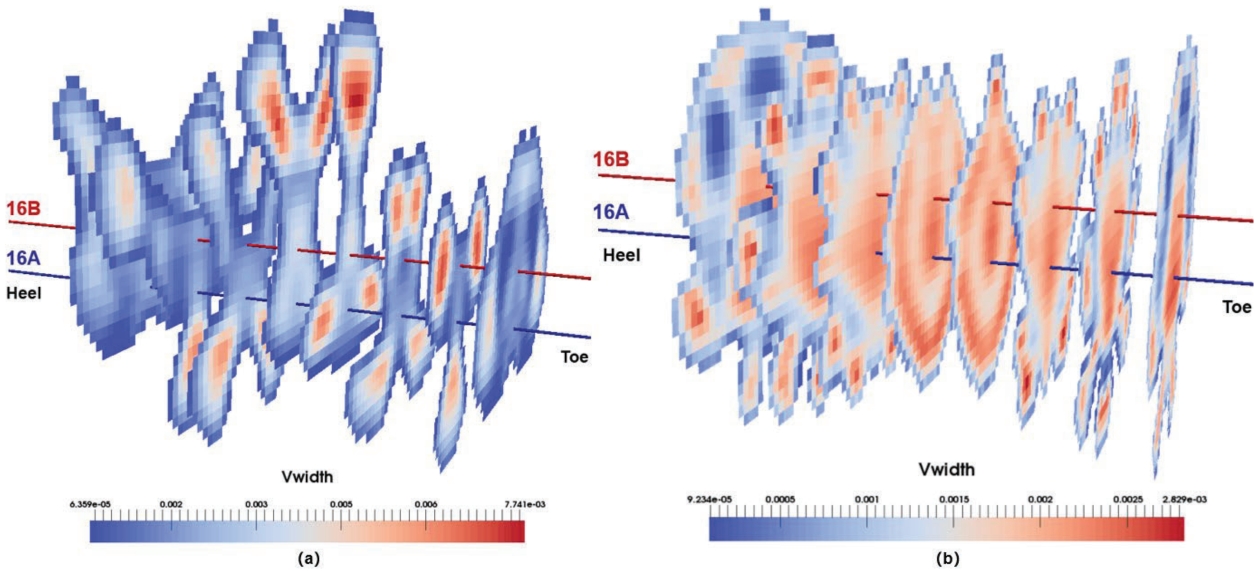

Figure 9.4: Simulated fracture geometry of the fluid property sensitivity cases. Distance in the direction of the wellbore is enlarged by 10 times for observation convenience. (a) fracturing fluid viscosity = 20cp. (b) fracturing fluid viscosity = 100cp.

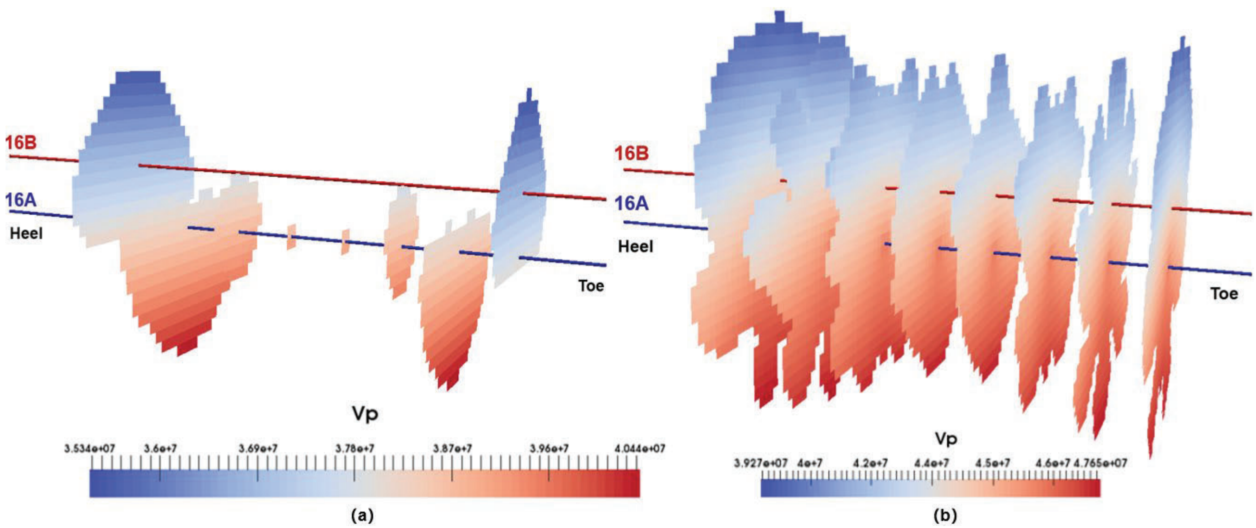

Figure 9.5: Simulated fracture geometry and fracture fluid pressure. Distance in the direction of the wellbore is enlarged by 10 times for observation convenience. (a) fracturing fluid viscosity = 1cp. (b) fracturing fluid viscosity = 100cp.

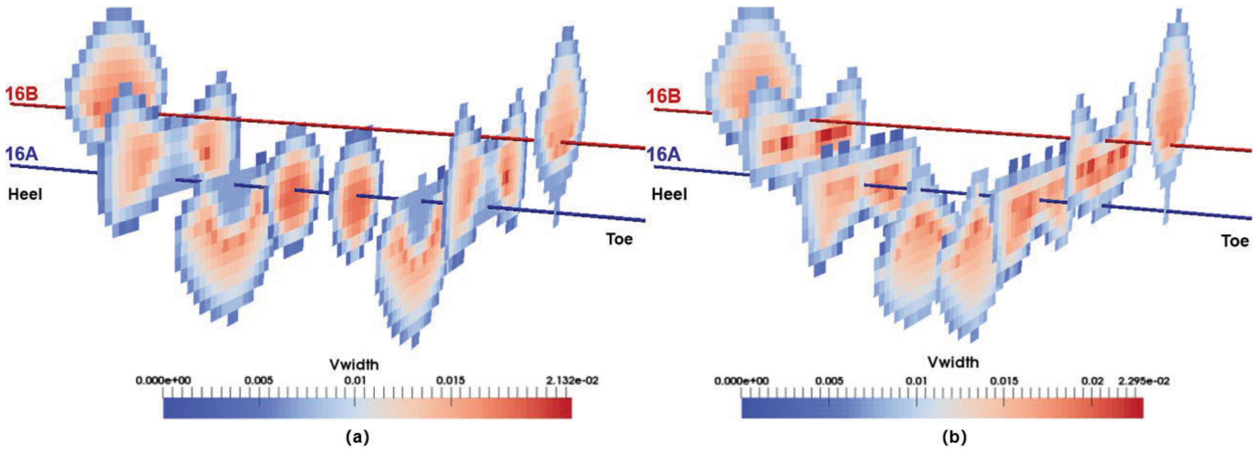

Figure 9.6: Simulated fracture geometry of the completion design sensitivity cases. Distance in the direction of the wellbore is enlarged by 10 times for observation convenience. (a) perforation per cluster = 6. (b) perforation per cluster = 2.

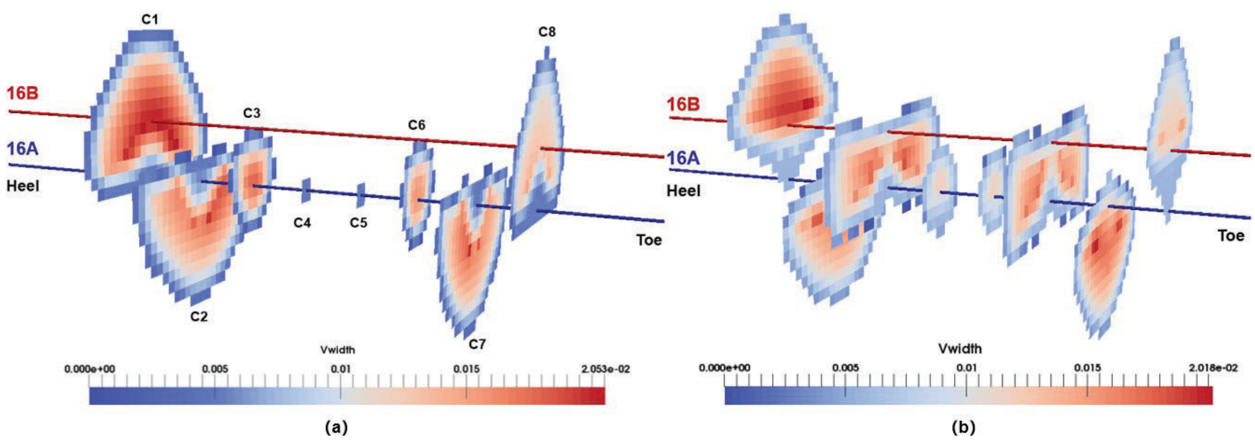

Figure 9.7: Simulated fracture geometry of the pumping schedule sensitivity cases. Distance in the direction of the wellbore is enlarged by 10 times for observation convenience. (a) gradually increase to maximum pumping rate in 30 minutes. (b) instantly pump to the maximum rate at the start of injection.

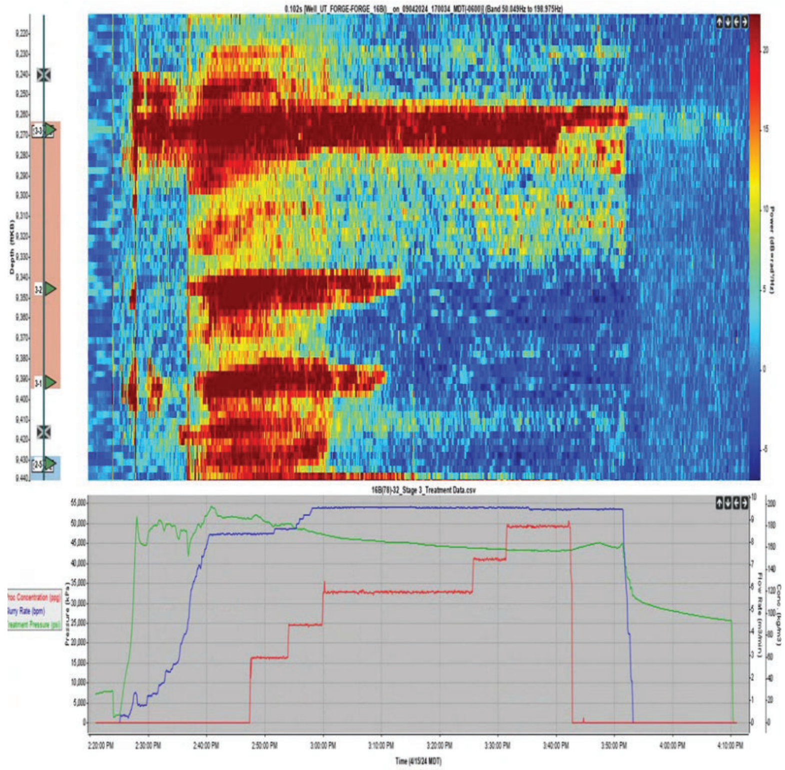

Figure 9.8: HF-DAS data during the April 2024 stimulation well 16B stage 3 at the Utah FORGE site. The fiber optic waterfall plot suggested a clear heel dominated fracture pattern where cluster screen-out happened at the locations of toe-side and middle cluster.

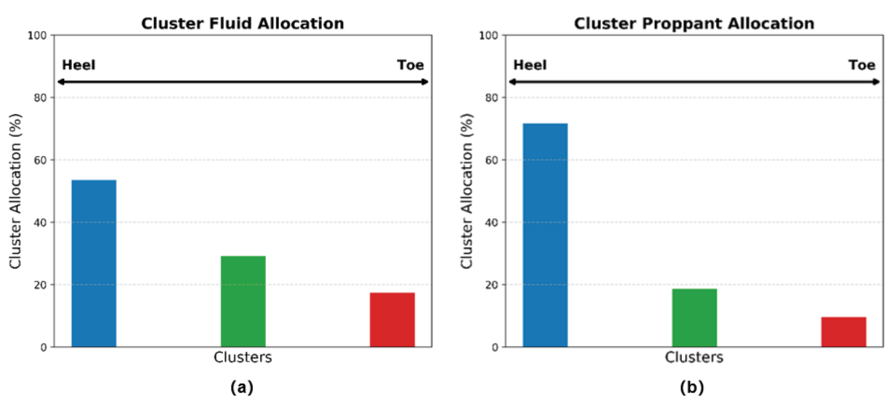

Figure 9.9: (a) Base Case final fluid allocation per cluster. (b) Base Case final proppant allocation per cluster.

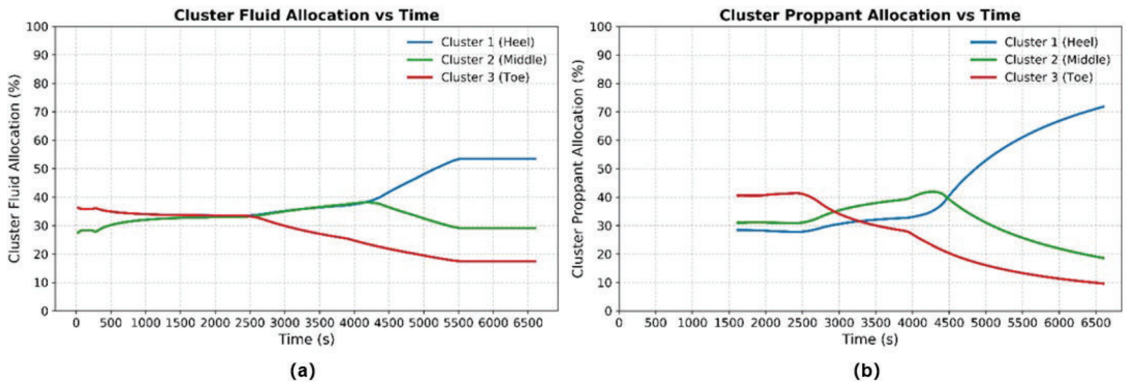

Figure 9.10: (a) Base Case fluid allocation vs time per cluster. (b) Base Case proppant allocation vs time per cluster.

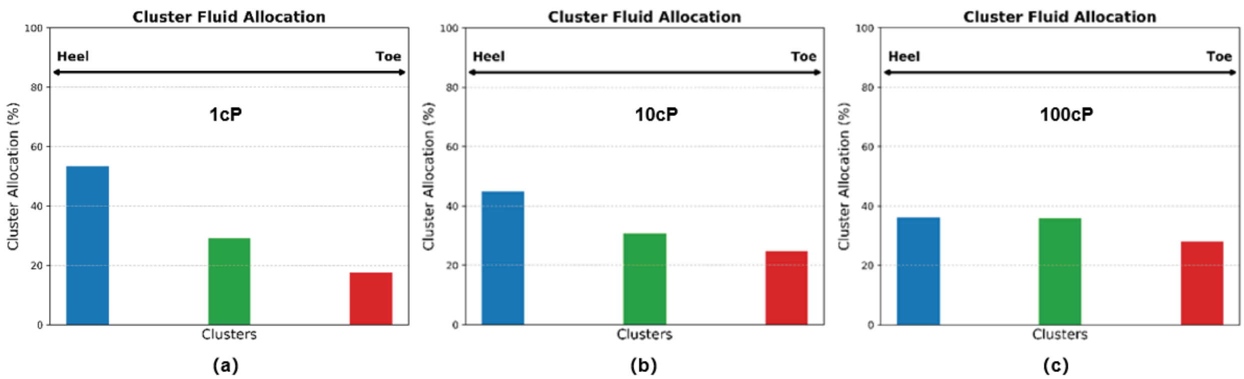

Figure 9.11: Final fluid allocation per cluster. (a) Fluid viscosity = 1cP. (b) Fluid viscosity = 10cP. (c) Fluid viscosity = 100cP.

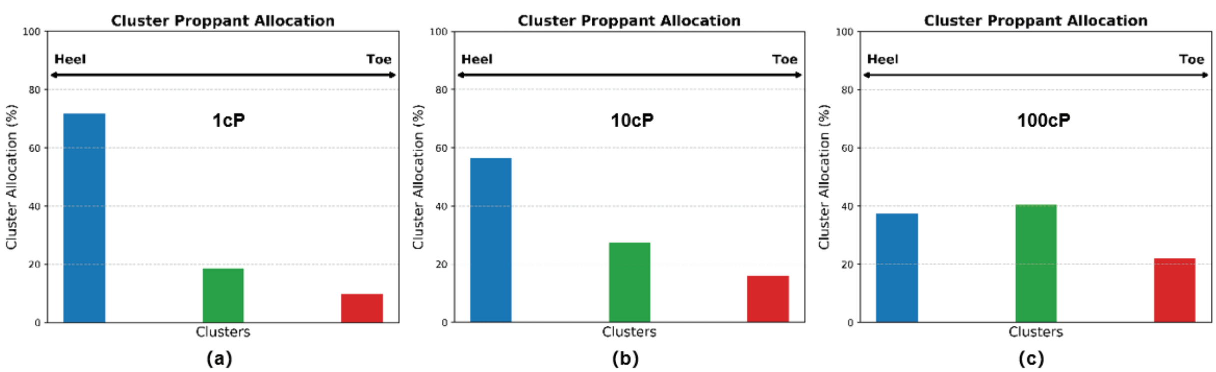

Figure 9.12: Final proppant allocation per cluster. (a) Fluid viscosity = 1cP. (b) Fluid viscosity = 10cP. (c) Fluid viscosity = 100cP.

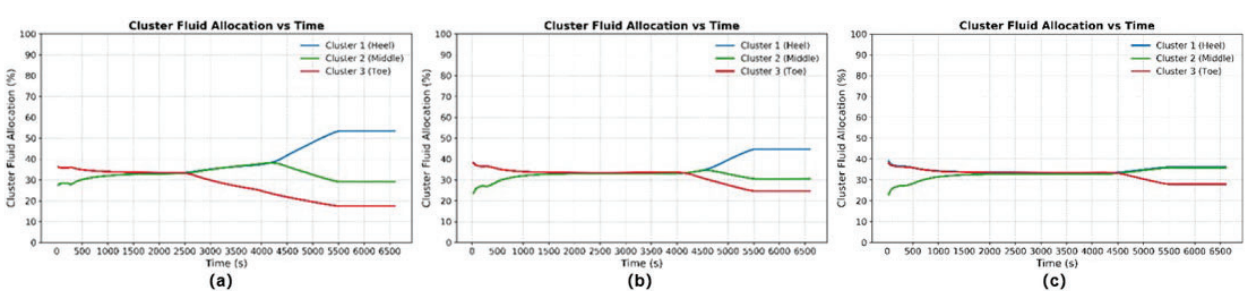

Figure 9.13: Fluid allocation vs time per cluster. (a) Fluid viscosity = 1cP. (b) Fluid viscosity = 10cP. (c) Fluid viscosity = 100cP.

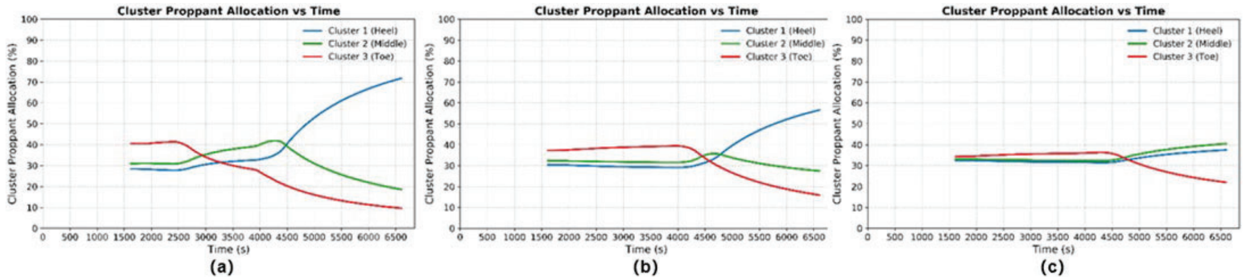

Figure 9.14: Proppant allocation vs time per cluster. (a) Fluid viscosity = 1cP. (b) Fluid viscosity = 10cP. (c) Fluid viscosity = 100cP.

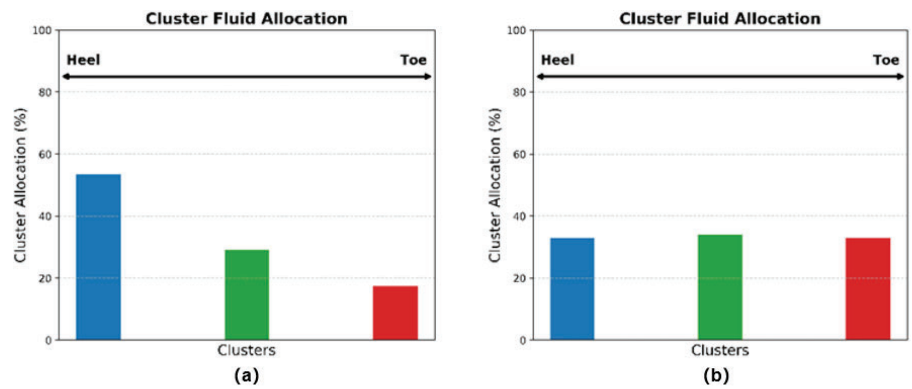

Figure 9.15: Final fluid allocation per cluster. (a) Base Case. (b) Lightweight proppant case.

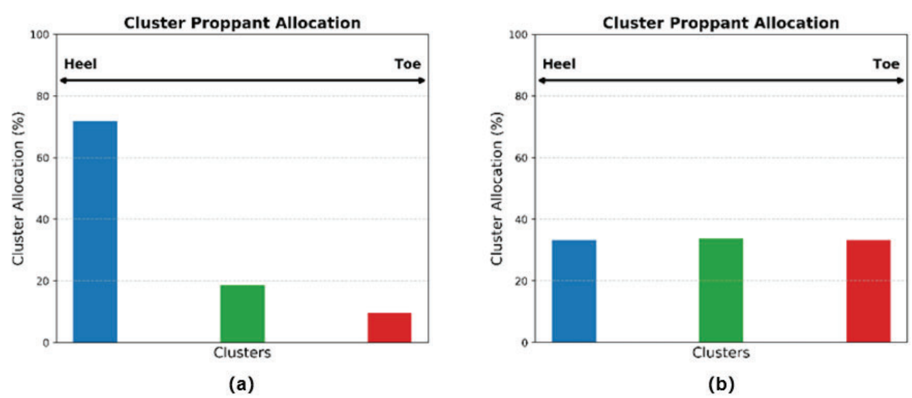

Figure 9.16: Final proppant allocation per cluster. (a) Base Case. (b) Lightweight proppant case.

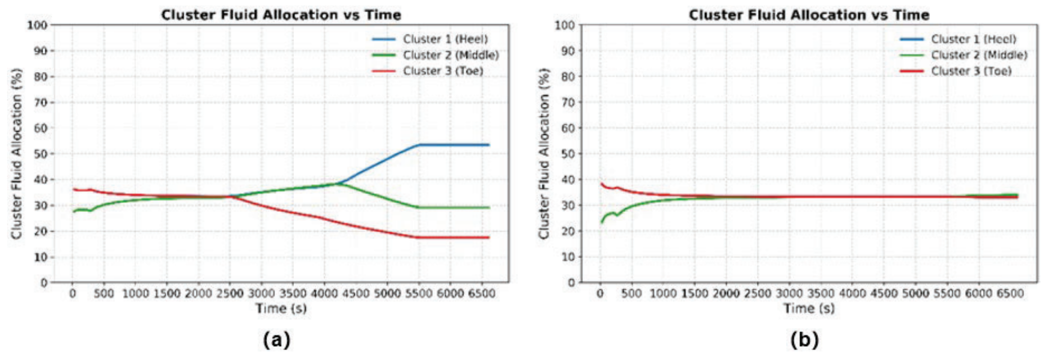

Figure 9.17: Fluid allocation vs time per cluster. (a) Base Case. (b) Lightweight proppant case.

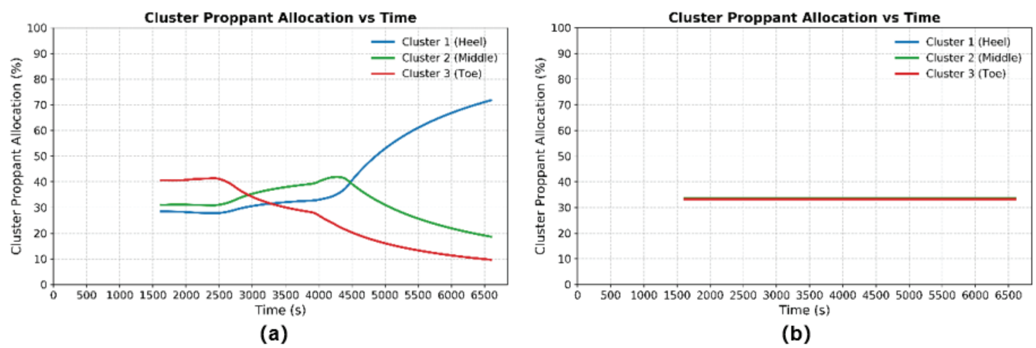

Figure 9.18: Proppant allocation vs time per cluster. (a) Base Case. (b) Lightweight proppant case.

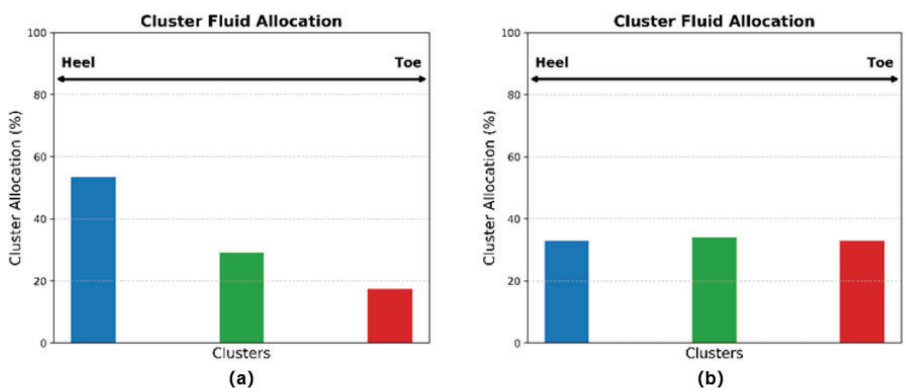

Figure 9.19: Final fluid allocation per cluster. (a) 10 perforations per cluster. (b) Tapered perforation design.

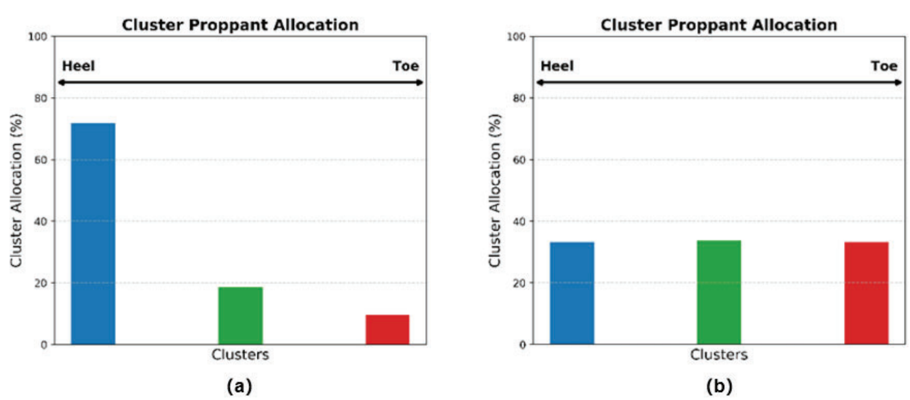

Figure 9.20: Final proppant allocation per cluster. (a) 10 perforations per cluster. (b) Tapered perforation design.

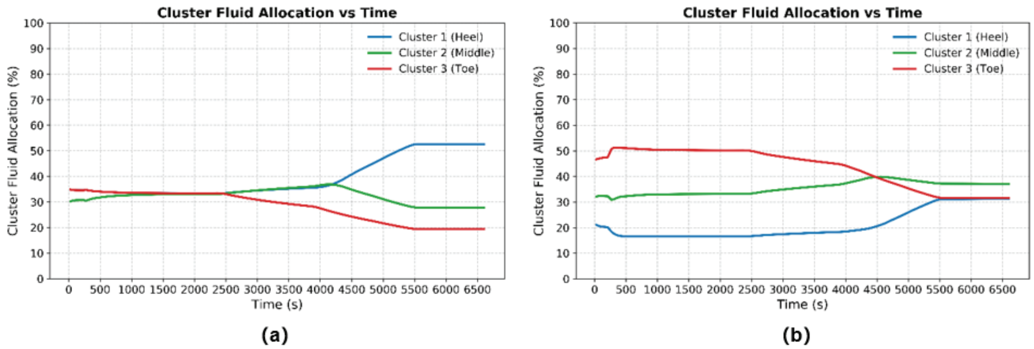

Figure 9.21: Fluid allocation vs time per cluster. (a) 10 perforations per cluster. (b) Tapered perforation design.

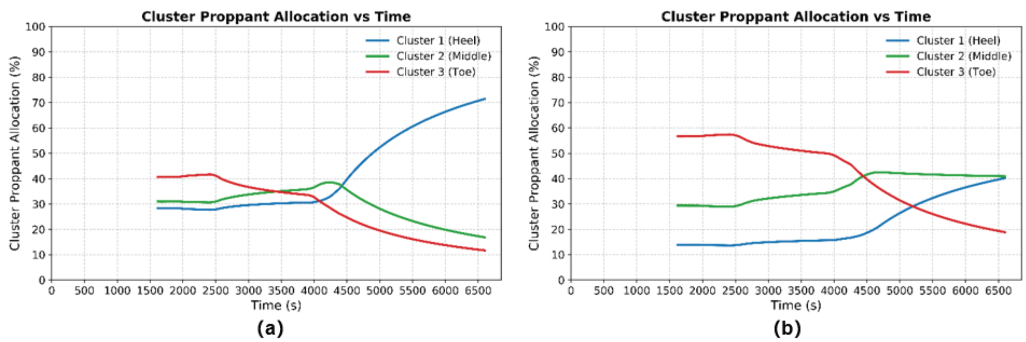

Figure 9.22: Proppant allocation vs time per cluster. (a) 10 perforations per cluster. (b) Tapered perforation design.

List of Papers

1. "Integration of Fiber Optic Data with FMI And Chemical Tracer Data To Evaluate Inter-well Fracture Connectivity and Fluid Circulation In Geothermal Well Pairs", Y. Ou, Chris Fredd and Mukul Sharma, SPE Hydraulic Fracturing Conference, Feb., 2026.
2. "Strategies for Improving Inter-well Connectivity and Proppant Placement In EGS Well Pairs: A Field Study Integrating Models And Well Fiber Optic Data", Y. Li, Y. Ou, M. Mura, Mukul Sharma, SPE Hydraulic Fracturing Conference, Feb., 2026.
3. "Pressure Drawdown Testing in Fractured Production Wells: Impact Of Geomechanics And Fracture Closure", Y. Li, Y. Ou, Mukul Sharma, SPE Hydraulic Fracturing Conference, Feb., 2026.
4. "Acoustic Emission Signatures During Frictional Sliding Of Rocks: Insights Into Induced Seismicity Events", A. Sathyanath, Mukul Sharma, SPE Hydraulic Fracturing Conference, Feb., 2026.
5. "Inversion Of Natural Fracture Properties Using Microseismic Data And Hydraulic Fracture Simulation", Q. Liu and Mukul Sharma, SPE Hydraulic Fracturing Conference, Feb., 2026.
6. "Monitoring fluid circulation in an enhanced geothermal system with permanent fibers", ARMA Workshop on Distributed Fiber Optic Sensing for Geomechanical Applications, Paper presented at the 58th US Rock Mechanics/Geomechanics Symposium held in Golden, Colorado, USA, 23-26, June 2024, Yuhao Ou and Mukul M. Sharma.
7. "Factors Controlling the Flow and Connectivity in Fracture Networks in Naturally Fractured Geothermal Formations," SPE Drilling and Completions, Vol. 38, issue 01, pp 131-145, SPE-212292-PA, March 2023, M. Cao and M.M. Sharma. https://doi.org/10.2118/212292-PA.
8. "A computationally efficient model for fracture propagation and fluid flow in naturally fractured reservoirs," Journal of Petroleum Science and Engineering, Vol. 220, Part B, pp 111249, January 2023, M. Cao and M.M. Sharma. https://doi.org/10.1016/j.petrol.2022.111249
9. "The impact of changes in natural fracture fluid pressure on the creation of fracture networks," Journal of Petroleum Science and Engineering, Vol. 216, pp. 110783, September 2022, M. Cao and M.M. Sharma. https://doi.org/10.1016/j.petrol.2022.110783
10. "Creation of a Data-Calibrated Discrete Fracture Network of the Utah FORGE Site," ARMA 23–0822, Paper was presented at the 57th US Rock Mechanics/Geomechanics Symposium held in Atlanta, Georgia, USA, 25-28 June 2023, M. Cao and M.M. Sharma.
11. "Integrating a Boundary Element Method Based Hydraulic Fracturing Simulator with a Compositional Reservoir Simulator for Well Lifecycle Simulations," ARMA 23–0382, Paper was presented at the 57th US Rock Mechanics/Geomechanics Symposium held in Atlanta, Georgia, USA, 25-28 June 2023, M. Cao, S. Zheng, and M.M. Sharma.
12. "Geomechanical Modeling of Fracture Growth in Naturally Fractured Rocks: A Case Study of the Utah FORGE Geothermal Site," Paper presented at the Unconventional Resources

Technology Conference held in Denver, Colorado, USA, 13-15 June 2023, M. Cao and M.M. Sharma.

13. "The Effect of Variations of Fluid Pressure in Natural Fractures on the Geometry of Fracture Networks and Well Productivity," Paper presented at the Unconventional Resources Technology Conference held in Denver, Colorado, USA, 13-15 June 2023, M. Cao and M.M. Sharma.
14. "Factors Controlling the Flow and Connectivity in Fracture Networks in Naturally Fractured Geothermal Formations," SPE Drilling and Completions, Vol. 38, issue 01, pp 131-145, SPE-212292-PA, March 2023, M. Cao and M.M. Sharma. https://doi.org/10.2118/212292-PA
15. "A computationally efficient model for fracture propagation and fluid flow in naturally fractured reservoirs," Journal of Petroleum Science and Engineering, Vol. 220, Part B, pp 111249, January 2023, M. Cao and M.M. Sharma. https://doi.org/10.1016/j.petrol.2022.111249
16. "An Efficient Model of Simulating Fracture Propagation and Energy Recovery from Naturally Fractured Reservoirs: Effect of Fracture Geometry, Topology and Connectivity," SPE-212315-MS, Paper presented at the SPE Hydraulic Fracturing Technology Conference and Exhibition, January 31–February 2, 2023, M. Cao and M.M. Sharma, doi: https://doi.org/10.2118/212315-MS
17. "The impact of changes in natural fracture fluid pressure on the creation of fracture networks," Journal of Petroleum Science and Engineering, Vol. 216, pp. 110783, September 2022, M. Cao and M.M. Sharma. https://doi.org/10.1016/j.petrol.2022.110783